KINETICALLY CONTROLLED Si-EPITAXY ON Si(100) AND Ge(100)

Marcus Eßer

The work described in this thesis was performed in the MESA+ Research Institute (Solid State Physics Group, Faculty of Applied Physics) at the University of Twente, P.O. Box 217, NL-7500 AE Enschede, The Netherlands.

Eßer, M.
Kinetically controlled Si-epitaxy on Si(100) and Ge(100)
Proefschrift Universiteit Twente, Enschede.
ISBN 90-365-1641-2

published by the Solid State Physics Group, University of Twente
printed in The Netherlands by Wormgoor B.V., Almelo.

© M. Eßer, 2001. No part of this publication may be stored in a retrieval system, transmitted, or reproduced in any way, including but not limited to photocopy, photograph, magnetic or other record, without the prior agreement and written permission of the publisher.

meinen Eltern
für ihre großartige Unterstützung

KINETICALLY CONTROLLED Si-EPITAXY ON Si(100) AND Ge(100)

PROEFSCHRIFT

ter verkrijging van
de graad van doctor aan de Universiteit Twente,
op gezag van de rector magnificus,
prof. dr. F.A. van Vught,
volgens besluit van het College voor Promoties
in het openbaar te verdedigen
op donderdag 13 september 2001 te 13.15 uur.

door

Marcus Eßer
geboren op 8 juli 1971
te Siegburg (Duitsland).

Dit proefschrift is goedgekeurd door de promotor:
prof. dr. ir. B. Poelsema
en de assistent-promotor:
dr. ir. H. Wormeester

Contents

1 Introduction **1**
1.1 Growth on semiconductor surfaces . . . 2
1.1.1 Si(100) and Ge(100) surfaces . . . 2
1.1.2 Kinetic growth and nucleation . . . 5
1.1.3 Advancing growth . . . 7
1.1.4 Heteroepitaxy . . . 8
1.2 Experimental techniques . . . 9
1.2.1 SPA-LEED . . . 9
1.2.2 STM . . . 11
1.2.3 Ellipsometry . . . 12
1.3 Experimental setup . . . 14
1.3.1 UHV system . . . 14
1.3.2 Samples . . . 17
1.3.3 Sample holder . . . 17
1.3.4 Sample cooling . . . 19
1.3.5 Evaporator . . . 21
1.4 Sample preparation . . . 21
1.4.1 Automatic sample preparation . . . 21
1.4.2 Silicon . . . 22
1.4.3 Germanium . . . 23

2 Improvements in SPA-LEED data acquisition **25**
2.1 Introduction . . . 25
2.2 Spotfinder class . . . 27
2.2.1 Center-of-intensity algorithm . . . 28
2.2.2 Overshooting . . . 28
2.2.3 Reliability . . . 29
2.2.4 Multiple instances . . . 30
2.2.5 I/E curves . . . 31
2.2.6 SPA-LEED measurements vs. sample temperature . . . 33
2.3 Extended one-dimensional intensity measurements . . . 34
2.3.1 Real-time spot profile series . . . 34
2.3.2 Spot profile series vs. electron energy . . . 36

2.4 Automatic experiments . . . 38
2.5 Distortion correction . . . 38
2.5.1 Calculating the undistorted spot positions . . . 38
2.5.2 Energy dependence of the fit parameters . . . 41
2.6 Conclusion . . . 44

3 Homoepitaxy on Si(111) 47
3.1 Introduction . . . 47
3.2 Experimental . . . 48
3.3 Multiple diffraction spot tracking . . . 48
3.4 Summary . . . 56

4 Homoepitaxy of Si(100) 59
4.1 The network of anti-phase boundaries (APB) . . . 59
4.2 Conventional growth . . . 62
4.3 Growth manipulation . . . 64
4.3.1 Smoothing a Si monolayer . . . 64
4.3.2 Flatten thicker Si films . . . 68
4.3.3 Failure of the concept of two mobilities . . . 70
4.4 Conclusions . . . 71

5 Si heteroepitaxy on Ge(100) 73
5.1 Conventional growth at 525 K . . . 74
5.2 Conventional growth at 343 K . . . 81
5.3 Manipulated growth at 343 K . . . 85

A WinSPA32 95
A.1 technical details . . . 95
A.1.1 I/O hardware . . . 95
A.1.2 System requirements . . . 96
A.2 source code hardware driver DLL # 1 . . . 96
A.3 source hardware driver DLL # 2 . . . 98

Bibliography 99

Summary 109

Samenvatting 113

Acknowledgements 117

Chapter 1

Introduction

Confinement of a solid state material in one or more dimensions to the nanometer scale can give rise to different and even completely new physical properties. Such a change in physical properties has been demonstrated for many materials. In particular, germanium and silicon have drawn great attention. The major drawback for the technological application of these materials is their indirect band gap, i.e. they are not as suitable for electro-optical purposes as the well-known III-V materials. The wide application of the latter is, however, hampered by their incompatibility to the highly advanced silicon technology. Confined silicon and germanium, with sizes in at least one dimension of only a few nanometers have shown a direct band gap. Application of such nanostructures depends on how well they can be grown, especially in stacked structures. This involves the growth of material A (Si) on B (Ge) and B (Ge) on A (Si). Under (or close to) equilibrium conditions, the spreading of one material on the other depends on the value of the surface and interface free energies and the difference in lattice constant of the two materials. The larger the difference of surface and interface free energies between the two, the better is the spreading of at least one material upon deposition on the other [Bau58]. However, this also means that the reverse situation, deposition of B on A will involve strong island formation, a situation not desired for the growth of a stacked structure. To overcome these problems, growth may be performed at low temperature, i.e., in the kinetic region at a sufficient supersaturation of the deposited material. We note that interdiffusion may further complicate the qualitative picture outlined above.

In the kinetic growth regime the question of the roughening of the growth front has to be addressed. A smooth growth front is only possible in the presence of sufficient interlayer transport. There are many examples of growth studies in which this interlayer mass transport is too small or even absent, resulting in a progressive roughening of the growth front. So called kinetic growth manipulation (KGM) techniques have been developed to

overcome the roughening of the growth front in the case of unreconstructed metal surfaces, e.g. [RST+93, RPC95, RLW+95]. A sufficient condition for the success of such an approach is that nucleation in the next layer does not or hardly occur before the completion of the previous one. Within the deposition of the monolayer (ML) the interlayer mass transport has to be manipulated in an appropriate way to achieve this. A recipe to reach this goal for reconstructing (100) semiconductor surfaces has been developed by Wulfhekel [Wul97, WZH+98]. To gain further insight in the processes governing his approach, the homo-epitaxial growth on a Si(001) surface will be studied: In chapter 4 an analysis of the limited interlayer mass transport at reduced temperatures is presented in connection to the specific reconstruction of the Si(001) surface. The identification of the problem makes it easy to find a solution in this specific case. In order to make this analysis, an in-situ probe of the morphology is required next to scanning probe microscopy for a detailed analysis of the morphology after a specific deposition. For this in-situ Spot Profile Analysis Low Energy Electron Diffraction (SPA-LEED) is used. The extended use of this technique has required the development of improved software to control the instrument. The capabilities of the software are presented in chapter 2. Some possibilities and limitations of the SPA-LEED technique for in-situ analysis are discussed for homoepitaxy of Si(111) in chapter 3.

The interface free energy of Si(001) is higher than that of Ge(001). This implies that reduced temperatures have to be used to grow flat layers of Si on Ge(001). The strong intermixing of these two materials further reinforces the temperature constraint. The critical thickness of a layer above which the lattice misfit leads to the break up of the layer and the formation of islands to reduce the stress build up in the layer is known to increase with lower growth temperatures. In chapter 5 the growth of well-defined ultra-thin layers of silicon on germanium is studied and it will be shown that even at very moderate temperatures intermixing strongly affects the growth. The KGM method developed for silicon homoepitaxy applied in this heteroepitaxial case enables the growth of an ultra thin epitaxial silicon layer on germanium.

In the following sections, some important physical and experimental details for the measurements described in this thesis will be presented.

1.1 Growth on semiconductor surfaces

1.1.1 Si(100) and Ge(100) surfaces

The surface atoms of both the Si(100) and Ge(100) form dimers to reduce the number of dangling bonds. In this way, the surface free energy is lowered substantially. The ar-

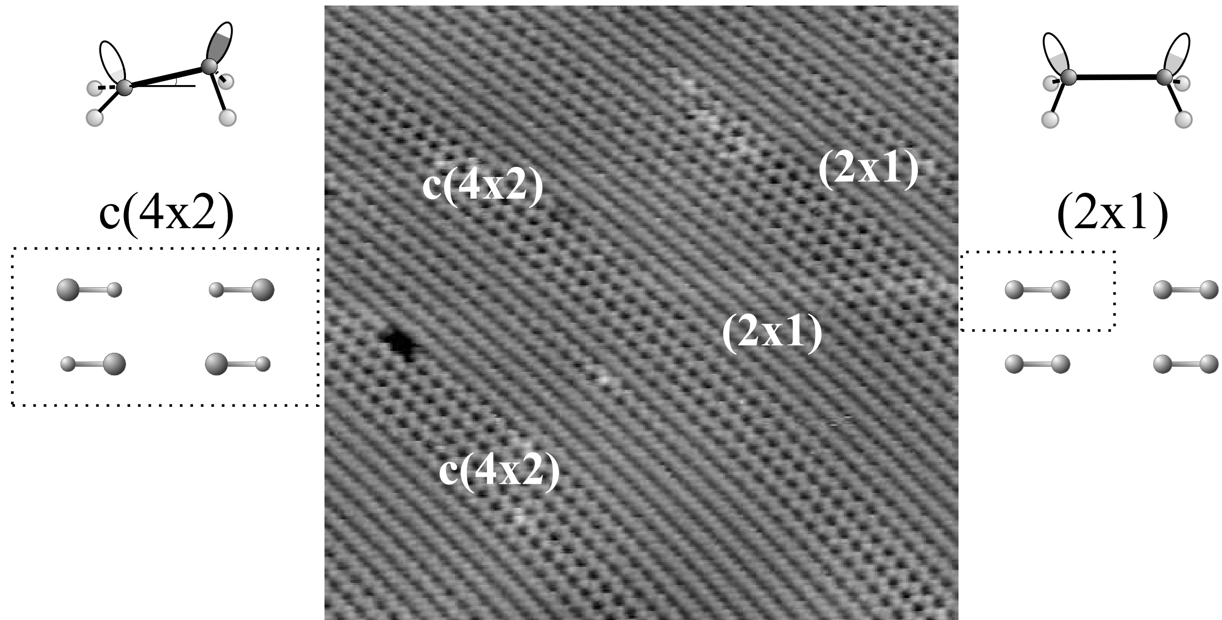

Figure 1.1: STM scan of a clean Ge(100) surface at RT. Domains of c(4x2) and (2x1) coexist. Form the point of view of STM, when the buckled dimers of the c(4x2) reconstruction (see left panel) are continuously flipping from one side to the other, they appear as non-buckled buckled (2x1) dimers (see right panel). The dotted rectangles mark the repeating cells of the two types of reconstruction.

rangement of buckled dimers in rows leads to the c(4x2) reconstruction. When the buckled dimers are continuously flipping from one side to another, the c(4x2) reconstruction turns into the (1x2) reconstruction. Figs. 1.2 and 1.1 show exemplary a diffraction pattern and an STM scan of a clean Ge(100) surface with c(4x2) and (1x2) reconstructions coexisting.

The reconstruction of the surfaces just mentioned has crucial influence on the roughness of films that are grown on it: Neighbouring islands that grow epitaxially on a terrace of a reconstructed surface have a chance of 50% to be in the wrong registry with respect to each other. When two islands that are out of registry grow and get closer, they cannot grow together without major atomic rearrangements. Instead, an *anti-phase-boundary* (APB) is created. There are two types of APBs (see fig. 1.3), APB_A and APB_B (according to the type of step that is incorporated by the APB). In this way a network of APBs builds up that hampers the diffusion of dimers on top. The APB_Bs act as a preferential nucleation sites. The result is an increased island density, which enlarges the density of the APB network in higher layers. As the A-type APBs cannot be filled up, the nucleation in the top layers will start with the underlying layers being filled less and less as the density of the

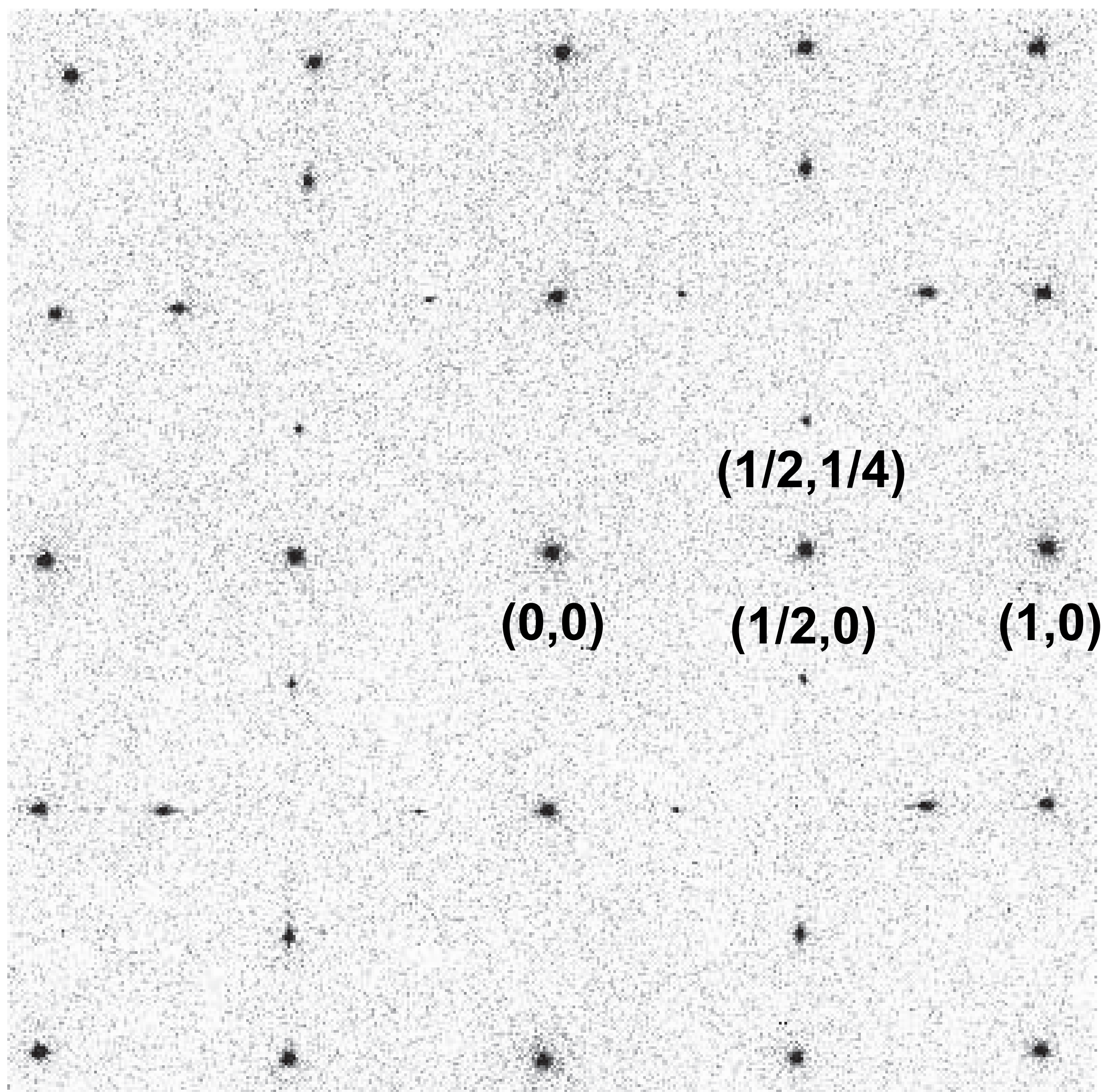

Figure 1.2: Diffraction pattern of a clean Ge(100) surface at 100 K. (width $\approx$ 2.2 BZ, E = 124.9 eV, resolution 400x400 pixels, integration time 15 ms/pixel), colour coding (logarithmic): white = 100 cps - black 100 kcps). Apart from the central and first order spots, the half-order and the spots of the c(4x2)-reconstruction are present.

APB-network rises, i.e. the grown film roughens progressively. At this point it becomes clear, that in contrast to unreconstructed surfaces roughening during epitaxial growth is intensified by the APB network, a consequence of surface reconstruction.

1.1.2 Kinetic growth and nucleation

During most growth experiments described in this thesis, the growth parameters (rate of the molecular beam epitaxy(MBE)-source, temperature of the semiconductor samples) were set to values that kept the observed system far away from thermodynamic equilibrium. Therefore, many of the observed growth phenomena are determined by kinetics rather than thermodynamics. At moderate sample temperatures growth is expected to proceed via nucleation and growth of adatom islands. The average island density N is then [Ven73, VSH84, BC94, BE92, BE93, AF94, AF95]

$$N \approx \eta(\theta) \cdot \left(\frac{F}{\nu_0}\right)^p \cdot \exp\left(\frac{p \cdot (E_d + (E_i/i))}{kT}\right) \tag{1.1}$$

where $\eta(\theta)$ is a parameter that depends weakly on the film coverage θ. F is the deposition flux. E_d is the activation energy for adatom diffusion on a terrace, ν_0 is the associated attempt frequency. $p = i/(i+1)$, where i is the number of atoms in the critical nucleus. E_i is the binding energy of the critical nucleus.

At growth conditions, which lead to very low islands densities N (i.e. high sample temperatures and/or low deposition rates) the characteristic adatom diffusion length on terraces can be larger than the width of the terraces. In this situation, which is close to the thermodynamic equilibrium, the film grows by *step flow*. In contrast, the adatom diffusion is suppressed at very low temperatures. Then the island density is dependent neither on sample temperature nor on deposition flux. For the semiconductor substrates discussed here, this leads to amorphous growth.

As the islands grow in size in the course of growth experiments on reconstructed Si(100) and Ge(100) surfaces, their shape is influenced strongly by the surface reconstruction: While the diffusion of ad-dimers along the substrate dimer rows is taking place at relatively low temperatures (about RT in the case of diffusion of Si-dimers on top of Si(100) substrate dimer rows), the ad-dimer diffusion across the substrate dimer rows becomes active only at higher temperatures (> 725 K for Si on Si(100)). This limitation in dimer diffusion leads to the growth of islands that are asymmetrically elongated in the direction of the dimer rows (see the detailed study of Zoethout [Zoe01])[1].

[1] This effect can even be intensified by anisotropical attachment of dimers to the islands [Zan00].

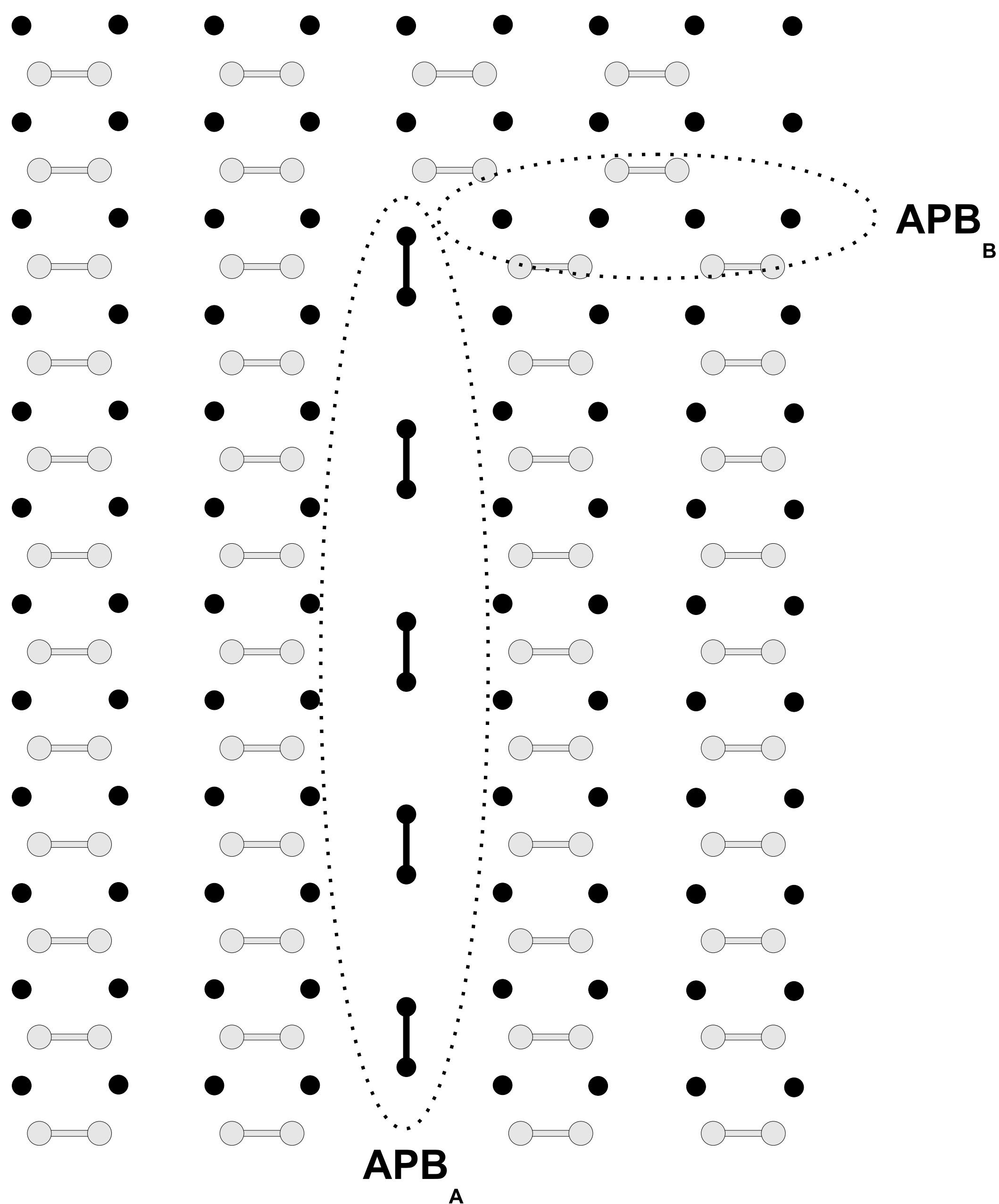

Figure 1.3: The two types of anti-phase boundaries (APB$_A$ and ABP$_B$, according to the type of step which is incorporated by the APB) on a (2x1) reconstructed (100) surface. The grey dumbbells represent the dimers in the topmost layer. The black points and dumbbells show the atoms and dimers one layer underneath.

1.1.3 Advancing growth

After nucleation, kinetic growth continues in a combination of the following two idealized modes: The first mode is the *layer-by-layer growth* or *two-dimensional growth*. In this mode nucleation on top of the islands does not take place before the layer with the islands is filled completely, resulting in smooth layers. The second mode is the *three-dimensional growth*; here interlayer mass transport is suppressed completely resulting in even earlier nucleation in higher layers. The result is a continuously roughening growth front.

Kinetic growth manipulation

It is the aim of *kinetic growth manipulation* (KGM) methods to force systems to grow via the layer-by-layer mode as much as possible. This is done by changing one or more of the parameters that control the growth process, for example deposition rate or sample temperature (supersaturation) with the rhythm imposed by monolayer equivalent deposits. Such KGM methods always base on a thorough analysis of what is actually causing the nucleation on top of islands before the underlying layer is fully completed. Three-dimensional growth is caused by a weak *interlayer mass transport* preventing the adatoms from reaching the lower layer before they nucleate. The weak interlayer mass transport is caused by an additional energy barrier at the island edge for downward diffusion, the so-called Ehrlich-Schwoebel barrier [EH66, SS66, KPVC90].

For such systems KGM methods that enhance the interlayer mass transport can be successful. A well-known exponent for these methods is the so called *concept of two mobilities* [RST+93, RPC95, RLW+95]. It uses growth parameters for a high island density N in the initial part of every layer's growth (lower growth temperature and/or higher deposition speed) and parameters for a lower N for the rest of the layer (higher growth temperature and/or lower deposition speed). This method can lead to smoother films: Because a lower island density N in the second period of the layer's growth also means an increased diffusion length, the adatoms that land on top of islands have an increased attempt frequency to overcome the additional energy barrier at the island edge and diffuse downwards. With more adatoms diffusing downwards, the interlayer mass transport is enhanced and the chance for nucleation on top of islands is lowered.

For systems that incorporate more complicated surfaces, KGM methods that aim at the reduction of restricted interlayer diffusion imposed by an Ehrlich-Schwoebel barrier may not work as there may be other reasons enhancing nucleation on top of islands. The reconstruction of the Si(100) surface for example turns out to give rise indirectly for early island nucleation on top of islands (see 1.1.1): the APBs that are concomitants of this reconstruction can act as preferential nucleation sites (see chapter 4). Wulfhekel et al.

have presented a KGM method for the growth of Si on Ge(100) that apparently overcomes also the obstacle of preferential nucleation at APBs [Wul97, WZH+98] and leads to films of unprecedented smoothness.

Surfactants

A completely different approach towards smooth film growth is the use of *surfactants*. In the case of Si on Ge(100), Copel et al. were able to suppress island formation using As as surfactant [CRKT89]. Using high-resolution photoemission, Cao et al. provided a microscopic description of the epitaxial Si on Ge(100) growth process using Sb as a surfactant [CYTP92]. They find that Sb fully saturates the surface dangling bonds. This would be the prerequisite for a growth mode, which is not hampered by reconstruction-induced problems like for example APBs. Gonzalez-Mendez et al. point out that possibility of Si diffusion into the Ge substrate is greatly reduced by the use of As as surfactant [GMT99].

Nevertheless, the use of a surfactant may contaminate the growth system that it is to assist. Of course, the consequences of the contamination on possible properties of the grown system are unknown. That's why, the perspective of reaching smooth films contamination free is a strong motivation for studying the use of KGM methods.

1.1.4 Heteroepitaxy

In case of heteroepitaxial growth systems the situation gets much more complicated compared to the homoepitaxy: the interlayer mass-transport can differ considerably with the layer height. This may for instance happen as a function of misfit induced changes of lateral diffusion [BBRK95] or directly through a change of the Ehrlich-Schowebel barrier. The difference in lattice constant of substrate and film and a possible tendency of substrate and film material to alloy (intermixing) can influence the evolution of the film morphology [Dij00].

Lattice misfit

The lattice misfit f is defined by

$$f = \frac{b-a}{a} \tag{1.2}$$

where a and b are the lattice constants of substrate and film. For the heteroepitaxial system Si on Ge ($a = 5.66$Å, $b = 5.43$Å), the misfit is $f = -4.1\%$. A heteroepitaxial film can either grow in a *commensurate* way or in a *incommensurate* way. *Pseudomorphic* growth is a special case of commensurate growth: In this case, the film takes on the in-plane lattice

constant of the substrate, while the distance between the layers of the film is contracted or expanded by elastic strain to keep the atomic volume constant. If the growth is not pseudomorphic, the film takes on an in-plane lattice constant different from the one of the substrate. Then, a misfit dislocation network can be imposed.

Intermixing

For heteroepitaxial growth systems, different kinds of intermixing phenomena can occur, e.g. indiffusion of the film material into the substrate or segregation of the substrate material through the film and on top of it. Besides on various free energies, the occurrence of intermixing phenomena depends on many growth parameters e.g. sample temperature, deposition rate, surface roughness, substrate and film materials, presence of surfactants etc. As a consequence, growth experiments that are significantly influenced by intermixing phenomena result in films and substrates being alloys with compositions of the two materials that can vary strongly with the thickness of the film or the depth into the substrate, respectively. It would therefore be desirable to let the growth experiments take place under circumstances that prevent intermixing phenomena in order to reach smooth and chemically sharp interfaces between film and substrate.

For the system Si on Ge(100), the conclusions that can be found in the literature about allegedly safe growth parameters relating to intermixing are contradictory. Hoeven et al. conclude that above 680 K a significant diffusion of Si into Ge occurs [HAL89, Hoe90, AKBB96]. However, other authors report that even at temperatures as low as room temperature intermixing phenomena can occur at the very surface [LMC92, QSL00, KT89]. Authors often consider sample temperatures as decisive growth parameter for intermixing phenomena. However it should be pointed out that such a so-called safe temperature always depends on the other growth parameters used for the individual experiment, under which most importantly the acting time-scale. This will play an important role in chapter 5.

1.2 Experimental techniques

1.2.1 SPA-LEED

SPA-LEED is the diffraction technique that has been used for the characterisation of the semiconductor surfaces before, during and after the experiments described in this thesis. Horn-von Hoegen has given a detailed description of SPA-LEED in his review article [HvH99]. The device (manufactured by Omicron Vakuumphysik GmbH, see fig. 1.4 for a schematic drawing) is equipped with a fine focus electron gun (LaB_6-Filament), an

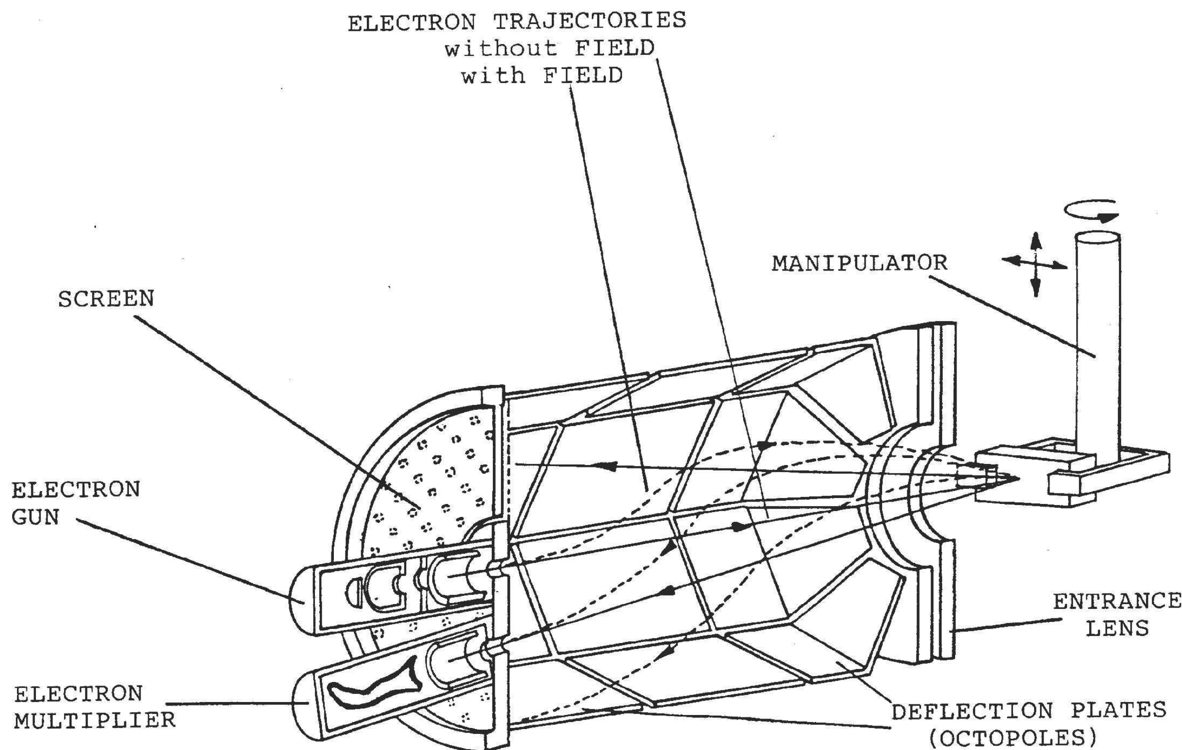

Figure 1.4: Schematic drawing of the Omicron SPA-LEED.

electrostatic deflection unit (octopole deflection plates) and a channeltron single electron detector. Compared to the electron gun of a conventional LEED, the high brightness electron gun gives a more monoenergetic and especially spatially collimated electron beam. As a result, the instrument will have a much larger transfer width than a conventional LEED instrument (approx. 1200 Å compared to approx. 150 Å) [Jor97, Dij00]. The SPA-LEED instrument can be used in two modes. In the optical mode, the diffraction pattern is made visible on a fluorescent screen, like in a conventional LEED. In the channeltron mode, the diffraction pattern is moved by the deflection unit over the small channeltron aperture. By measuring the diffraction pattern intensity with the channeltron, a digital image of the pattern can be recorded. The electron optics has been designed in such a way that the position of the electron beam on the sample does not change during such a recording if the sample is at the optimal distance to the SPA-LEED instrument [2].

[2]During molecular-beam epitaxy (MBE) real-time growth experiments the distance between sample and SPA-LEED instrument has to be increased to allow that material coming from the evaporator can reach the sample (see 1.3.1).

Phase conditions

Kinematic phase conditions S_z can be calculated from the electron energy E and the inner potential ϕ (in units of eV) and the vertical atomic layer distance h (in units of Å) of the surface [Jor97] (for an angle of incidence of the electron beam parallel to the surface normal and using the De Broglie wavelength of the electron; $\tilde{E}_0 = 150.4 eV Å^2$):

$$S_z = 2 \cdot h \cdot \sqrt{\frac{E + \phi}{\tilde{E}_0}}$$

Electron energies that lead to $S_z = 1, 2, 3, \ldots$ for the given surface fulfil the so called *in-phase* or *Bragg* condition; the *out-of-phase* or *anti-Bragg* condition is present when $S_z = 0.5, 1.5, 2.5, \ldots$ Under in-phase conditions the electrons that are scattered from adjacent terraces interfere constructively. For out-of-phase conditions the electrons interfere destructively, providing great sensitivity to surface roughness. The electrons are not annihilated but redistributed into broadened *wings* surrounding the sharp diffraction spot [HvH99]. Provided a peaked step distribution is present on the surface, these wings are peaked too and often referred to as *Henzler rings*.

Real-time growth measurements

SPA-LEED can be used for the monitoring of surfaces during manipulation, especially growth experiments, by continuously measuring the intensities of selected ranges of the diffraction pattern throughout the whole experiment. These measurements are called *real-time measurements*. It is the aim of the real-time measurements during growth to draw conclusions about the present growth mode (see above). Under out-of-phase conditions, layer-by-layer growth would result in oscillations of the diffraction spot intensities during deposition (e.g. for Si on Si(111) at higher growth temperatures, see chapter 3). The origin of the oscillations is the periodic variation of the surface morphology during deposition [GH82, HvH99]. A growth mode combined of layer-by layer growth and 3D-growth should be measurable as a exponential decay of the intensity modulated with an intensity oscillation. A less oscillatory character of the out-of-phase intensity is indicative of increasing roughness of the growth front. Close to ideal three-dimensional growth, the out-of-phase intensity should exponentially decay with the amount of evaporated material (e.g. Si on Si(100) at low temperatures, see chapter 3).

1.2.2 STM

For the STM scans that are presented in this thesis, a commercially available room temperature STM from Omicron Vakuumsysteme GmbH was used (STM1, see [Wul97, WZH+98,

ZEvL92]).

1.2.3 Ellipsometry

Set-Up

The optical properties of the thin Si films grown on Ge were analysed with spectroscopic ellipsometry. For this a home build instrument was used, extensively described in [Wen96]. It consists of a 75 W Xe arc source which emits unpolarized light. A parallel beam was created by positioning a pinhole just in front of the quartz housing of the lamp and only one quartz lens (f=200 mm). The size of the beam was determined by a 2 mm aperture behind the lens. A Glan-Thompson polarizing prism with a beam deviation of less than 30" was rotated at 67 Hz to complement the incoming beam of a rotating polarizer ellipsometer set-up. The reflected beam was analysed with a second Glan-Thompson polarizer that could be set to a fixed angle with an accuracy of 0.01 deg. An Oriel 7240 monochromator and a EMI-QB-S20 photomultiplier were used for the wavelength sensitive detection of the beam. On the UHV system lowstrain fused quartz windows are used to minimize polarization effects of the windows.

Signal Analysis

With ellipsometry it is in principle possible to determine thickness and optical properties of thin films. However the films considered in this work are only a few monolayers thick, i.e. ultra thin. This makes the analysis of the optical properties and thickness of the layers difficult. To enhance the sensitivity, a differential optical measurement was performed in which first the sample after deposition is measured. After this the sample was cleaned by Ar sputtering and annealing. A second, reference measurement, was done from this clean sample without changing the incident and exit angle of the instrument. This provides a differential measurement that eliminates many systematic errors present in an absolute measurement.

In ellipsometry, one measures the ratio of the parallel (p) and perpendicular (s) reflection coefficient of the surface:

$$\rho = \frac{\widetilde{r}_p}{\widetilde{r}_s}$$

These reflection coefficients can be calculated for a particular stack of layers that make up a sample if the thickness and optical properties of these layers are known. At every optical interface separating two layers the reflection and transmission is determined by the well known Fresnel coefficients $\tilde{r}$. For this the complex refractive indices $\widetilde{n}_i$ and $\widetilde{n}_e$ of the material above and below the interface have to be known as well as the angle of incidence

$\widetilde{\theta}_i$ and refraction angle $\widetilde{\theta}_e$ in the two media at either side of the interface. The Fresnel coefficients for the parallel (p) and perpendicular (s) polarised ligth are:

$$\begin{aligned}\widetilde{r}_{p,ie} &= \frac{\widetilde{n}_e \cos\left(\widetilde{\theta}_i\right) - \widetilde{n}_i \cos\left(\widetilde{\theta}_e\right)}{\widetilde{n}_e \cos\left(\widetilde{\theta}_i\right) + \widetilde{n}_i \cos\left(\widetilde{\theta}_e\right)} \\ \widetilde{r}_{s,ie} &= \frac{\widetilde{n}_i \cos\left(\widetilde{\theta}_i\right) - \widetilde{n}_e \cos\left(\widetilde{\theta}_e\right)}{\widetilde{n}_i \cos\left(\widetilde{\theta}_i\right) + \widetilde{n}_e \cos\left(\widetilde{\theta}_e\right)}\end{aligned}$$

Of course the angle of incidence is real if the medium is vacuum (no light absorption), but will be complex if the medium absorbs light as follows from Snell's law:

$$\widetilde{n}_i \sin\left(\widetilde{\theta}_i\right) = \widetilde{n}_e \sin\left(\widetilde{\theta}_e\right)$$

For a so-called three layer system, namely a bulk material covered with a thin layer of thickness d, and vacuum, which represent our samples quite accurately, the reflection of the surface is influenced by interfering light beams that are reflected and transmitted by the two interfaces. Upon travelling between the two interfaces, the light beam obtains a phase change depending on the wavelength of the light λ, the refractive index of the layer and the angle.

$$\phi = \frac{2\pi\lambda}{d}\widetilde{n}\cos\left(\widetilde{\theta}\right)$$

The total reflection of the tree-layer system $\widetilde{r}_{123}$ can than be calculated for both s and p polarization separately, with (1) the ambient (vacuum), (2) the thin layer and (3) the bulk of the sample:

$$\widetilde{r}_{p(s)123} = \frac{\widetilde{r}_{p(s)12} + \widetilde{r}_{p(s)23}e^{2i\phi}}{1 + \widetilde{r}_{p(s)12}\widetilde{r}_{p(s)23}e^{2i\phi}}$$

For very thin layers, i.e. with a thickness much smaller than the wavelength of the light, a Taylor expansion of the exponential phase factor can be made. With a Taylor expansion to the second order the ratio of the response of a three layer system (with a thin film of thickness d) with respect to the two layer system (thickness of the film zero), one can evaluate:

$$\begin{aligned}\frac{\widetilde{\rho}_{123}}{\widetilde{\rho}_{13}} - 1 &= \frac{\widetilde{r}_{p123}}{\widetilde{r}_{s123}} / \frac{\widetilde{r}_{p13}}{\widetilde{r}_{s13}} - 1 = \frac{2ieE}{\hbar c}\frac{\cos\left(\theta_1\right)}{1-\widetilde{\varepsilon}_3}\frac{\widetilde{\varepsilon}_3 \sin^2\left(\theta_1\right)}{\widetilde{\varepsilon}_3\cos^2\left(\theta_1\right) - \sin^2\left(\theta_1\right)}\widetilde{J} \\ \widetilde{J} &= d\left(\widetilde{\varepsilon}_2 - \widetilde{\varepsilon}_3 + \frac{\widetilde{\varepsilon}_3}{\widetilde{\varepsilon}_2} - 1\right)\end{aligned}$$

E denotes the photon energy of the light, e, $\hbar$ and c are the electron charge, Planck's constant an the speed of light and the refractive index of vacuum, 1, was substituted and instead of the refractive index, the dielectric function $\widetilde{\varepsilon}$ was used. The dielectric function

is used in this expression instead of the refractive index, because the imaginary part of the dielectric function can be interpreted as the amount of light absorption of a medium. From this equation it is obvious that the influence of the thin layer on the optical response of the total system is limited to the so-called ellipsometric invariant J. The rest of the variables in the measurement can be considered as a prefactor. The interpretation of J is, however, not straightforward, already from a mathematical point of view. For every energy point it has both a real and imaginary part. The number of unknowns are next to the thickness of the film a real and imaginary part of the dielectric function of the layer for every photon energy. Also the expression of J is quadratic in this dielectric function. As the thickness of the layer is known from the experimental set-up, the only task is to select the right roots of the quadratic expression. In this way the optical absorption of the thin layer grown was calculated in this work.

1.3 Experimental setup

1.3.1 UHV system

The electron diffraction measurements described in this thesis have been performed in the so called *ARA* UHV system, which is shown in fig.1.5. For this purpose, an existing ellipsometry UHV system (described in [Wen96], chapter 2.1) has been equipped with a commercial Spot Profile Analysis LEED (SPA-LEED) [SMH86, GH82, Jor97, HvH99]. The base pressure is $p_0 = 1.3 \cdot 10^{-11}$Torr. The experience with sample preparation during the experiments show in accordance with the latest publications [HKOS00] that especially this low base pressure is a very important prerequisite to prepare almost defect free silicon surfaces (see section 1.4).

The optimal distance between the SPA-LEED's front side and the sample during measurements is 15 mm. As the type of SPA-LEED instrument used in the ARA system is cylindrical on its whole length it has to be retracted 45 mm in order to allow the Si evaporator to be turned towards the sample for growth experiments. The evaporation angle is then 55°[3]. A negative consequence of changing the distance between sample and SPA-LEED is that the sample gets out of focus, i.e. the spot where the electron beam hits the sample starts moving over the sample as soon as the x- and y-deflection are used. Thus the maximum measurable height or width respectively of the diffraction pattern is reduced (to about 1.5 BZ) due to the limited sample dimensions as long as the internal SPA-LEED

[3]The necessity of pulling back the SPA-LEED apparatus is a consequence of using MBE for the growth experiments. CVD would allow that the SPA-LEED stays at its optimal distance to the sample [MzHGG+00].

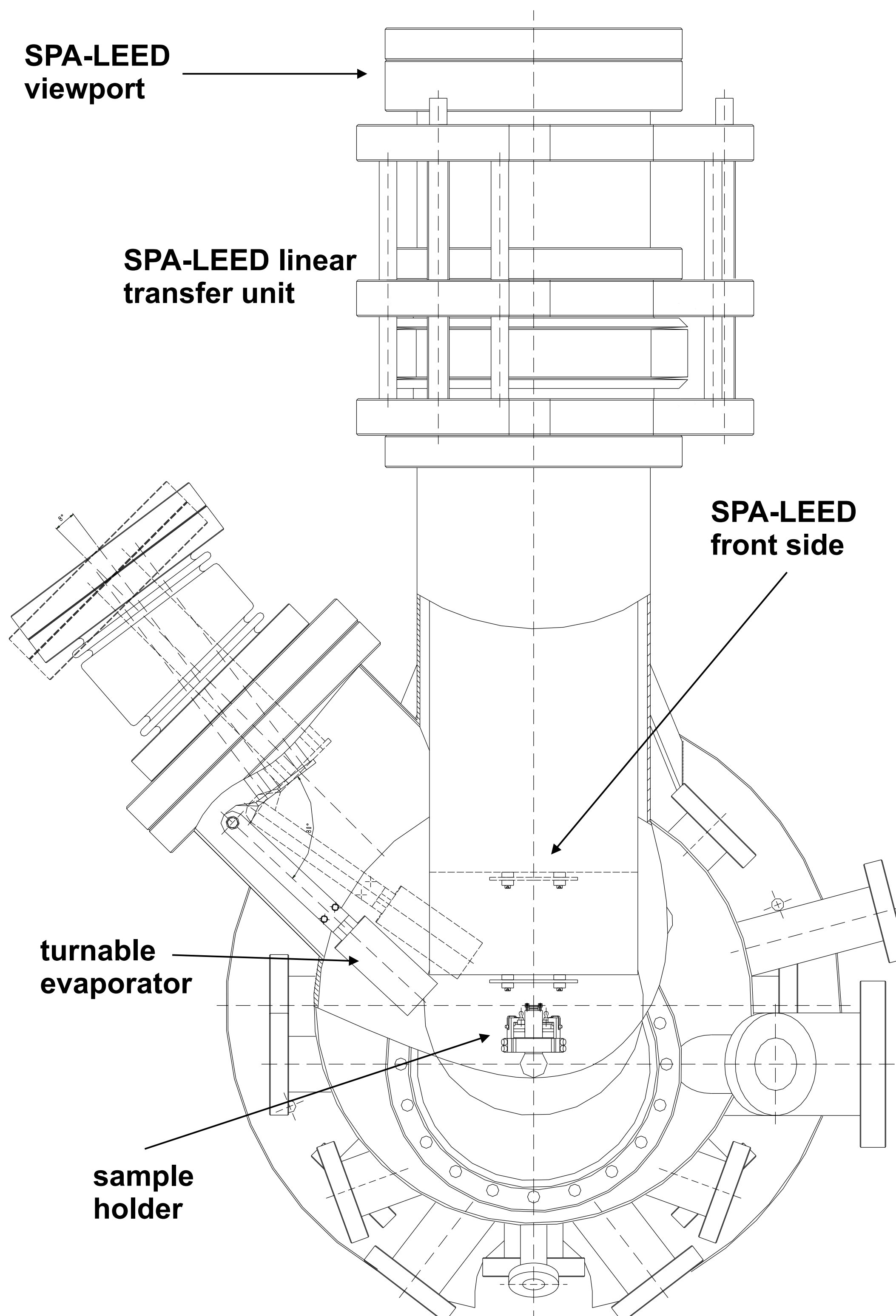

Figure 1.5: Top view ARA UHV system's main vacuum chamber. The SPA-LEED is mounted on a linear transfer unit. For the real-time intensity measurements during growth experiments the SPA-LEED is pulled back and the evaporator is turned towards the sample.

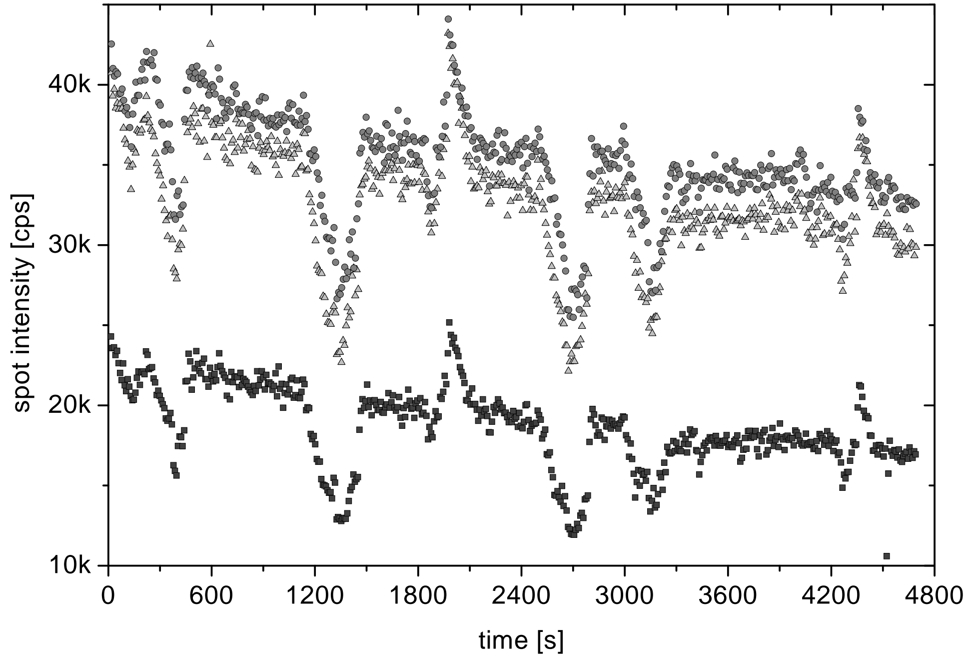

Figure 1.6: Disturbing influence of varying external magnetic fields (sweeping range -3 T < B < 3 T) on SPA-LEED measurements: Central spot intensities at three different electron energies measured on a Si(111) surface at about 525 K.

focus settings are not changed [4] [5].

The SPA-LEED itself is shielded with a μ-metal cylinder against external magnetic fields. Still, the SPA-LEED measurements are very sensitive to such fields, especially when the SPA-LEED is retracted from the sample. Fig. 1.6 displays the long-term behaviour of the intensity of the central peak in the profile of the specular beam from a clean Si(111) surface, measured at three different electron energies [6]. The sample was kept untouched; all the measured sudden changes in spot intensity were caused by a sweeping magnet (sweeping range -3 T < B < 3 T) that was located at a distance of 8m. Thus special care has to be taken, even if the external magnetic fields seem to be negligible.

The STM measurements presented in this thesis were performed in a different UHV system (in-situ) (see [Wul97, WZH+98, ZEvL92] for a detailed description).

[4] The focus settings have not been changed. If necessary, the SPA-LEED was moved forward to its optimal position after growth experiments.

[5] A modernized version of SPA-LEED has a conical front [HvH99]. Because of this improvement, it has to be retracted less to allow evaporation at similar angles.

[6] As the sample temperature is slightly rising, the intensities are slightly decaying.

1.3.2 Samples

Silicon and Germanium samples are broken out of 2 and 3 inch wafers. To facilitate the breaking procedure, a pattern of lines is scratched on the wafer's backside using an commercial CO_2 cutting laser. Light scratches are sufficient, if they are aligned with the symmetry lines of the crystal. Special attention has to be paid to avoid contact of the wafers or samples with metals during the whole preparation process and the entire experiment. To prevent contamination, the wafers/samples are only touched with specialized teflon tools. Find details about the wafer material in the following:

Si(111) 2 inch by 0.3 mm, polished, n-type, $\approx 2000\Omega$cm

Si(100) 3 inch by 0.375 mm, polished, p-type (Boron), $\approx 1000\Omega$cm, miscut $< 5/100°$

Ge(100) 3 inch by 0.5 mm, polished, n-type, $\approx 25\Omega$cm , miscut $< 5/100°$

1.3.3 Sample holder

The ARA UHV system is equipped with a load lock and transfer stick, the sample holder (see fig.1.7) is connected to the manipulator by a bayonet construction that enables both electrical connections for sample heating or temperature measurement respectively and thermal connection with a liquid nitrogen dewar for sample cooling. The sample holder can hold 6×30mm samples, with a thickness up to 0.5mm. To prevent any contact of the samples with stainless steel or other metals (see above), they are clamped to Mo electrical contacts using Mo springs. No thermocouple is used to measure the sample temperature during the experiments as thermocouples are also possible sources of contamination[UDYJ97]. During the initial degassing of new samples and flashing for preparation, the samples are heated resistively using direct current. During real-time SPA-LEED measurements the samples are heated indirectly from behind by a tungsten band filament (width 1 mm, thickness 0.01 mm), with the sample itself remaining at zero potential. This prevents possible disturbances of the SPA-LEED electron optics. The heating filament is also helpful when the maximum voltage of the resistive heating power supply is too low to heat up high resistance samples. In case of high sample temperatures, the temperature is determined by pyrometry. For low temperatures calibration measurements were performed with a Pt100 resistor is pressed against a dummy sample. All temperature measurements have been verified by sample resistivity measurements. Fig. 1.8 shows the sample temperature calibration graph for Germanium and indirect sample heating. The maximum sample temperature that can be reached using the heating filament is about 525K. It is limited by the electrical contacts of the sample holder with the manipulator. The contacts heat up

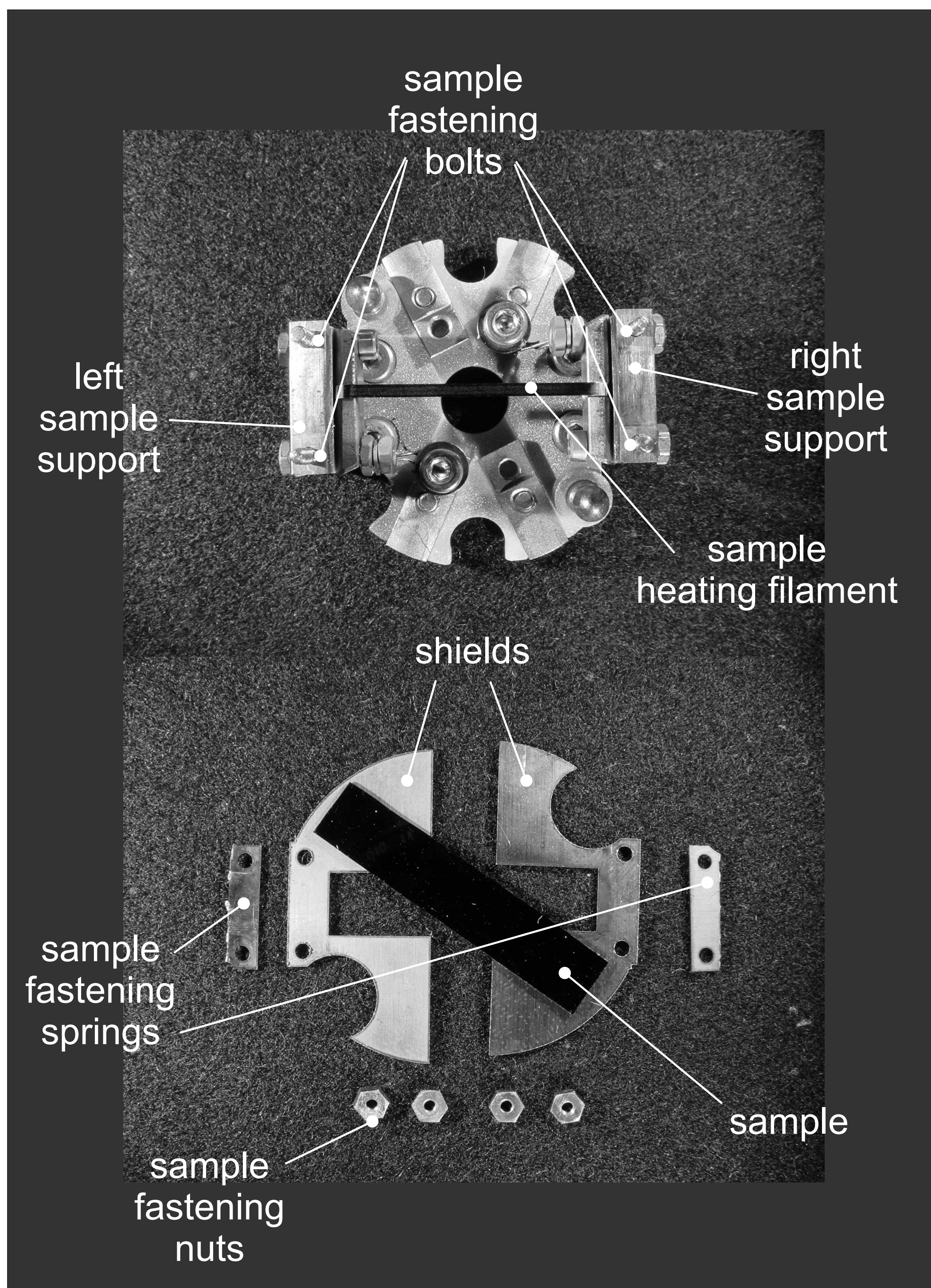

Figure 1.7: Sample holder. The sample (cut to a size of 6×30 mm) are mounted on the sample supports using the bolts, springs and nuts. Right behind the sample (distance to sample less than 1 mm) is a tungsten band filament of the indirect sample heating. The shields are also mounted behind the sample to prevent electrostatic charging of the ceramic back plate of the sample holder. All parts that are in the vicinity of the sample are made from either molybdenum or tungsten to prevent sample contamination.

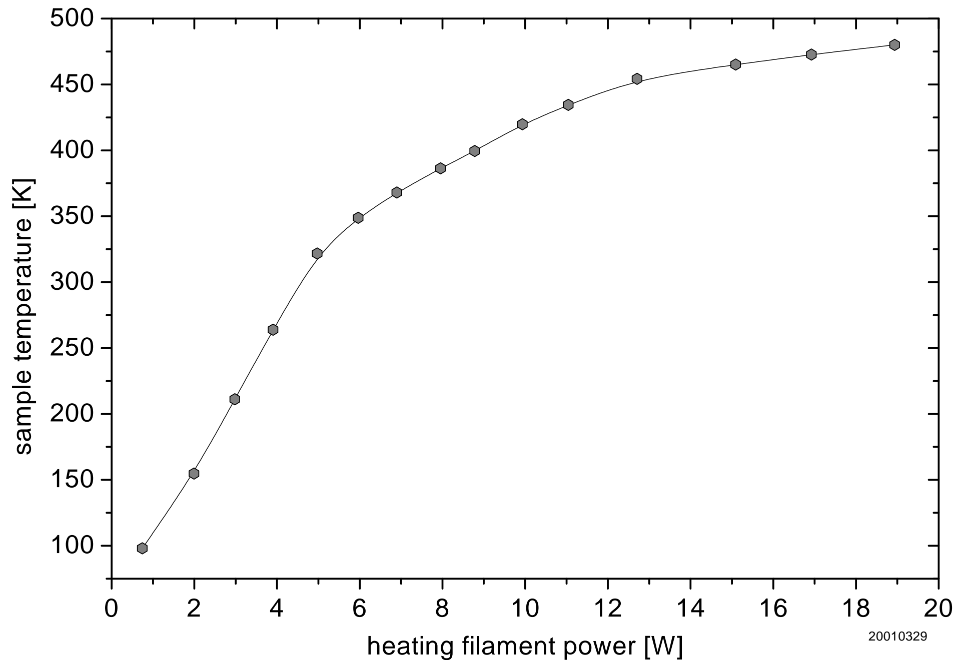

Figure 1.8: Ge sample temperature vs. indirect sample heating filament power

too much above a certain current and cause a rising pressure, whereas at the maximum sample temperature, the UHV system pressure rises only insignificantly above the base pressure. The basis of the sample holder construction is made from Alumina. To prevent electrostatic charging of this isolator, a Mo shield covers the side of the sample holder facing the SPA-LEED instrument.

1.3.4 Sample cooling

Although the manipulator of the ARA UHV system was constructed to allow sample tranfer, it was possible to install a sample cooling that cools sample and sample holder down to 100 K (see fig. 1.9). As a consequence of the cooling of the sample and its environment, the system pressure during flash preparation of the samples stays much lower than without cooling resulting in more defect free surfaces. This way, lower system pressures are also achieved during real-time SPA-LEED measurements when the samples have to be heated indirectly. The cooling compensates the heat dissipation to the sample holder very efficiently.

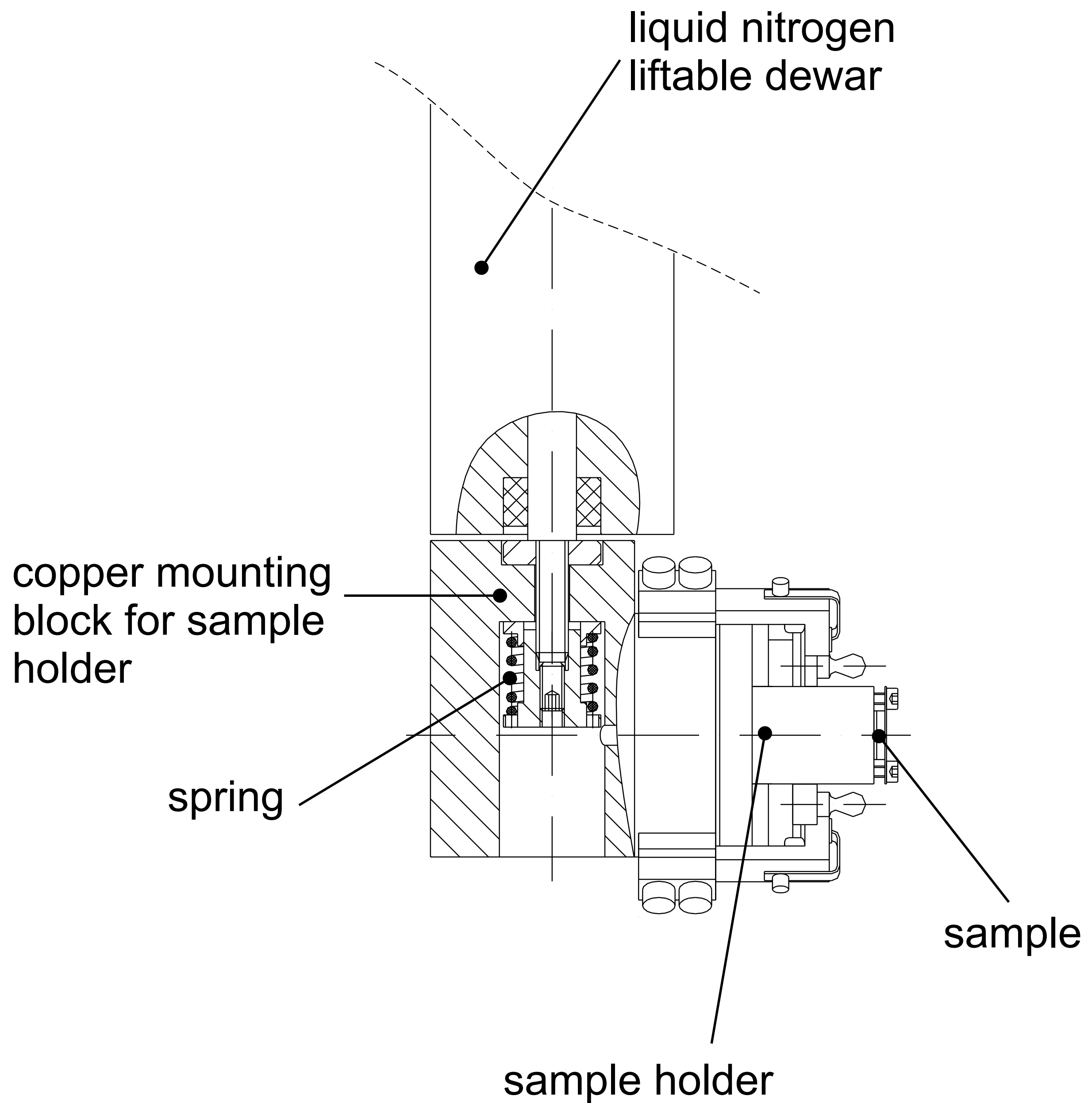

Figure 1.9: Sample cooling of the ARA UHV system. When the liquid nitrogen dewar is lowered, a spring presses the copper mounting block against the lower side of the dewar to improve the thermal conductivity.

1.3.5 Evaporator

It is not a trivial problem to find a suitable Si evaporator for the intended growth experiments. Evaporators with electron beam heated crucibles or evaporation material are suspected to influence the growth because the ionised part of the evaporated material is accelerated towards the sample (in case of the commercially available e-beam evaporators) and can cause sputtering-like effects when hitting the surface. Radiation-heated crucibles made of ceramic materials (Alumina, Quartz) with tungsten filaments wrapped around showed to be qualified to create good evaporation rates (as the evaporation material could be heated above its melting point), but the evaporated material (Si) was oxidized at a high-grade by oxygen originating from the crucible material. Recently, the same experience was reported by Michely et al. as they tried to evaporate aluminium from Alumina crucibles. The type of evaporator that was finally used for the experiments contains a Si rod of quadratic cross-section (1×1 mm, leated length 10 mm, cut from a single crystal) that is heated by direct current. This approach allows a very small holder construction (see fig. 1.5)that meets the requirements for real-time SPA-LEED measurements during growth experiments: It can be turned towards the sample after retracting the SPA-LEED apparatus. The holder for the Si rod is made from pure Mo, the degassing even during long evaporation experiments of many hours is negligible. The evaporation rates that are typically reached are between 3 and 8 ML per hour (currents of about 4.5 - 5.5 A). Higher evaporation rates drastically lower the lifetime of the Si rod as it has to be heated to temperatures too close to the melting point. The influence of the radiation originating from the evaporator on the sample temperature is negligible if the sample cooling is active.

1.4 Sample preparation

Defect free surfaces are the key to well defined experiments on silicon and germanium surfaces, as defects are known to influence processes like growth, adsorption, oxidation etc. The defect density can depend very much on the sample preparation method in use.

1.4.1 Automatic sample preparation

A thorough, fast and reproducible sample preparation is facilitated by the fact that the new experimental control software (WinSPA32, see chapter 2) can perform automatic sample degassing and/or sample preparation (as long as the sample in question can be prepared using heat treatment only). A maximum degassing system pressure and a recovery system pressure can be defined limiting the degassing current during interval or constant heating of the sample (directly or indirectly). In this way especially samples (and the holders) that

have just been introduced into the vacuum system can gently and evenly be automatically degassed over night, being ready for later flash preparation. In case of a failure of the UHV pressure gauge, the software responds fail-safe and stops all degassing activities.

1.4.2 Silicon

The basis for standard procedures for silicon sample annealing and flashing has been described in [SMWL89]. Further developed procedures are widely used. For the experiments described here, another modified procedure led to optimal results for both Si(111) and Si(100) samples (sample dimensions $30 \times 6 \times 0.375$mm) [7]:

1. if the sample is new[8], it is degassed automatically up to 600°C in intervals for 24h using resistive heating by direct current (up to I=1.2A)
2. the sample is heated from -175°C to 900°C (I=5A) in 5s, and further to the flash temperature of 1100°C (I=11A) in 0.1s using resistive heating by direct current
3. after 5s the sample is quenched by switching off the heating current
4. the sample cools down for about three minutes
5. repeat from step 2 for 3–5 times (depending on the amount of degassing during the flash)

This procedure leads to silicon surfaces with low defect densities (minimum of diffuse scattering in LEED) and wide terraces. For the FWHM of the central diffraction peak, usually values of about 0.5 % BZ are measured.

In a recent publication [HKOS00] Hata et al. show a similar procedure to prepare a nearly defect free Si(100) surface, they furthermore state necessary secondary conditions of the UHV system and the sample holder. One of their most important conclusions is that an increase of the system pressure during flashing due to degassing of the sample environment has to be avoided as much as possible. During the flashing the pressure in the ARA system is rising only insignificantly above the base pressure ($p_0 = 1.3 \cdot 10^{-11}$Torr), thanks to the cooling of the sample holding construction that prevents efficiently the heating up and therefore the degassing of the sample environment[9], filaments of all the other devices attached to the ARA system are switched off at that time.

[7] Before this procedure can be applied, the sample holder must be degassed very thoroughly.

[8] Before introduction into the UHV system, silicon samples undergo a 5min ultrasonic cleaning process in isopropanol at 80°C.

[9] In case of samples that have just been introduced into the experimental set-up, the amount of degassing can be higher. In this case flashing is interrupted as the system pressure rises above $5.0 \cdot 10^{-11}$ Torr. Flashing is then repeated till there is no significant degassing any more.

Direct current heating can have important consequences for the surfaces of the silicon samples. On Si(111) the steps can form bunches, separated by wide terraces[LAKS89, YY93, DMTY00]. On Si(100) S_A and S_B steps can move towards each other to form double steps, resulting in a (2x1) or (1x2) single domain like structure[KY89, Sto90]. To prevent these effects, the polarity of the direct current is changed before every repetition of step 2 the preparation procedure. LEED spectra of Si(100) samples taken after sample preparation don't show significant intensity differences of the (2x1) and (1x2) reconstruction spots, thus indicating a homogeneous contribution of terraces with monoatomic height distance belonging to the two species.

1.4.3 Germanium

To obtain Ge surfaces of high quality, preparation steps similar to those described for Si are used (heating currents and heating times are identical with steps 1-5, sample dimensions $30 \times 6 \times 0.5$mm). The preparation method is is supplemented by noble gas ion sputtering before the treatment at elevated temperatures. Because heteroepitaxial growth experiments are performed on the Ge surfaces, sputtering is not only necessary for the actual preparation process but especially for the thorough removal of the evaporated material before the preparation. After typical Si evaporation experiments with a grown film of 10 ML a two hour sputter treatment (Ar^+ ions, Ar partial pressure $2 \cdot 10^{-5}$ Torr, acceleration voltage 800 eV, incoming ion current on sample 1 μA) in combination with the thermal treatment described above leads to flat surfaces with an extremely low defect density.

It turned out that the condition of the c(4x2) spots in the SPA-LEED diffraction pattern can be used as indicators for the surface quality of the Ge(100) samples. The preparation cycles consisting of ion bombardment and thermal treatment should be repeated till the c(4x2) are sharp, symmetric and intense. In contrast, unsharp, streaky or moderately intense c(4x2) spots indicate that the preceding preparation was insufficient. This holds both for samples that have been introduced to the vacuum system shortly before and for samples that were used for heteroepitaxial growth experiments.

Chapter 2

Improvements in SPA-LEED data acquisition

2.1 Introduction

Most research groups with a SPA-LEED apparatus at their disposal use it only for conventional a priori/posteriori characterization of surfaces, i.e. they mainly measure one- and two dimensional diffraction intensities at one particular energy to characterize surfaces after preparation or manipulation [EHO+00, GMG+00, SC00, HMzHZHvH00, SLI+00, HPL+99, IGWM99, WVT+99, CdRM+99, MRZH99, CMdR+98, CDvdGR+98, SESK98, GBBvB98, BFL+97, NSS+97, LFS+97, MFL+96, LWWM96, BPR+95]. This is quite surprising, because more involved SPA-LEED applications and measurement procedures have been known for many years: Gronwald et al. [GH82], Altsinger et al. [ABHM88] and Horn et al. [HGH88] have already reported in the 1980s about their real-time diffraction spot intensity oscillation measurements during homoepitaxy on Si(111) and Si(100). Later, real-time diffraction spot intensity measurements during growth were intensively studied by Wollschläger et al. [WM96, NMF+97, PKMW97, WES98]. More elaborate intensity measurements (also known as *k-space-scans* or *Heringplots*, see 2.3) have been described by several authors [BAN96, KJW+00] and nicely refined by Meyer zu Heringdorf et al. [MzHGG+00, MSY+00, MZVHvH98, MYMzH+99].

Then, why are just a few SPA-LEED users applying the extended types of measurements? The reason can be found in the SPA-LEED's standard peripherals that are provided by the manufacturer of the instrument: The electron energy remote control[1] that

[1] The electron energy remote control enables that the energy of the LEED electrons can be set remotely from the data acquisition software. Without it, the operator of the apparatus has to manually set the electron energy at the SPA-LEED power supply.

is necessary for the greater part of the extended types of measurement is not functioning and has to be implemented by the user[2]. Additionally the data acquisition software[3] only supports the simple types of measurements in an acceptable way. Time- and energy-dependent measurements rely heavily on the ability to measure spot intensities with a high dynamic range without loosing the particular spot. Furthermore, in static one- and two-dimensional measurements, the main spot itself does not change for the duration of the measurement. That's why both data acquisition hard- and software have to be adapted to enable the enhanced types of measurements, probably being the main reason for their limited spreading.

The ARA UHV system (see chapter 1) has SPA-LEED as a main technique for surface analysis. That's why extended types of SPA-LEED measurements are intensively called for. These measurements make high demands on the data acquisition software, mainly due to the fact that the diffraction pattern can slightly drift during the dynamic experiments. On the one hand, the software should be able to compensate drift in a very reliable way, on the other hand the user interface of the software should keep the experimentalist up to date about possible problems of the measurement and give the possibility to adapt important parameters of the measurement at any time. The standard data acquisition software with its limited drift compensation and poor user interface does not fulfil these demands.

That's why *WinSPA32* was developed, a novel improved software allowing both the extended types of measurements and the simpler conventional types. With the implementation of the electron energy remote control, an important drawback of the commercial instrument was eliminated. In addition, numerous useful features were added to increase the software's functionality like the remote controllability of key experimental parameters (e.g. sample temperature and evaporation rate of the MBE source). WinSPA32 runs under 32-Bit Windows operating systems as a native Windows application and is that's why fully integrated into the hardware periphery (especially the LAN[4]). With these extensions, WinSPA32 has become an integrated experimental control system with new features such as macro-programmable experiments and the possibility to remotely control the experimental set-up remotely, also via LAN/WAN[5](Internet).

In the next sections several key aspects of the software are discussed: The spotfinder (see section 2.2) is responsible for fast and precise position determination of diffraction spots. Compensating possible spot drift, it enables reliable dynamic SPA-LEED mea-

[2]The SPA-LEED power supply may have a analogue input to control the electron energy remotely, but the corresponding DA converter is missing on the Burr-Brown data acquisition board.

[3]SPASO V4.1d, © by OMICRON Vakuumphysik GmbH, developed by the Institut für Festkörperphysik, Universität Hannover, Hannover, Germany

[4]Local Area Network

[5]Wide Area Network

surements. Based on the spotfinder, extended one-dimensional intensity measurements become possible (see section 2.3). In section 2.5 WinSPA32's capabilities to characterize the SPA-LEED's lens aberrations are presented. They form the basis for a future automatic aberration correction during diffraction intensity scans.

2.2 Spotfinder class

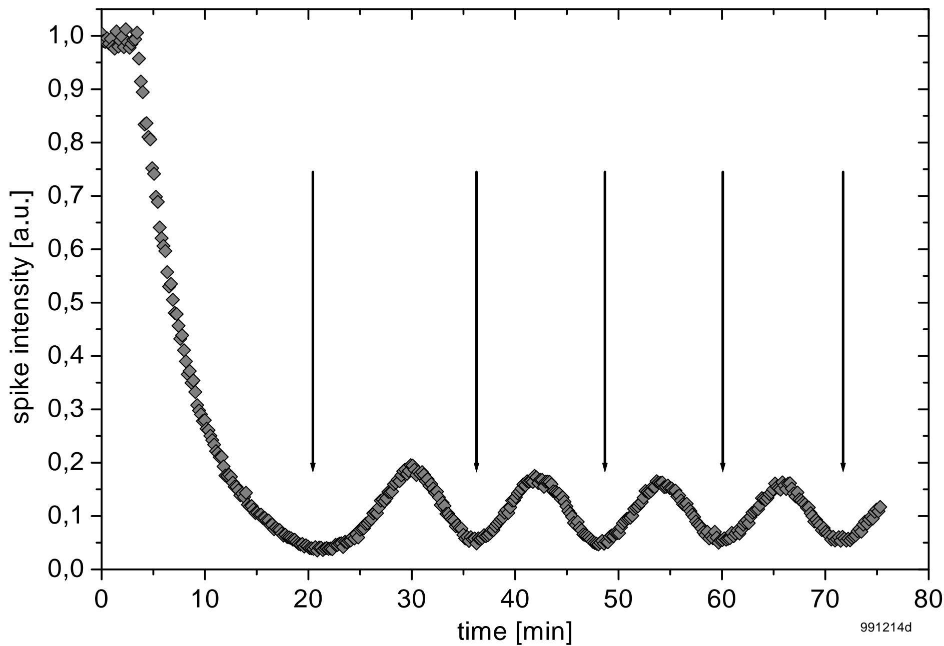

Figure 2.1: Real-time measurement of the central spot's spike intensity during homoepitaxy on Si(111) (sample temperature 498 K) at out-of-phase condition (see section 1.2.1, s=2.5, E=83.0 eV). Crucial for the reliability of the spotfinder are the intensity minima (marked with arrows). A reliable spotfinder does not lose its spot, even if the spot's peak is hardly distinguishable from the background noise.

A typical application for the SPA-LEED instrument as a real-time probe is the automatic continuous measurement of multiple spike intensities of diffraction spots during for example a growth experiment (see fig. 2.1, [HvH99]). The spikes of diffraction spots can be very sharp (just a few per mil of a BZ) and their intensities orders of magnitude higher than the surrounding (diffuse) parts of the spots. Also the reverse situation occurs in which spots are at times only barely discernable from the background. Taking possible slight spot drift into consideration it becomes clear that the exact determination of the spike's po-

sition is of key importance for the reliability of the real time intensity measurement. In WinSPA32, the quality of the *spotfinder* class [6] is responsible for that task.

2.2.1 Center-of-intensity algorithm

To determine the spike's position, the spotfinder class first of all measures a two dimensional array $I_{1\ldots n_x,1\ldots n_y}$ of intensity values with the coordinates $\vec{r}_{i,j} = (x_{i,j}, y_{i,j})$ around the last known spot position $\vec{r}_{old} = (x_{old}, y_{old})$. The new coordinates of the spot's spike are calculated using a centre of intensity (CoI) algorithm. To make sure that only intensity values originating from the spike itself and not from the diffuse part of the spot will influence the calculation of the CoI, the intensity array is filtered in the following way:

$$I^*_{i,j} = \left\{ \begin{array}{ccc} I_{i,j} & \text{if} & I_{i,j} \geq f \cdot I_{old} \\ 0 & \text{if} & I_{i,j} < f \cdot I_{old} \end{array} \right\}$$

where I_{old} is the last measured spike intensity and f the filter factor (typically $f = 0.5$, that means that the upper half of the spike intensities are used for the CoI calculation). Then, the new spike coordinates $\vec{r}_{new} = (x_{CoI}, y_{CoI})$ are calculated as

$$x_{CoI} = \frac{\sum_{j=1}^{n_y} \sum_{i=1}^{n_x} I^*_{i,j} \cdot x_{i,j}}{\sum_{j=1}^{n_y} \sum_{i=1}^{n_x} I^*_{i,j}}, \quad y_{CoI} = \frac{\sum_{j=1}^{n_y} \sum_{i=1}^{n_x} I^*_{i,j} \cdot y_{i,j}}{\sum_{j=1}^{n_y} \sum_{i=1}^{n_x} I^*_{i,j}}$$

For small spot drifts a scan width of about $1.5 - 2$ times the FWHM (full width half maximum) of the spike in x- and y-direction for the intensity array $I_{i,j}$ is sufficient. The gate time t_g for the measurement of each of the array's elements and the array's height and width n_x, n_y are chosen in dependence of the spike intensity. Typical values are $t_g = 12$ms and $n_x = n_y = 20$ for spike intensities of about 10^4cps. The time necessary for a spotfinder execution typically varies, depending on the spike's intensity, between 0.1s (for very intense spikes) and 20s (for spikes with very little contrast against the background/the diffuse part of the spot).

Once the spike's coordinates are calculated, its intensity can be measured.

2.2.2 Overshooting

In some situations, like during recording I/E curves (see 2.2.5), cases of strong, but uniform spot drift can be observed. These can effectively be eliminated by introducing the

[6] A *class* is defined in the sense of object-oriented programming (OOP) as a user defined data type which has a state (its representation) and operations (its behaviour). It has internal data and methods, in the form of procedures and functions, and usually describes the generic characteristics and behaviour of a number of similar objects (the *instances* of the class) [Can98].

overshooting factor l. With $\Delta\vec{r} = \vec{r}_{new} - \vec{r}_{old}$, the starting coordinates for the following run of the spotfinder are set to

$$\vec{r}_{overshoot} = l \cdot \Delta\vec{r} + \vec{r}_{new}$$

The overshooting factor l is user defined (typically 0.5-0.8) and can be adjusted at any time of the measurement. With l well chosen for the present drift, the width of the intensity array $I_{i,j}$ can be reduced to a smaller value resulting in a more precise determination of the spot's spike position.

2.2.3 Reliability

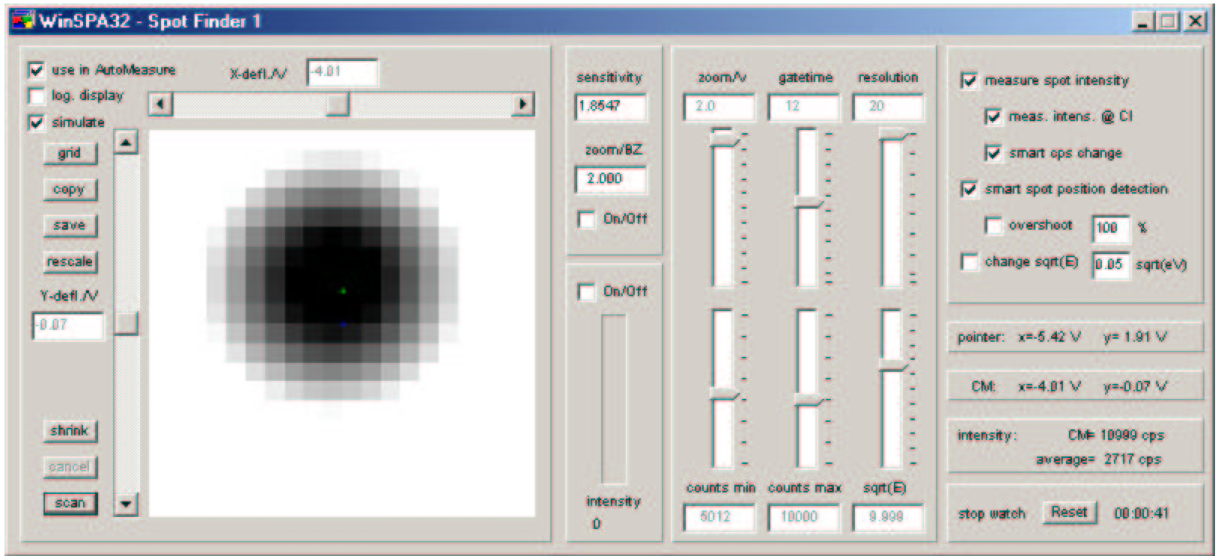

Figure 2.2: The graphical user interface of WinSPA32's spotfinder class. In the large panel on the left side of the window, the measured intensity array $I^*_{i,j}$ measured around the last known spot position $\vec{r}_{old}$ is graphically displayed. With the sliders and checkboxes on the right side of the window, the spotfinder's different parameters (e.g. gate time t_g, array height and width n_x, n_y, scan width etc.) and modes (e.g. overshooting) can be changed at any moment of a running experiment, which is essential for a reliable tracking of the spot recording and the recording of its spike intensities.

In the course of the measurements performed with WinSPA32, the spotfinder class showed that it is very reliable compared to similar routines of the standard data acquisition software. The crucial situation for the reliability of the spotfinder class during a real time measurement of a spot's spike intensity or during recording an I/E curve (see 2.2.5) is the intensity minimum as it occurs for example during epitaxial layer by layer growth

in the out-of-phase condition in the situation of maximum surface roughness (coverage $\theta = 0.5\,\mathrm{ML}, 1.5\,\mathrm{ML}, 2.5\,\mathrm{ML}, \ldots$ see fig. 2.1). In this situation there is very little or even no contrast at all between the spot's spike and the background/the diffuse part of the spot. This often leads to abrupt, runaway-like position changes to unreasonable coordinates when the spotfinder of the standard software was used in early experiments. Due to the poor user interface of the standard software, the spike position could not even be reset once the problem had occurred. The measurement had to be cancelled as a consequence.

WinSPA32's spotfinder prevents to a great extent any abrupt spot position changes. The reason for its higher reliability can on the one hand be found in the better statistics of the two dimensional intensity array $I_{i,j}$ compared to the only one-dimensional array that is used in the standard software [7] (assuming a sufficient array height and width n_x, n_y in combination with a sufficient gate time t_g). On the other hand, the special user interface of the spotfinder class (see fig. 2.2) ensures that the operator is at every moment up to date about the state of the measurement and able to manually adapt important parameters (like intensity array width or height n_x, n_y, gate time t_g, scan width) or switch from automatic to manual measuring mode as soon as the experiments runs into a critical situation.

2.2.4 Multiple instances

As WinSPA32 is running, the operator can create a maximum of ten spotfinder class instances[8]. Every instance can be set to its own deflection coordinates and electron energy. In the automatic measuring mode the instances are sequentially activated. In this way, the intensities and positions of various spots (at different phase conditions) can be measured intermittently during the same experiment. This is an important prerequisite for many of the measurement types described in the following sections (e.g. temperature dependence of central, first order and two different reconstruction spots in fig. 2.5, extended one-dimensional real-time measurement during growth in fig. 2.6 etc.). Fig. 2.3 shows exemplary the intensities of the central diffraction spot at in- and out-of-phase condition that have been recorded intermittently during homoepitaxy on Si(111).

A truly parallel measurement of several diffraction spot intensities is not possible in the channeltron mode of the SPA-LEED apparatus, but still the intermittent measurement as described above is a good approximation. The major disadvantage is of course the higher time consumption of the sequential way of measuring. Budde et al. [BSE$^+$01]

[7] Here, the spot position is calculated from intensity values that are scanned along lines or circles of the diffraction pattern.

[8] An *instance* of a class (or an *object*) is according to the definitions of object-oriented programming (OOP) a variable of the data type defined by the class. The instances (or objects) are the actual entities of the class [Can98].

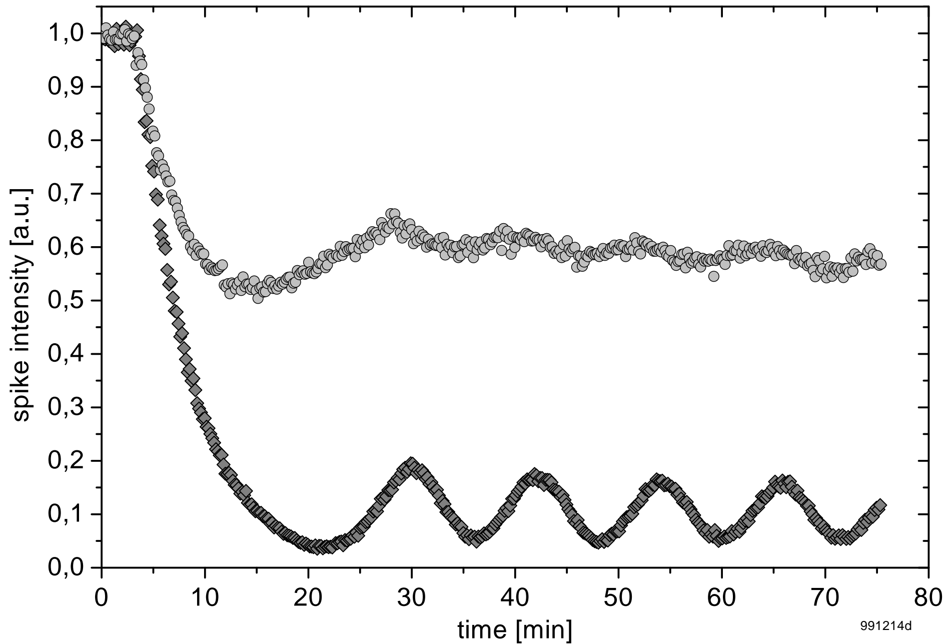

Figure 2.3: Using multiple instances of the spotfinder class, it is possible to record the intensities and positions of various spots (also at different phase conditions) intermittently during the same experiment. A Real-time measurement of the central spot's spike intensity during homoepitaxy on Si(111) (sample temperature 498 K) at in-phase (S=3.0, E=100.0 eV) and out-of-phase condition (S=2.5, E=83.0 eV) is shown.

have presented an extension of the SPA-LEED apparatus (based on a combination of phosphor screen and CCD camera) that, according to their article, allows the fast parallel measurement of diffraction spot intensities, at least for spots at identical electron energies. For the measurement of spot intensities at different phase conditions their solution is not faster, of course.

2.2.5 I/E curves

Without electron energy remote control, the recording of an I/E curve of a diffraction spot is a troublesome time-consuming matter: For every point of the curve, the electron energy has to be manually set, after that the spot has to be manually tracked down and finally the intensity of the spot's spike has to be determined. If an I/E curve with a high point density is desired, this measurement can take hours. WinSPA32, making use of the spotfinder class and the implemented electron energy remote control, can record

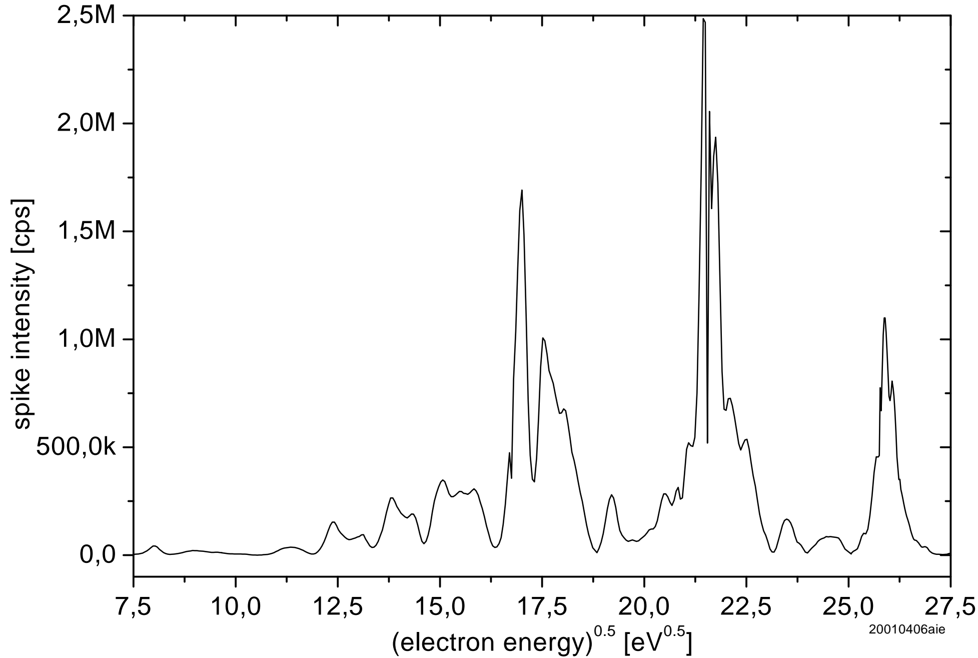

Figure 2.4: Automatically recorded I/E curve of the central spot's spike intensity of a clean Ge(100) surface at ≈ 100 K. Making use of the spotfinder class and the implemented electron energy remote control, I/E curves of high point density can be measured much faster than manually.

I/E curves automatically. The spotfinder is necessary, because during the recording the diffraction pattern can move with the changing energy in a similar way as during a real-time measurement. This phenomenon occurs, if the central diffraction spot cannot exactly be aimed at the channeltron due to limitations of the sample manipulator. A situation in which the specular beam is reflected on the channeltron without using the octopole is desired for this measurement as this at least assures that the angles of incidence and exit of the electron beam remain the same when the energy is varied. This geometry makes that I/E curves are highly reproducible. In fig. 2.4 an I/E curve of a clean Ge(100) surface is plotted that has been obtained in this way. Recording an I/E curve takes only 5-30 minutes, depending on the spike's intensity and the resolution of the curve. It should be remarked that I/E curves require the same demands from the spotfinder reliability as real-time intensity measurements relating to the intensity minima (see 2.2.3).

2.2.6 SPA-LEED measurements vs. sample temperature

Usually the diffraction pattern does slightly move when the sample temperature is changed due to the insufficient thermal stability of the sample holder. The spotfinder class compensates this motion by tracking the diffraction spots. With this requirement met, WinSPA32 can perform diffraction pattern intensity measurements against the sample temperature, provided that a sample temperature sensor is present or the relation between sample heating parameters and sample temperature is well defined. As an example, fig. 2.5 shows the intensities of the central, the first order, the half order and the c(4x2) reconstruction peak of a clean Ge(100) surface measured against the sample temperature. The c(4x2) reconstruction spot disappears at about 250K in agreement with the phase transition that is expected in this temperature regime.

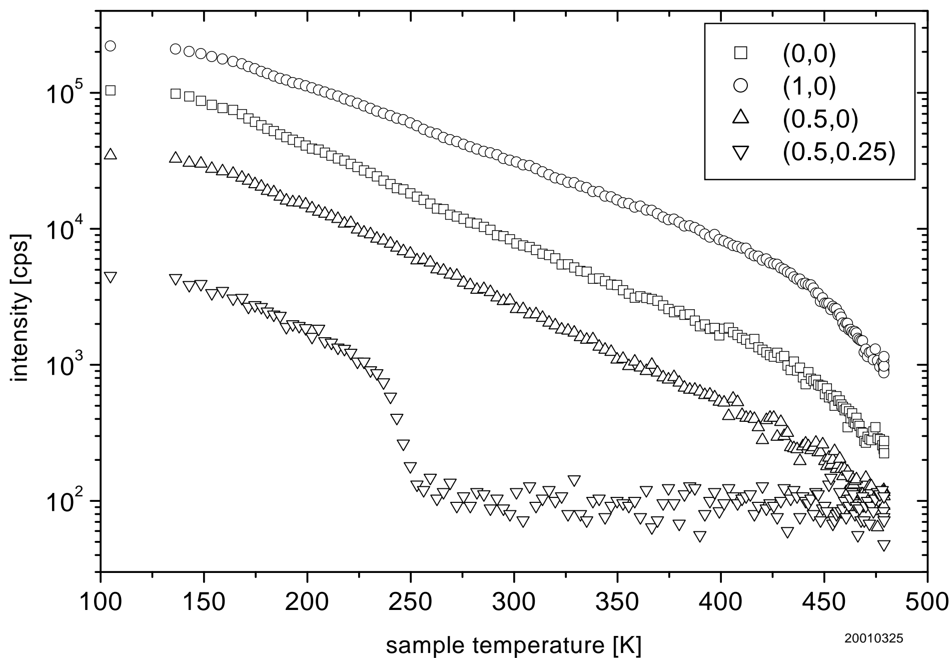

Figure 2.5: Automatically recorded intensity measurement of the central diffraction, first order, half order and c(4x2) spot of a clean Ge(100) surface vs. the sample temperature. Using multiple instances of the spotfinder class, all intensities were measured in one stage.

2.3 Extended one-dimensional intensity measurements

Spot profiles (also known as one-dimensional scans (1D-Scans) or linescans) are intensities of a diffraction pattern measured along a line in the k-space. As an extension of the zero-dimensional intensity measurements (e.g. measurement of the spike intensity of a diffraction spot) they contain lots of valuable information for surface analysis, especially when they are measured as a parameter series against e.g. the time in real-time during surface manipulation or against the scattering phase. Also the well-known 2D-Scan (the intensity map in the $k_{\|}$-plane) is a special case of a spot profile series. Additional to the 2D-Scans, WinSPA32 supports the automatic real-time recording of spot profile series against the time of an experiment and the recording of series against remote controllable parameters like the electron energy or the sample temperature. Similar to the spotfinder class, the user of WinSPA32 can create several instances of the class scanning the spot profile series. In this way multiple spot profile series can be recorded intermittently during the same experiment.

2.3.1 Real-time spot profile series

Spot profile series measured in real-time allow a deeper insight in the changes happening on a surface during an experiment [MSY+00, MzHGG+00]. There are many ways to graphically display such a spot profile series. Fig. 2.6 shows a colour coded representation (in particular useful to visualize phase changes on the surface) of a series recorded during homoepitaxy on Si(111) at out-of-phase conditions. The line along which the intensities are measured is defined by the central diffraction spot and one of the closest 7x7 reconstruction spots. As can easily be seen, the intensity of the central diffraction spot oscillates (compare with fig. 2.1), whereas the intensity of the reconstruction spots is decaying continuously. Using WinSPA32, one Spotfinder instance tracks the central diffraction spot and a second Spotfinder instance tracks one of the 7x7 reconstruction spots. The 1D-Scan is then measured on the line defined by the coordinates of the two Spotfinder instances. This procedure (in contrast to simply measure along a line defined by one spot and an certain fixed angle) has the advantage that the measurement cannot be falsified by slight rotations of the diffraction pattern that can occur during the growth experiment due to instabilities of the sample holder/manipulator, because the scanning parameters (origin and angle of the line) are continuously updated using the current spot coordinates from the spotfinder instances. From the moment on that the intensity of the reconstruction spot has completely vanished, the updating of line angle of course ends. Then, only the origin of the line is updated.

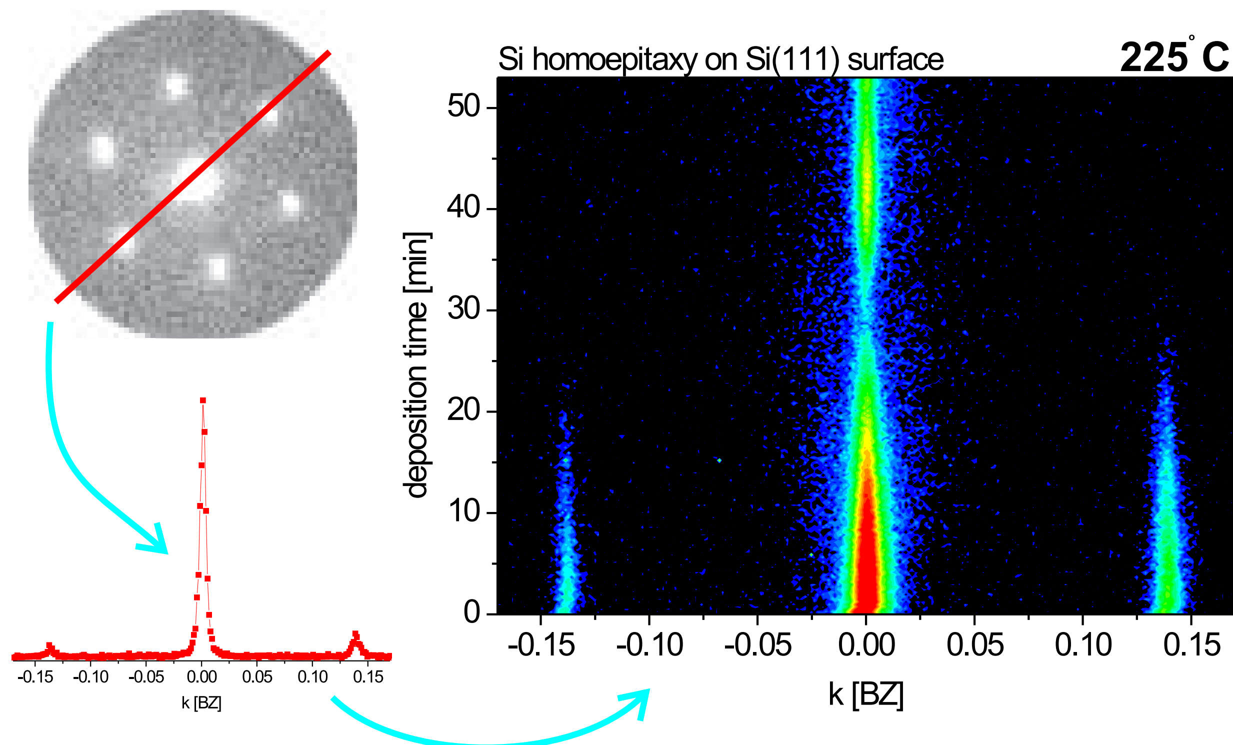

Figure 2.6: Color coded representation of an extended one-dimensional real-time measurement: During homoepitaxy on Si(111) 1D-Scans through the central spot and two 7x7 reconstruction spots are continuously recorded. Origin and angle of the line along which the intensities are measured are defined by the coordinates of two spotfinder instances that follow central spot and reconstruction spot throughout the measurement. These parameters are continuously updated to avoid falsification of the measurement by drifting spots. While the intensity of the central spot is oscillating, the reconstruction spots are decaying continuously.

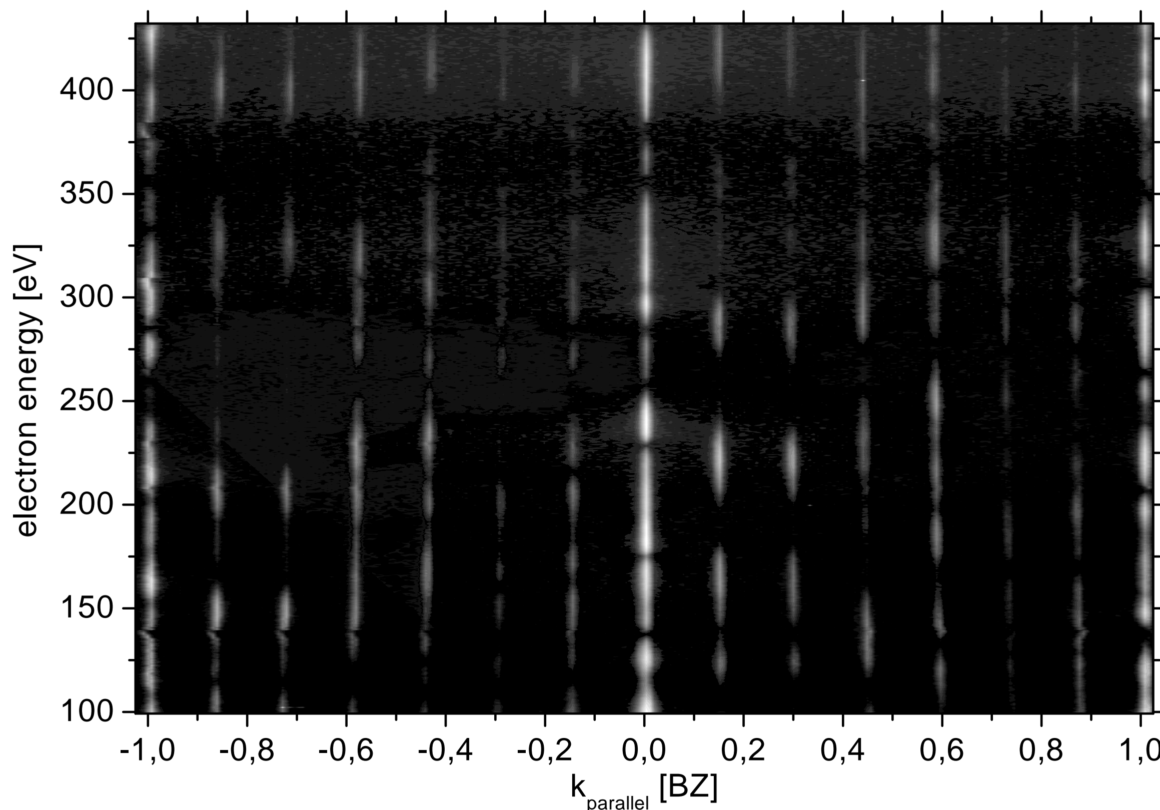

Figure 2.7: Colour coded representation of an extended one-dimensional measurement: 2 BZ wide 1D-Scans through the central and the first order spots were recorded on a clean Si(111) surface at room temperature against the electron energy .

2.3.2 Spot profile series vs. electron energy

Similar to the real-time measurement just described, where the spot profiles are recorded against the time of an experiment, 1D-Scans can also be recorded against the electron energy/the scattering phase [BAN96]. In the case of fig. 2.7 a series of wide 1D-Scans through the central and first order diffraction spots of a clean Si(111) surface at room temperature have been plotted colour coded against the electron energy. Note the 12 rods originating from the 7x7 reconstruction between the central and first order diffraction spots' rods. The graph nicely visualizes the difference in phase conditions of the 15 spots.

Extended intensity measurements can also be used to easily determine the angle of facet structures on surfaces [KJW$^+$00, MZVHvH98, MSY$^+$00]. Fig. 2.8 shows weak facet rods of $\approx 55^\circ$ facets on Ge(100) after Si heteroepitaxy (see fig. 5.1 for details of this experiment).

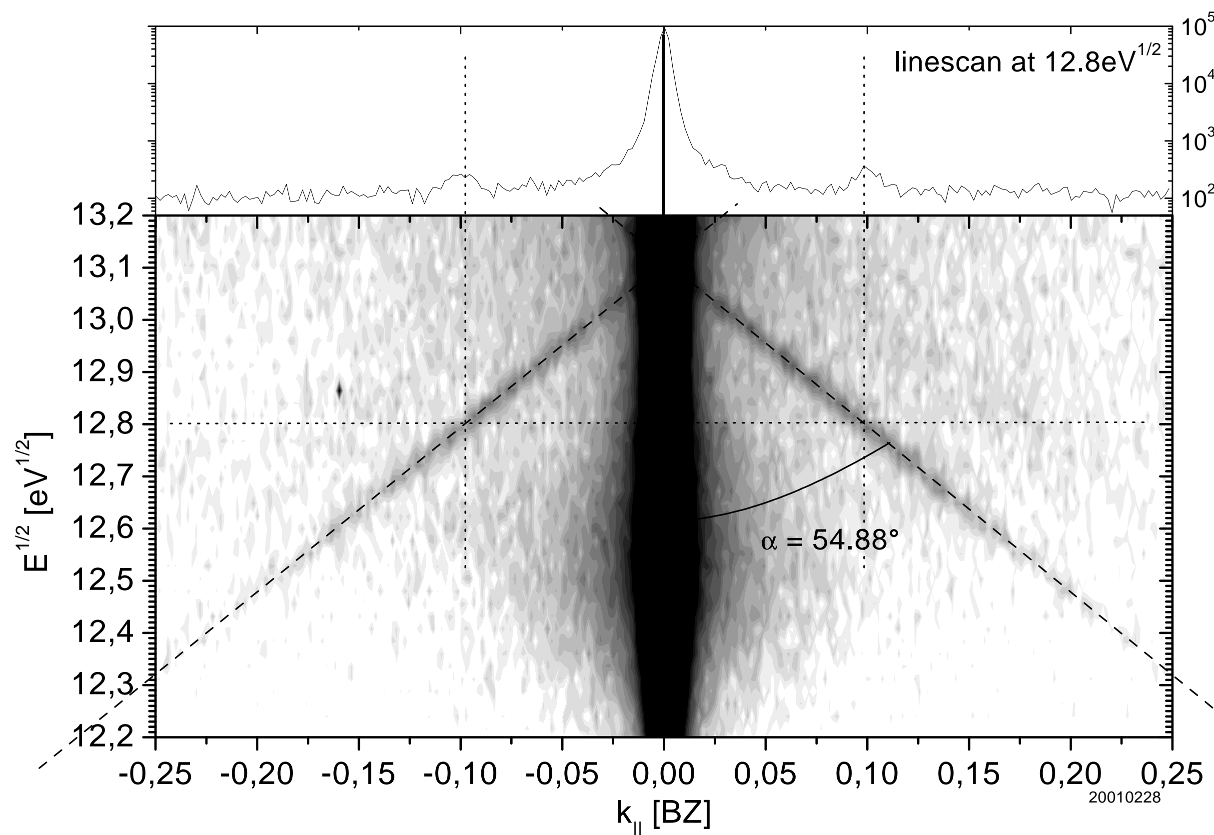

Figure 2.8: Colour coded representation of an extended one-dimensional measurement: 0.5 BZ wide 1D-Scans through the central spot of a Ge(100) surface were recorded at 100K after Si heteroepitaxy (see fig. 5.1 for details of this experiment). The two oblique rods are caused by facets of $\approx 55°$ on the surface. The linescan (upper panel) demonstrates that the facet spot intensity is weak compared with the central spot intensity.

2.4 Automatic experiments

Key experimental parameters like sample temperature (direct and indirect heating), evaporation rate and UHV system pressure can be measured and set directly. This allows not only new types of (automatic, if necessary) SPA-LEED measurements as described in the previous sections. It also facilitates everyday experimental tasks that can be very time consuming and monotonous (e.g. the automatic degassing and preparation of samples that have just been inserted to the vacuum system, see chapter 1.4). Combining sample preparation and automatic diffraction pattern intensity measurements, series of growth experiments can then be performed completely automatically using a simple macro instruction method (provided that the surface preparation of the sample can be completely done by heat-treatment, as it is the case for Si(111) after homoepitaxy). Fig. 2.9 shows a series of spot intensity measurements during homoepitaxial growth on Si(111) at six different temperatures that has been performed by WinSPA32 during one afternoon.

2.5 Distortion correction

Especially at low electron energies, wide two-dimensional intensity scans of diffraction patterns are clearly influenced by lens aberrations of the SPA-LEED optics. Apart from slight trapezoid and parallelogram distortions, a barrel distortion causes the strongest deviation of the diffraction spots from their expected positions. Fig. 2.10 shows a diffraction pattern of a clean Ge(100) surface at 100 K and a quite low electron energy of 59.6 eV.

2.5.1 Calculating the undistorted spot positions

The measured positions of the first order spots are marked with white crosshairs. The dashed lines indicate the calculated positions where the spots are expected without distortion. As can easily be seen, the distortion pulls parts of the diffraction pattern towards its centre. The shifts in position Δx and Δy caused by the barrel distortion at the point (x, y) can in the most simple case be expressed in the following way [Bro65, KF86]:

$$\begin{aligned} \Delta x &= \beta_x (x^3 + x \cdot y^2) \\ \Delta y &= \beta_y (y^3 + y \cdot x^2) \end{aligned}$$

In order to calculate spot positions of a distorted scan back to their undistorted positions, the coefficients β_x and β_y have to be determined first.

WinSPA32 uses an enhanced model for the calculation of the barrel distortion properties. In this way also possible translations and tilts of the diffraction pattern are considered.

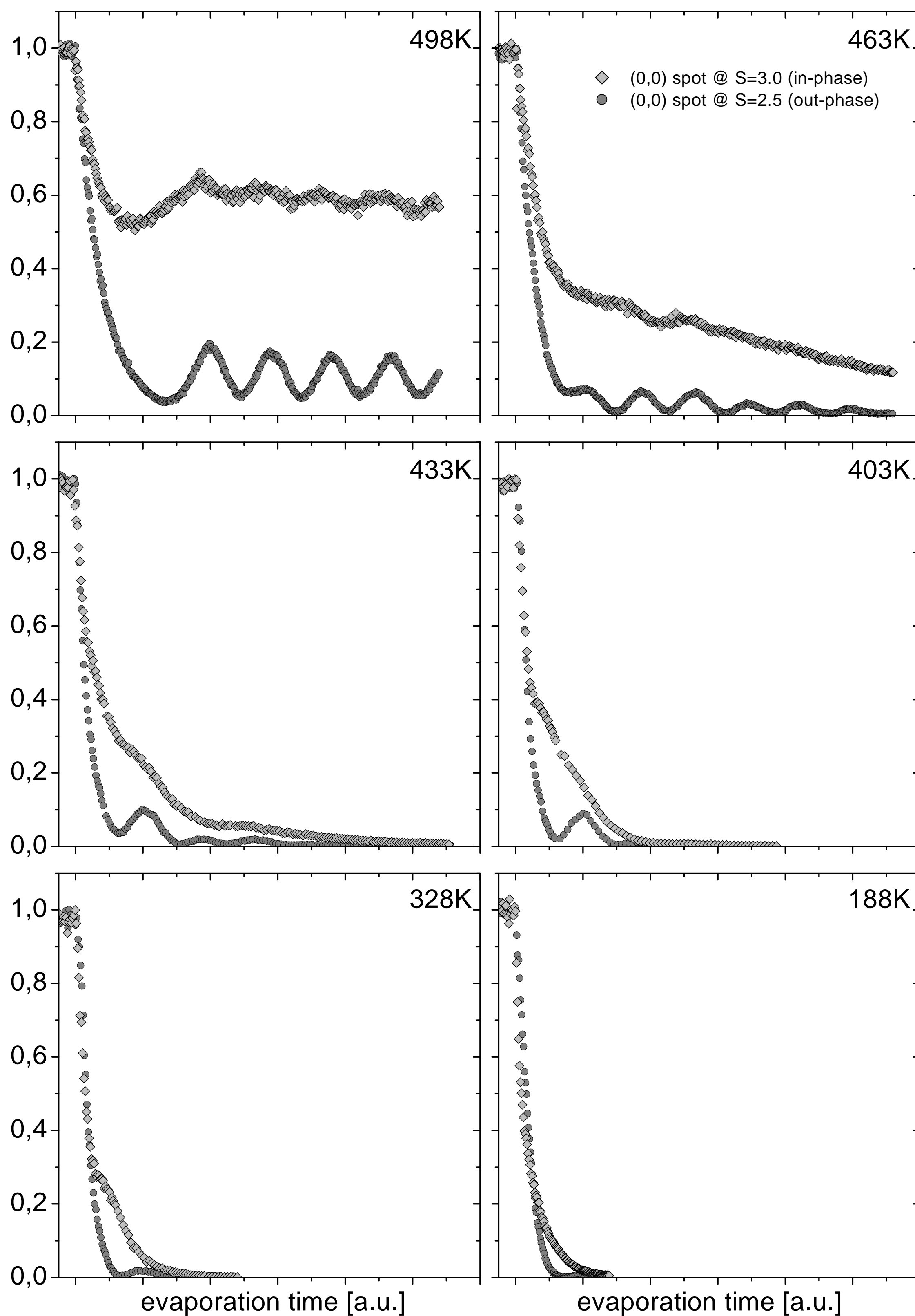

Figure 2.9: Diffraction spot intensity measurements during homoepitaxy on Si(111) at different temperatures. The experiments were automatically performed

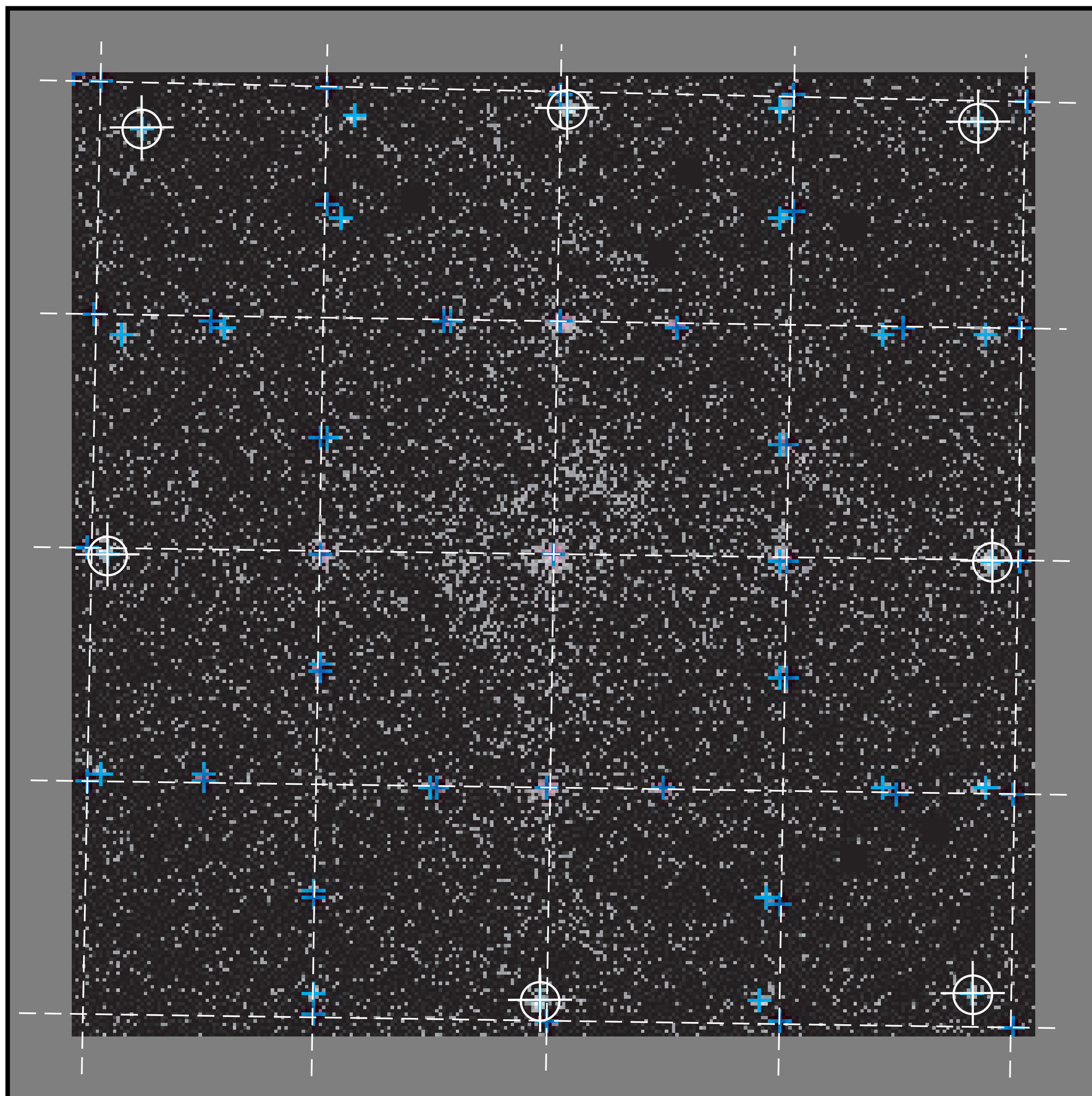

Figure 2.10: Barrel distortion: Wide 2D-Scan (width > 2 BZ) of a clean Ge(100) surface at 100 K and a quite low electron energy of 59.6eV (the lower the electron energy the stronger the distortion). The white crosshairs mark the first order diffraction spots as they were measured. The intersections of the dashed white lines indicate the calculated positions where the spots are expected without distortion.

Instead of β_x and β_y six fit parameters $c_1, \ldots, c_6$ (see table 2.1) have to be considered. The spots' coordinates in units of deflection voltage x_i, y_i (measured) and the true coordinates in units of BZ $k_{x,i}$, $k_{y,i}$ of all known visible spots of a 2D-Scan are used to calculate the parameters by fitting them to the following extension of the barrel distortion equations:

$$\begin{aligned}
\tilde{k}_{x,i} &\equiv k_{x,i} \cdot \cos c_6 - k_{y,i} \cdot \sin c_6 \\
\tilde{k}_{y,i} &\equiv k_{x,i} \cdot \sin c_6 + k_{y,i} \cdot \cos c_6 \\
x_i &\equiv c_1 \left((\tilde{k}_{x,i} - c_3)^3 + (\tilde{k}_{x,i} - c_3)(\tilde{k}_{y,i} - c_4)^2 \right) \cdot (c_5)^3 + \tilde{k}_{x,i} \cdot c_5 \\
y_i &\equiv c_2 \left((\tilde{k}_{y,i} - c_4)^3 + (\tilde{k}_{y,i} - c_4)(\tilde{k}_{x,i} - c_3)^2 \right) \cdot (c_5)^3 + \tilde{k}_{y,i} \cdot c_5
\end{aligned}$$

For the determination of the fit parameters the non-linear least squares *Levenberg-Marquardt*

c_1	distortion factor x-direction
c_2	distortion factor y-direction
c_3	center of diffraction pattern: x-coordinate
c_4	center of diffraction pattern: y-coordinate
c_5	sensitivity
c_6	rotation angle of the diffraction pattern

Table 2.1: Definition of the fit parameters $c_1 - c_6$ for the barrel distortion correction.

Method is used [PFTV86]. At least 6 diffraction spots are of course necessary for the calculation. Nine spots (e.g. the first order spots and the central spot) give significant results. Diffraction patterns of semiconductor surfaces with its reconstruction spots lead in contrast to unreconstructed metal surfaces to even smaller errors of the fit parameters. In case of the distortion correction shown in fig. 2.10 the coordinates of 36 spots (central spot, first order spots, half order spots and the spots of the c(4x2) reconstruction) have been used.

2.5.2 Energy dependence of the fit parameters

A series of 2D-Scans like the one shown in fig. 2.10 was taken at different electron energies in the range from $\approx 7\sqrt{\text{eV}}$ to $\approx 29\sqrt{\text{eV}}$. From all those scans the barrel distortion fit parameters have been determined and drawn against the electron energy (see figs. 2.11-2.14).

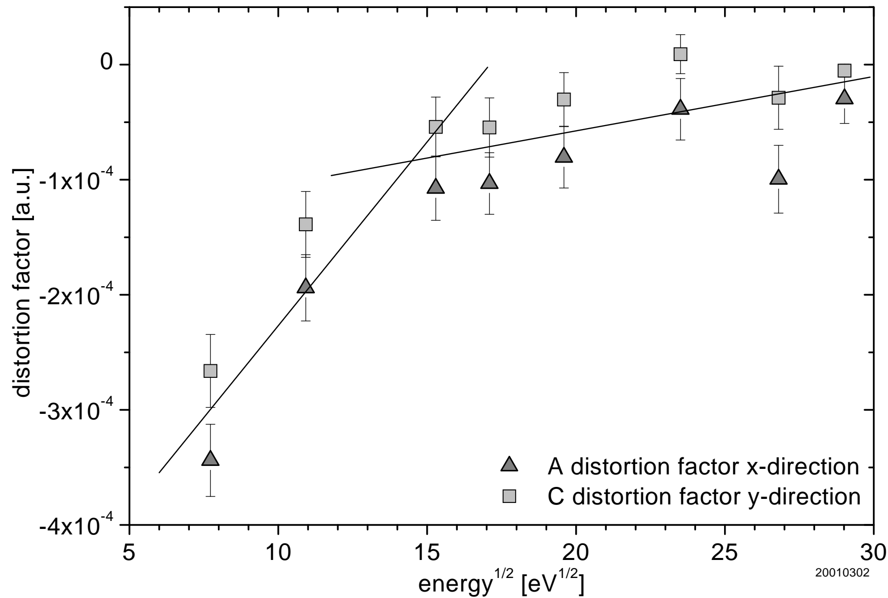

Figure 2.11: Barrel distortion factors in x- and y-direction plotted against the electron energy. The lines are guides to the eye. The lower the electron energy, the stronger the barrel distortion. From about $15\sqrt{\text{eV}}$ downwards, the increase is distinctly enhanced.

As can be seen from fig. 2.11, the barrel distortion is the stronger, the smaller the electron energy is. At high electron energies it is more difficult to find certain electron energies where many diffraction spots are visible. This is the reason for the non-uniform barrel distortion factors around $27\sqrt{\text{eV}}$

The diffraction pattern centre moves only very little with the electron energy (see fig. 2.12). Most probably the odd value at $29\sqrt{\text{eV}}$ has to be attributed to the fact that the calculation in this particular case only bases on 14 spots because of the high electron energy.

The SPA-LEED sensitivity is quite constant in the energy range from $10\sqrt{\text{eV}}$ to $23\sqrt{\text{eV}}$ (see fig. 2.13). At energies below $10\sqrt{\text{eV}}$ and above $23\sqrt{\text{eV}}$ the sensitivity varies significantly. The total measured change in sensitivity is about 2%.

The tilt of the 2D-Scans stays almost constant in the whole electron energy range (see fig. 2.14).

In conclusion, the presence of the barrel distortion means problems for the interpretation of all non-corrected wide diffraction pattern intensity scans (1D-Scans *and* 2D-Scans). In the close vicinity of the central spots the use of non-corrected scans is not tainted with a significant error, but for scans with a width of 1/2 BZ or more that can be the case,

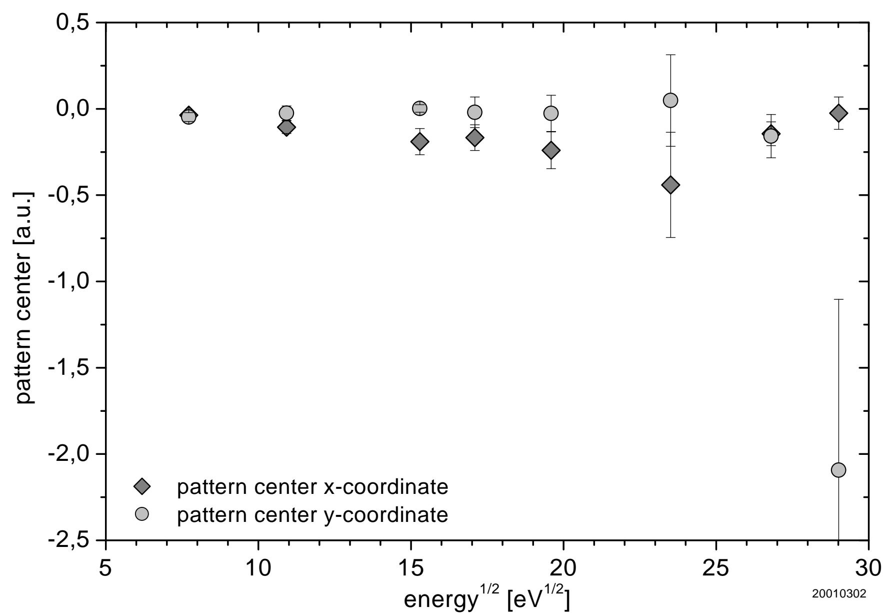

Figure 2.12: Diffraction pattern centre x- and y-coordinates plotted against the electron energy. The position of the centre only changes very little with the electron energy.

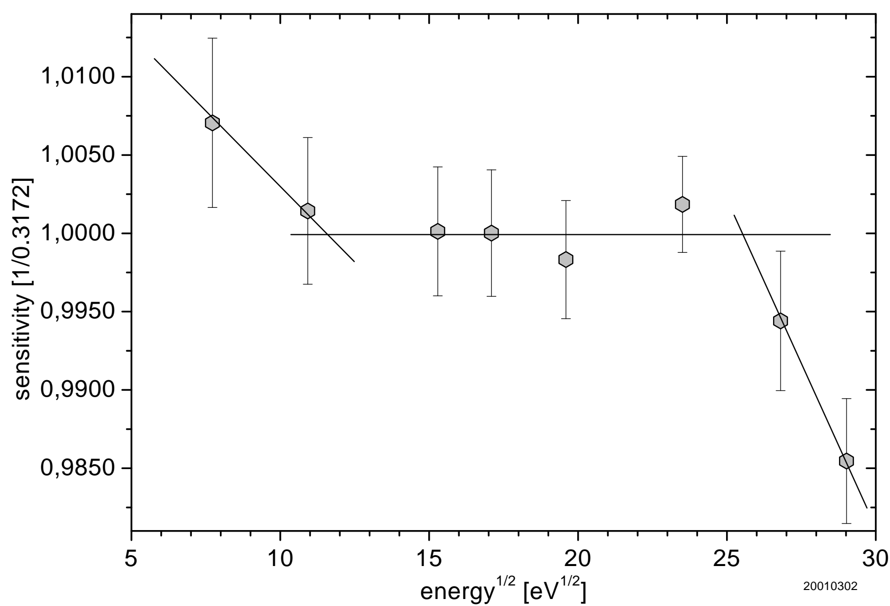

Figure 2.13: Normalized SPA-LEED sensitivity plotted against the electron energy. The lines are guides to the eye. The sensitivity is relatively constant from $10\sqrt{\mathrm{eV}}$ to $23\sqrt{\mathrm{eV}}$. Below $10\sqrt{\mathrm{eV}}$ and above $23\sqrt{\mathrm{eV}}$ it varies significantly.

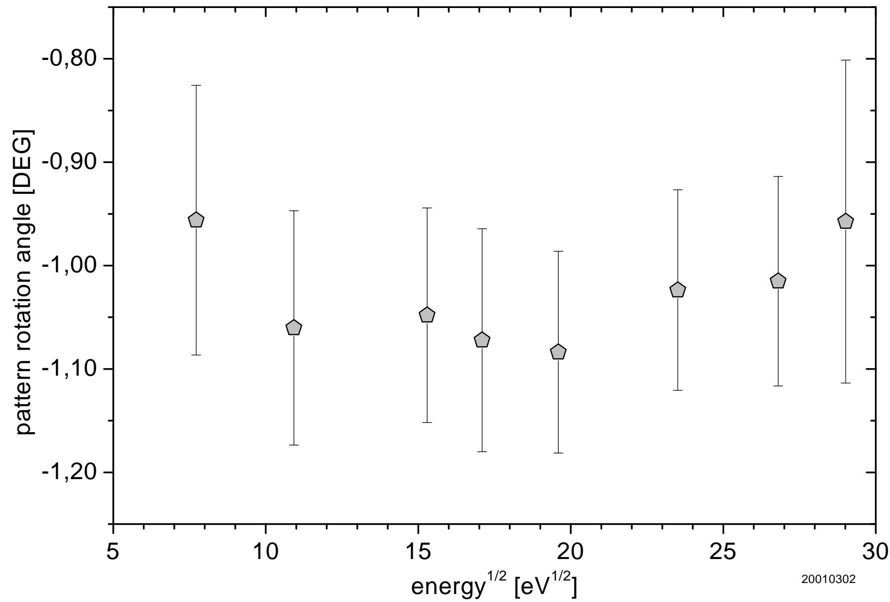

Figure 2.14: Diffraction pattern rotation angle plotted against the electron energy. It stays almost constant in the whole electron energy range.

especially for low electron energies. While the examination of the surface morphology is essentially undisturbed, conclusions for e.g. reconstructions could be hampered. This analysis also shows that a simple determination of the sensitivity factor is best done by measuring the distance between central and the (0,1) spot. Determining the sensitivity from the (-1,1) and (1,-1) spots gives easily an error of 5% in k-value. A second problematic situation occurs in 1D-scans through for instance the (0,0) and (1,0) spots: This scan will only graze the(-1,0) spot if lucky or completely miss that spot that actually should be on one line. In essence, a real-time barrel distortion correction is recommendable for the future.

2.6 Conclusion

The new SPA-LEED data acquisition software WinSPA32 in combination with the implementation of the remote control of the electron energy and other key experimental parameters allows the reliable automatic measurement of diffraction pattern intensities in real-time while the experiments are being performed. During an experiment, the spike intensities or linescans through various spots even at different phase conditions can be recorded intermittently. I/E curves can be recorded automatically with high point resolution. The

user-interface of the software allows a good overall view of the state of the experiment and enables user interaction at any moment. This leads to less failure measurements as they were often experienced with the standard software.

The results of the electron energy dependence study of the SPA-LEEDs barrel distortion recommend an automatic real-time barrel distortion correction as a future promising development.

Chapter 3

Homoepitaxy on Si(111)

3.1 Introduction

Probes like high-resolution helium atom diffraction (TEAS) [EFFL94] [Ern97] [GBIS85] [DFC+88] [PVC84] [WBR+98] [vDJP99], X-ray diffraction [vSvdVFN92] [vSLZ+92] [Rob98] [RPLV98] [vdVVBV98] [VLvdV95] and high-resolution low energy electron diffraction (HR-LEED, or SPA-LEED[1]) [NKE93] [EJ89] [HvH99] [ZWDC94] [ZW97] provide valuable, laboratory scale information on the morphology and atomic structure of surfaces and (ultra-) thin films. Especially when used as real-time probes[2] for film growth or other dynamic processes on surfaces, such as two-dimensional phase transitions and others, they are well suited for monitoring the changes of structure and/or morphology of surfaces. Among the probes mentioned SPA-LEED is the widest spread and most readily accessible technique. In order to take full advantage of its capabilities as a real-time monitor for growth or etching experiments, it is highly beneficial to be able to measure the temporal evolution of several integer or non-integer diffraction spots (quasi) simultaneously.

Since the existing SPA-LEED data-acquisition software is rather more focused on a static analysis in retrospect than on a real-time, in-situ evaluation of dynamic processes at surfaces, we have developed a new software concept. It allows tracking the temporal changes of multiple diffraction spots and their shapes simultaneously, even when they temporarily pass through a low intensity minimum. It is also capable of dealing with spot drifts, occurring as a result of insufficient stability of the sample holder, e.g., during heating. The potentialities of our novel approach are demonstrated with experimental results on the homoepitaxial growth of Si(111). The simultaneous measurement of diffraction spots at different Bragg conditions sheds new light on the applicability of the kinematic approx-

[1]Spot Profile Analysis Low Energy Electron Diffraction

[2]in-situ probes of surface morphology during sample manipulation

imation in SPA-LEED and highlights possible pitfalls in SPA-LEED data-analysis. Our data clearly indicate that the maximum surface smoothness in layer-by-layer growth does not necessarily coincide with the deposition of an equivalent integer number of bilayers. More details on our data-analysis and some key features of the software are described.

3.2 Experimental

All experiments described in this paper were performed in a UHV system with a base pressure of $p < 3 \cdot 10^{-11}$ Torr. The silicon samples (n-doped, $\rho \approx 2500\,\Omega$cm) were prepared using flash annealing at 1500 K. Silicon is evaporated from a rod heated by direct current. The resulting growth rate is in the range of one silicon bilayer per ten minutes. During the flash annealing process of the silicon samples and during growth the system pressure is always better than $p < 1 \cdot 10^{-10}$ Torr. The filaments of all UHV system devices are switched off during sample preparation and growth to keep partial pressures of carbon oxides as low as possible. Doing real-time growth monitoring, the SPA-LEED electron gun's filament current is 0.9 A, yielding an emission current of 5 μA. Sample temperatures till about 900 K are determined indirectly using calibration measurements performed with Pt100 resistors on dummy samples. To avoid contamination, the silicon samples are at no time of the atmospheric and vacuum preparation and the experimental processes in direct contact with other materials than molybdenum, tantalum and specialized semiconductor manipulation tools.

3.3 Multiple diffraction spot tracking

Our new software enables tracking several diffraction spots and measuring their intensities and/or profile in real-time during growth or etching experiments. Owing to the full implementation of the remote control of the electron beam energy, the spots can also be tracked at different Bragg conditions (quasi-) simultaneously. For the present purpose we apply this technique to monitor the homoepitaxial growth of Si(111). Fig. 3.1 shows measured diffraction spot intensities during silicon growth at different sample temperatures in the range between 188 K and 498 K. Limitations of the sample heating prevented in-situ SPA-LEED measurements at even higher temperatures. During growth, the intensities of the central diffraction spot at S_z=2.5 (out-of-phase; $\phi = 5\pi$) and S_z=3.0 (in-phase; $\phi = 6\pi$) were recorded.

Let us first concentrate on the data illustrated in the upper left panel. At 498 K, the out-of-phase intensity is oscillating with the evaporation time, indicating layer-by-layer growth [ABHM88]. The maxima of the growth oscillations are at almost constant height,

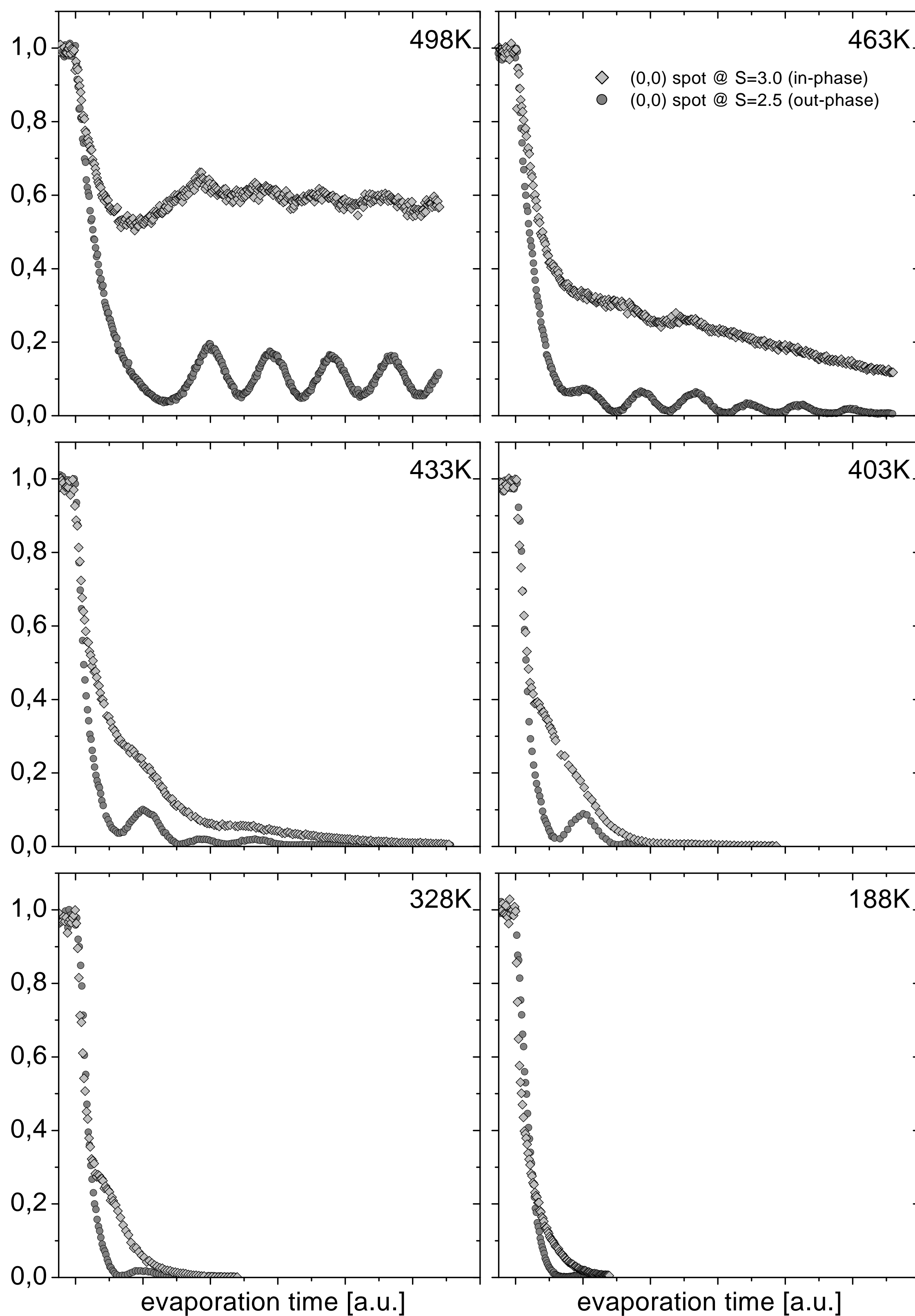

Figure 3.1: Intensities of the central diffraction spot at in- and out-phase conditions during homoepitaxy on Si(111) at different temperatures

at the level of about 0.2 times the spot intensity before evaporation. This observation is indicative of persistent effective layer-by-layer growth. The inherent kinetic roughness, which builds up initially, remains "stationary" during later stages of growth and only varies with the periodicity set by the equivalent deposition of one bilayer of material [ABHM88] [Hen88] [PC]. Within the kinematic approximation and assuming a hypothetical ideal instrument (infinite transfer width) the intensity of the anti-phase Bragg spot would vary as

$$I_{out-of-phase} \propto \left[\sum_{i=1}^{\infty} (x_{2i} - x_{2i-1}) \cdot \sum_{k=0}^{\infty} (-1)^k \, \alpha_k \right]^2 \tag{3.1}$$

where x_i indicates the exposed fraction of bilayer i. The contributions of deeper ('hidden') bilayers are represented by α_k with $\alpha_k < \alpha_0$. Usually the index k runs only over a few bilayers, due to the electrons' small mean elastic free path length, i.e. α_k decays strongly with k. In the case of growth oscillations the out-of-phase spot intensity runs through a minimum, when the condition

$$\sum_{i=1}^{\infty} x_{2i} = \sum_{i=1}^{\infty} x_{2i-1} \tag{3.2}$$

is fulfilled. By definition this minimum equals zero. In the actual experiments, however, even within the kinematical approach, the minimum intensity differs from zero because of the fact, that the intensity as described above has to be convoluted with the instrument response function. This gives rise to non-zero values when taking the intensity at the Bragg position. For the maxima one has to comply with the condition

$$\left| \sum_{i=1}^{\infty} (x_{2i} - x_{2i-1}) \right| = max \tag{3.3}$$

In the hypothetical ideal layer-by-layer growth case this would apply for $x_i = 1$ and $x_{k \neq i} = 0$. In realistic cases, however, (at least) three bilayers are exposed around a maximum and the resulting intensity at the Bragg position in the kinematic approximation would typically yield

$$I_{i,out-of-phase} \propto \left[(x_i - x_{i-1} - x_{i+1}) \cdot \sum_{k=0}^{\infty} (-1)^k \, \alpha_k \right]^2 \tag{3.4}$$

being less affected by convolution with the instrument response function. The stationary values of the experimental maxima of the upper left panel in Fig. 3.1 therefore indicate that around the intensity maxima the distribution of exposed bilayers remains the same, independent of the film thickness. Under in-phase conditions the kinematic approximation predicts a stationary intensity at the Bragg position with a value equal to

$$I_{in-phase} \propto \left[\sum_{k=0}^{\infty} \alpha_k \right]^2 \tag{3.5}$$

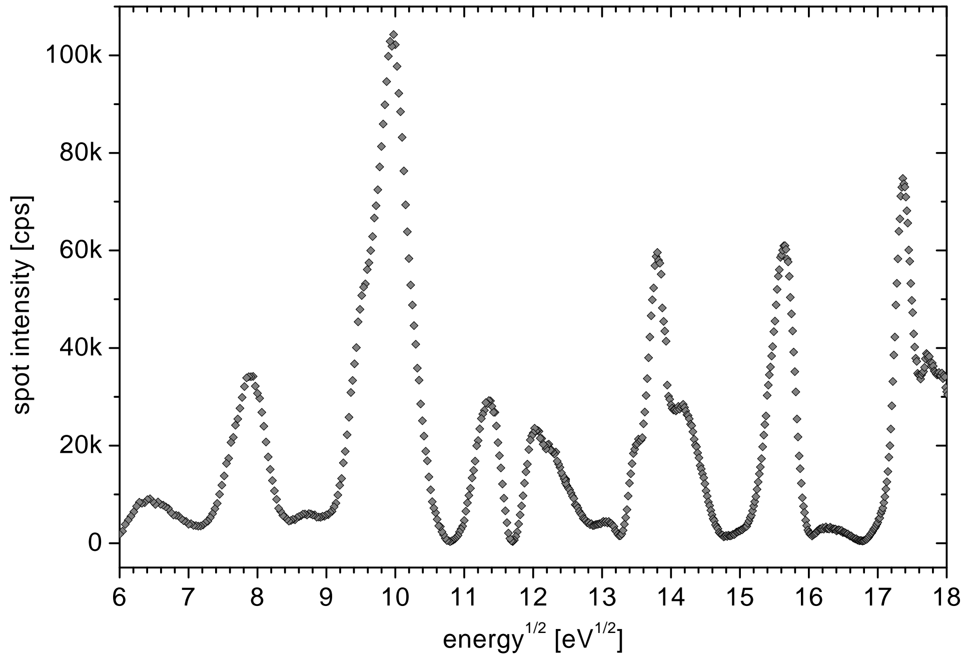

Figure 3.2: Energy dependence of the Si(111) central diffraction spot's intensity

being independent of exposed bilayer distribution. In fact this is clearly at variance with the experiment (cf. Fig. 3.1; upper left panel), which exhibits a distinct dependence of the in-phase intensity on the deposited amount and thus on the proceeding development of the exposed bilayer distribution.

A first attempt to rationalize the remarkable deviation of the actually measured data from the prediction in (3.5) can be found in the shortcomings of the simple kinematic approximation which has been described above. It is a well-known fact that a full dynamic evaluation of I-V data has to be performed. Fig. 3.1 shows that the intensity of the in-phase peak clearly decreases with deposited amount of silicon, being clearly at variance with condition (3.5). This fact demonstrates that diffuse scattering from step sites takes place. The loss of intensity far above amount that can be accounted for by a simple one-to-one correlation to the density of the step atoms demonstrates the need for taking into account variations of the atomic scattering factors beyond that of the step atoms only. Though less severe, this feature is similar to that observed in thermal energy helium scattering.

Further evidence for an insufficiency of the simple kinematic approach is provided by Fig. 3.2, showing an energy-scan for the specular spot. These data unambiguously show the dynamic character of electron diffraction and thus nicely demonstrate the need for taking into account multiple reflections. In a seminal paper [ABHM88] Henzler and co-workers

argue that the dynamic effects may be accounted for satisfactorily by including them in the scattering factor. So for each surface cell a column can be introduced, which takes care of all multiple scattering with crystal atoms in a defined neighbourhood. Obviously, such an "atomic" scattering factor would depend strongly on the energy of the diffracted electrons and on the order of the diffraction spot. However, such effects are supposedly negligibly small and allow application of the kinematic approximation with identical scattering factors provided sufficiently small variations of the in-plane wave vector change are considered [ABHM88] [Hen85] [HvH99]. This approach is supposedly well within the validity limits when examining spot profiles. To be fair Henzler did realize that in principle the scattering factors, constructed to mimic multiple scattering, for e.g. columns in the centre of terraces may be different from those centred at step sites. In practice he notes, however, that: "so far no experimental results are reported, which require dynamic calculations with respect to disorder".

Henzler and co-workers have reported cases too, where the intensity of in-phase spot suffers a substantial reduction with increasing roughness. In these cases, however, this feature remains either disregarded or is attributed to diffuse scattering from point defects. We think our data (Fig. 3.1; upper left panel) suggest the need to take into account dynamic aspects when analysing (growth induced) disorder. This statement is based on a number of observations; all, as we will elaborate below, highly significant. (Please note that the capability of measuring multiple spots simultaneously, enabled by the new software, is crucial to the second and, in particular, the third issue addressed below.)

- First we note that the decay of the in-phase spot height amounts to roughly 50% already in the high temperature data. This makes any explanation in terms of diffuse scattering from point defects highly questionable, since this would require densities of such defects of the order of 30% and even higher at slightly lower temperatures (cf. Fig. 3.1). Such an assignment does not really seem physically acceptable and would not allow out-of-phase oscillations with the strength shown in the upper left panel.

- Second, we stress that not only the out-of-phase but also the in-phase spot height exhibits oscillations with a periodicity that varies at the rate of bilayer deposition. They are admittedly weak, but still are clearly visible. These oscillations are very reminiscent to those observed under in-phase conditions before in TEAS experiments [PBR$^+$92]. In this case they have been attributed to diffuse scattering from step edges. As is well-known helium scattering is very sensitive to defects and the oscillations directly reflect the fact that the integral step length oscillates in tact with the deposition of a bilayer, being at its maximum around the deposition of a bilayer

(or 2n+1 BL). In this case for Si/Si(111) the amplitude of the oscillations is much smaller because of the lower sensitivity of LEED for diffuse scattering from steps.

- Finally, we emphasize that the maximum in the in-phase data appears roughly at an equivalent coverage of some 0.15 bilayers before that of the out-of-phase data. This again is at variance with an explanation in terms of scattering from single point defects: point defects, if present in any appreciable amount at all on Si(111) at the given temperature, should be supposed to be present less abundantly near completion of the growth of a particular bilayer and at the concomitant nucleation in the next level.

Rather than scattering from single point defects the explanation of the in-phase spot should be sought in diffuse scattering due to different atomic scattering factors and possibly -phases related to unit cells at (or near to) the step edges. In terms of Henzler's column-concept the scattering factor related to the columns positioned at (or near) a step edge substantially differ from those at a central position on a terrace. One may argue that a step atom position with a non-negligible normal component of relaxation, different from those of terrace atoms, would lead to a similar result. Closer inspection of that possibility, however, reveals that contraction of the step atoms would to second order approximation result in adatom islands of which the effective height is determined by the average height of all atoms. In other words the effective layer distance would be slightly smaller than its bulk value and the in-phase condition would be slightly changed. Since the average length scale to a very good approximation can be considered about constant during layer-by-layer growth this possibility is highly unlikely. Moreover, the in-phase condition has been detected for the rough surface! (Deviations of the step atom position from the bulk positions in a lateral sense do not play a role since we are considering the intensity fluctuations of the (0,0)-beam.) Both cases mentioned further above could in principle be distinguished by comparing results of higher order diffraction spots. We did not address this issue, which we expect to be quite tedious and which would not affect the basic message, i.e., the attribution of the deficit of the in-phase spot height to a breakdown, or rather incompleteness, of the kinematic approximation with position independent effective atomic scattering factors. An atomic scattering factor for step atoms (and even near-step atoms), differing from terrace atoms would also allow understanding the appearance of the maximum of the in-phase spot heights at slightly smaller coverage than those of the out-of-phase maxima. This would be the case if at similar coverage the step edges around the vacancy islands in the almost completed bilayer are shorter than those at the circumference of the smaller adatom islands in the newly growing bilayer.

So far it is clear that dynamic features could be responsible for the observed anomalous

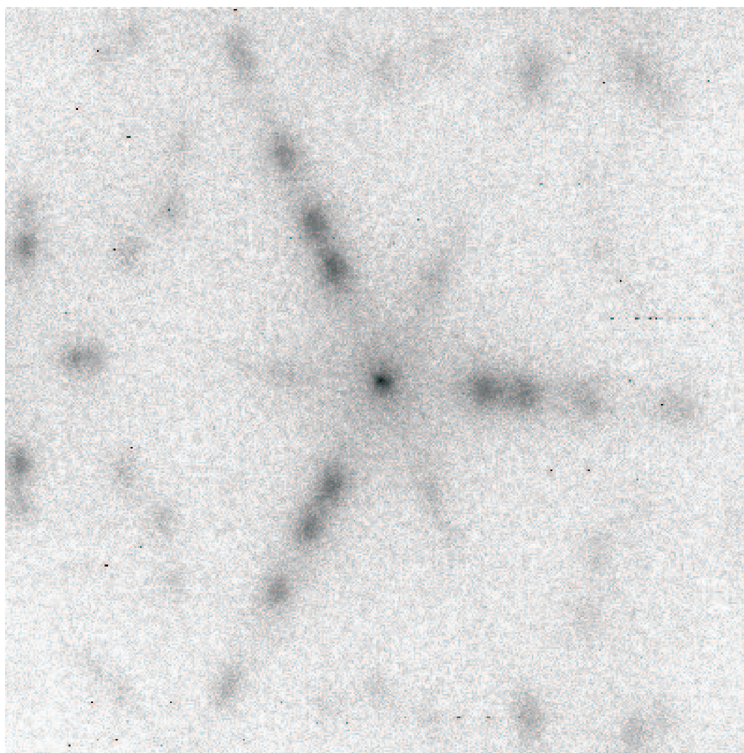

Figure 3.3: diffraction pattern of a quenched Si(111) surface after growth of 4 bilayers of silicon at 600K, E=221eV

behaviour of the intensity oscillations for both in-phase and out-of-phase peaks. Note that we have not observed physical variations in the shape and the width of the central spike of the specular beam. Consequently, whenever intensity is mentioned we mean integrated intensity or interchangeably height of the central spike.

It is highly likely that dynamic effects provide the physical background for our observations. However, in order to make this statement unequivocally we have to exclude a few other possibilities. It should be realised that the Si(111) surface is a very complex reconstructed surface. It initially has a (7x7) lateral periodicity, involving adatoms, vacancies, etc. When adatoms are deposited on this surface major rearrangements may occur. Even locally ordered atomic "7x7-building blocks" arrangements such as 3x3 or 5x5 may occur and have been reported [KDH89]. Being well aware of these possibilities we have looked for modified reconstructions and have found evidence for those as shown in Fig. 3.3 and 3.4. Indeed they are present but only at quite a bit higher temperatures. In the temperature range reported here we have carefully looked at the occurrence of fractional order peaks without any glimpse of success, however. We have not seen these even after

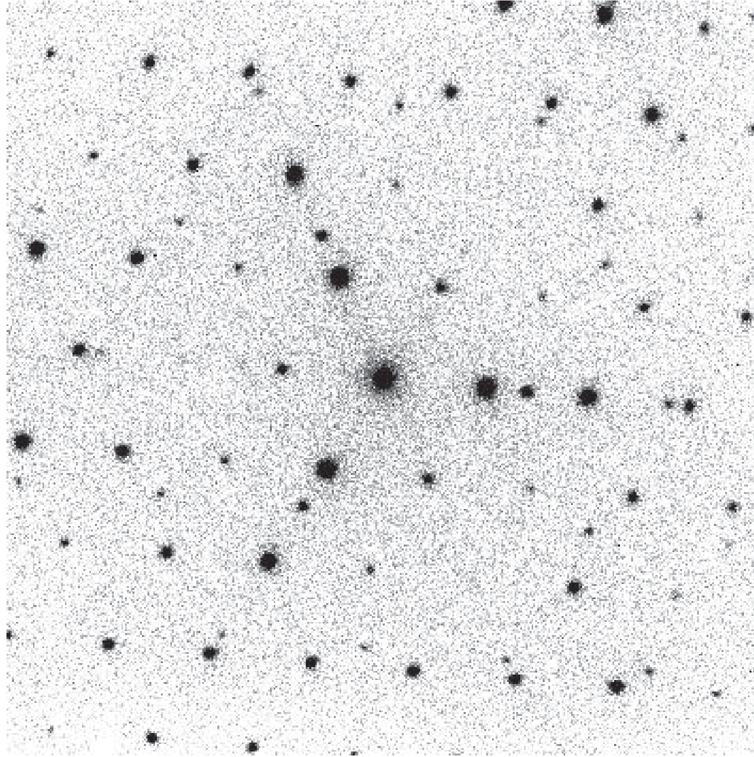

Figure 3.4: diffraction pattern of a quenched Si(111) surface after growth of 4 bilayers of silicon at 730K, E=221eV

quenching the substrate to well below room temperature. So we have only evidence for the presence of a 1x1 structure under the (temperature) conditions discussed here and have not observed oscillatory behaviour of any superstructure, in spite of heavily searching for them. Therefore, we conclude that the potential possibility of a, with layer deposition, oscillatory varying average terrace structure, which might give rise to the observed data, can be ruled out. We do think, however, that the disappearance of superstructures plays an important role in the very initial behaviour of the peak intensity (cf. Fig. 3.1).

We finally would like to draw the reader's attention to another example of the new level of consideration using our new experimental approach. For this we refer to the data obtained at the lowest temperature in (the right bottom panel of) Fig. 3.1. Again owing to the fact that beyond any doubt we know that the coverage is exactly the same at a given point in time we can be sure that the relative intensity of the in-phase spot height initially drops below to that for the out-of-phase spot height. This behaviour might be explained if one considers a non-zero pre-deposition step density. In that case destructive interference features already reduce the starting height of the out-of-phase spot, where only diffuse

scattering reduces the in-phase spot. It is noted that at the given temperature things get complicated soon because of the fact that an amorphous layer is growing. The reason for the second curve crossing remains unclear and is further disregarded here.

We return now to our main issue, i.e. the break-down of the simple kinematic approximation model in LEED from disordered systems. This fact bears strong implications with respect to possibilities of obtaining quantitative information from the energy dependence of the height of the central spike of the specular beam with respect to the vertical distribution of exposed bilayers [ABHM88]. When the simple kinematic approximation applies, this method is quite powerful to reveal such distributions. Here again a warning has to be given. In contrast to previously made presumptions with respect to the applicability of the kinematic approximation, dynamic scattering features may well be important for disordered systems. Therefore, when following the route for obtaining information on the vertical distribution of visible bilayers via the behaviour of the central spike with varying vertical phase conditions extreme caution has to be exercised. We suggest specifically avoiding regions in k-space (or in energy space) where dynamic aspects of diffraction from the as prepared surface show already clear indications for strong dynamical effects. Considering the data in Fig. 3.2, we suggest that such may well be the case for Si(111) in the energy region corresponding to n=4-5. Note that not even a clear n=4 spot appears in the data in contrast to the higher energy part where dynamic effects are known to become less important (cf. Fig. 3.2).

3.4 Summary

We have revisited the problem of the validity of the kinematic approximation in LEED. In particular, we aggravate the dispute on its applicability for the purpose of obtaining quantitative information from the analysis of spot shapes in high-resolution LEED (SPA-LEED). Our data on the homoepitaxial growth of Si(111) suggest that dynamic features could be important also for the analysis of disordered systems even in a small range of scattering vector changes. We follow the useful approach, suggested by Henzler, in which the atomic scattering factors are replaced by effective atomic scattering factors related to columns below a particular surface unit cell. Our observations on the behaviour of the in-phase spot height during growth imply that the atomic scattering factors positioned on, or near to, defect sites deviate from those centred in ideal environments in flat terraces. At this point we think it is unlikely that just a deviation from the scattering position of the step atoms from their bulk positions could explain these results. However, to really nail down the importance of dynamic effects in SPA-LEED analysis one should study kinetic roughening of surfaces, which show no inherent tendency for reconstruction. Our

present findings urge caution when trying to obtain information on the vertical distribution of exposed bilayers from the energy dependence of the height of the central spot in the spatial distribution near a Bragg position.

Chapter 4

Homoepitaxy of Si(100)

Novel thin film structures synthesized by MBE or CVD on silicon have found a wide variety of applications in science and technology. Its inherent properties and the low manufacturing costs are the main reasons why silicon devices dominate the microelectronic market. Therefore, it is not surprising that many growth studies have been devoted to Si(100) surfaces. In this respect the simplest model system imaginable is the homoepitaxial growth of Si(100). Smooth and abrupt interfaces between epitaxial layers are often crucial factors for the device's performance, but the smoothness and abruptness of the interface lead to a conflicting demand with respect to the growth conditions. On the one hand the growth temperature should be sufficiently low to reduce atom diffusion and hence intermixing of the layers[1] and dopant segregation, while on the other hand the growth temperature should be sufficiently high to avoid kinetic roughening.

4.1 The network of anti-phase boundaries (APB)

The Si(100) surface is stabilized by a (2x1) surface reconstruction where the atoms of the outermost layer couple in pairs to form dimers in order to reduce the number of dangling bonds of an ideally bulk-truncated surface (see also section 1.1.1). When Si atoms are deposited on Si(100) surfaces at room temperature the atoms are sufficiently mobile to most of them combining quickly to form dimers. The dimers can be divided in two classes: dimers residing on top of the substrate dimer rows and dimers residing in the troughs between the substrate dimer rows. At temperatures slightly above room temperature

[1]While intermixing is not a problem for homoepitaxial growth, it should still be considered at this point. Otherwise, the transfer of possible growth recipes from the homoepitaxial to the heteroepitaxial case, where intermixing is indeed a very crucial issue, would in all probability be condemned to failure when high growth temperatures are used.

($\approx 300 - 350$ K) the on-top dimers are able to diffuse over the substrate dimer rows [Swa96]. At even higher temperatures (≈ 450 K) also diffusion across the substrate rows becomes active [BKG97, KBG97]. As Si islands nucleate and grow on (100) surfaces, the dimer rows in neighbouring islands have a probability of 50% to be in the correct registry. An anti-phase boundary (APB) will form if two islands meet, when their internal dimer rows are not aligned. For the Si(100) surface there are in principle two different APBs (see fig. 1.3), one type of APB runs along the substrate dimer rows (APB_A) and the other runs perpendicular to substrate dimer rows (APB_B). Several authors have pointed out that the latter APB acts as a preferential nucleation site for island growth (e.g. [HD90]). The first type of APB gives, in combination with the fact that the islands are elongated in the dimer row direction, rise to the formation of trenches and double layer steps [WHZ+97]. The anti-phase boundary (APB)-network [ZZWP01] is of key importance for the roughness of the grown layer. In this chapter it will be shown that by changing the temperature during growth the APB network can be manipulated in such a way that smooth layers can be grown at relatively low temperatures. Before demonstrating this with the growth of 15 ML, the temperature dependence of the APB network will be discussed. The size of the APB network is determined from STM, while SPA-LEED is employed to study the annealing behaviour of the APB network in detail.

The investigation will be started by looking at one of the parameters in growth, the number density of islands. The APB network opens a unique way to determine the maximum island number density, especially at high coverages of grown material. Because neighbouring islands have a probability of 50 % to be in the wrong registry the island density extracted from the APB network is four times too low. Thus $N = 4/(< L > \cdot < B >)$, where $< L >$ ($< B >$) is the averaged spacing between APBs in a direction along (perpendicular) to the substrate row direction (see insert in fig. 4.1). In fig. 4.1 a plot of N vs. $1/T$ in the temperature range from RT to 1000 K is shown. The dotted line refers to the work of Mo et al. [MKWL91, PVW92], who measured the island density after deposition of 0.07 ML. The island density depends on the coverage and will reach a maximum at the time just before coalescence sets in. It is exactly this maximum number that is measured with the determination of the island density from the APB network. The kink in the curve at a temperature around 560-600 K is caused by island coarsening, an additional process that becomes active at higher temperatures, which is due to attachment and detachment at kink sites [ZEvL92, KSLW93, PBK+95].

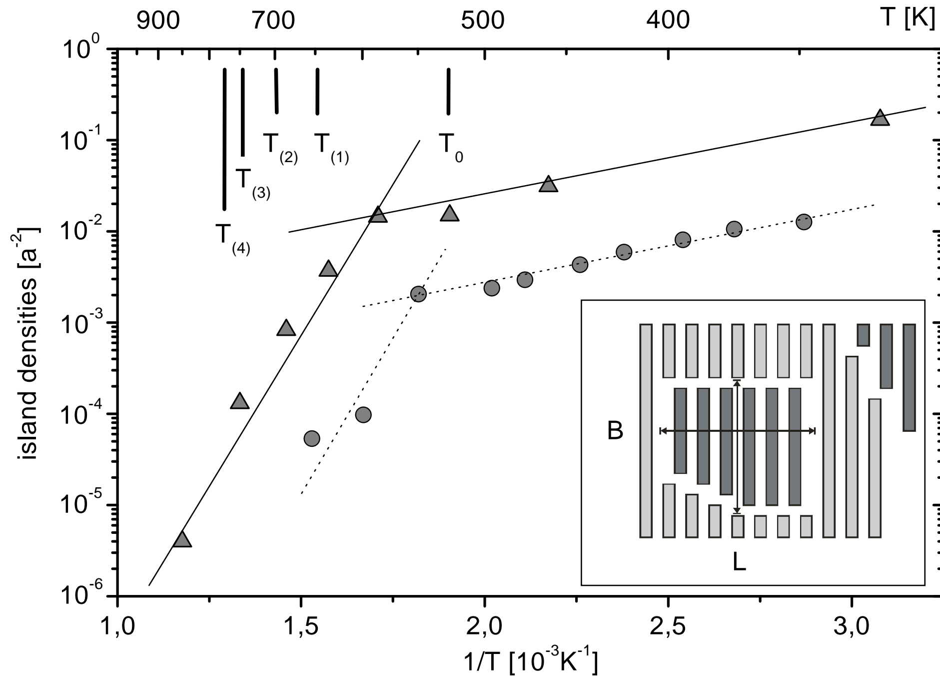

Figure 4.1: Si island densities on Si(100) vs. growth temperature. Up-triangle values are calculated from the APB network. Circle values have been published by Mo et al. [MKWL91, PVW92]. The lines are guides to the eye. T_0 is the growth temperature, $T_{(1)}$- $T_{(4)}$ are the flash temperatures of the SPA-LEED measurement shown in fig. 4.4. The kinks in the curves at a temperature around 560-600 K are caused by island coarsening that becomes active in this temperature range. The kink temperatures of the two curves differ by about 40 K. This can be due to the errors in sample temperature measurement (it is quite complicated to make more accurate temperature measurements for semiconductor samples, because of the surface contamination problem). The slope of the two curves in the temperature range below 550 K is identical and originates from the diffusion process of Si dimers along the dimer rows (1D-diffusion, [MKWL91, Swa96]). The lower right insert visualizes the definition of the spacing L and B between APBs along and perpendicular to the substrate dimer row direction.

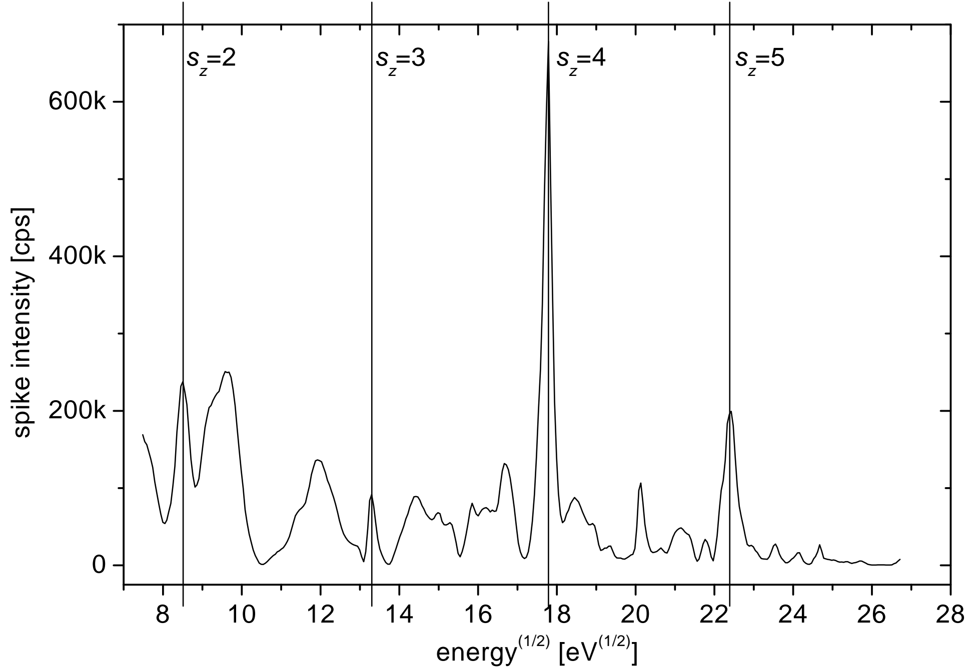

Figure 4.2: I/E curve of the central diffraction spot measured on a clean Si(100) surface at 100 K. It is heavily influenced by dynamic effects at energies up to the in-phase intensity maximum $S_z = 4$. For the definition of the phase number see section 1.2.1. Refer to section 2.2.5 for details about the recording of I/E curves.

.

4.2 Conventional growth

For the real-time SPA-LEED measurements first the appropriate energies for the in- and out-of phase conditions of the central spot have to be determined. Fig. 4.2 shows an I/E curve of the clean Si(100) surface at 100 K. As can easily be seen, the I/E curve is heavily influenced by dynamic effects at energies up to the in-phase intensity maximum at about $18\sqrt{\text{eV}}$ ($S_z = 4$, see also section 1.2.1). At the low electron energies that are predestined for real-time measurements[2] it is difficult to immediately determine the good energies just by means of the I/E-curve itself. The energies that have finally been chosen for the out-of-phase ($7.338\sqrt{\text{eV}}$) and in-of phase ($9.609\sqrt{\text{eV}}$) condition have been found in numerous testing growth experiments using electron energies between $6\sqrt{\text{eV}}$ and $18\sqrt{\text{eV}}$ for the spot

[2]Low energy electrons have a higher surface sensitivity. Furthermore, the Debye-Waller effect reduces the spot intensities when the sample temperature is rising. The decrease at low electron energies is weaker, that's why it is easier (lower gate-time due to higher count rate) to measure the spot intensities at lower energies in a real-time measurement.

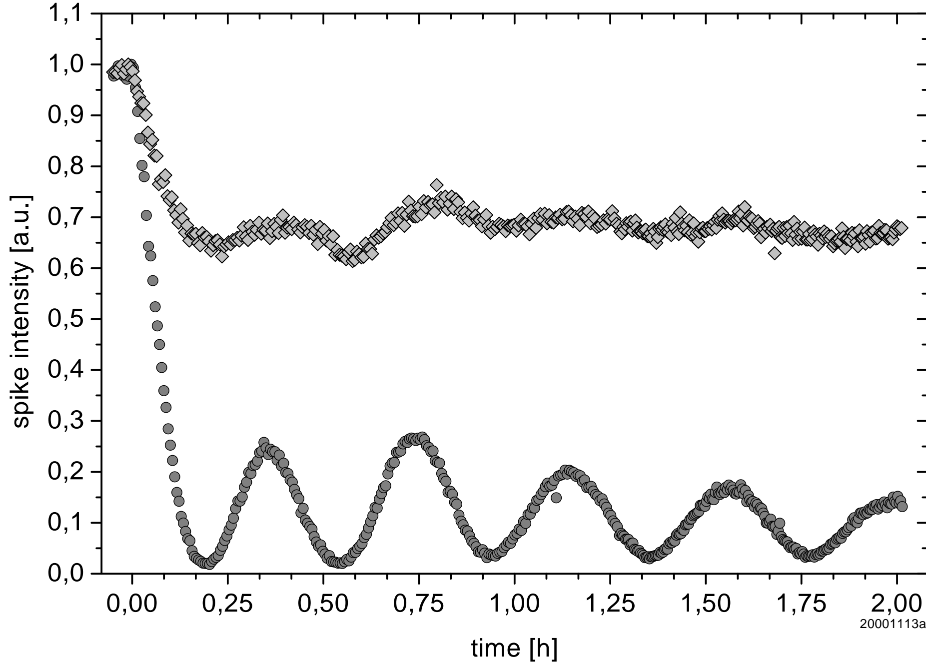

Figure 4.3: Real-time measurement of central spot's spike intensities (normalized, circle symbols: at $7.338\sqrt{\mathrm{eV}}$, out-of phase condition; rhomb symbols: $9.609\sqrt{\mathrm{eV}}$, in-phase condition) during conventional growth of Si on Si(100) at a sample temperature 575 K. The out-of phase intensity oscillates while the oscillation amplitude is decaying. This indicates layer-by-layer growth with a growth front that roughens in the course of the measurement. The in-phase intensity shows weak oscillations, the oscillation maxima are reached after the maxima of the out-of-phase intensity oscillation.

intensity measurements.

Fig. 4.3 shows the spot intensities measured at the chosen energies in real time during the conventional growth of Si on Si(100) at about 575 K. The out-of phase intensity oscillates, the oscillation frequency is in accordance with the evaporation rate (approx. 3 ML per hour in this case). Due to the progressing roughening of the surface the amplitude of the oscillation is decaying from about 27% at the first two intensity maxima to 15% after about 5 grown ML. The in-phase intensity shows weak oscillations, the oscillation maxima are reached after the maxima of the out-of-phase intensity oscillation. This is an interesting observation, because in the case of homoepitaxy on Si(111) the in-phase oscillation maxima were reached before the out-of-phase oscillation maxima (see chapter 3).

This experiment demonstrates that during the growth of Si on Si(100) growth oscillations can well be measured, but, in contrast to the homoepitaxy on Si(111), the growth is

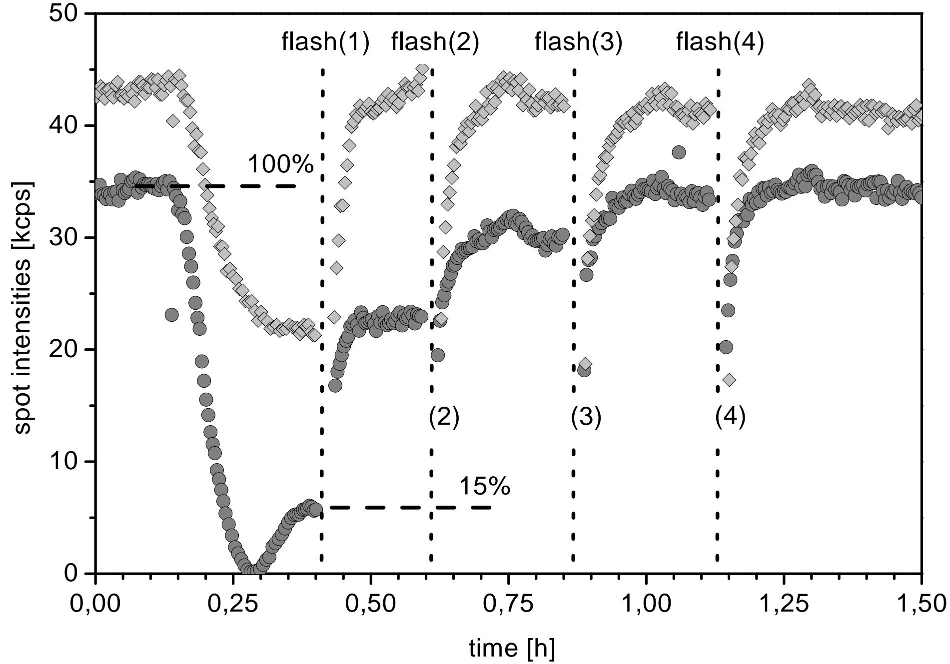

Figure 4.4: Real-time measurement of central diffraction spot intensities during Si growth on Si(100) and the following flash annealing of the grown film (circle symbols: $7.338\sqrt{\text{eV}}$, out-of phase condition; rhomb symbols: $9.609\sqrt{\text{eV}}$, in-phase condition; $R \approx 1$ ML/15 min; $T \approx 525$ K). 1 ML of Si was grown and afterwards gradually flashed to 650 K (1), 700 K (2), 750 K (3) and 775 K (4) (duration of each flash: 1 min). After the flashes the sample quickly cools down to 525 K. In this periods the measured spot intensities rise because of the Debye-Waller effect.

accompanied by a roughening growth front. In the next section, a growth manipulation method will be presented that prevents this roughening.

4.3 Growth manipulation

4.3.1 Smoothing a Si monolayer

Figs. 4.4 shows the intensities of the central SPA-LEED diffraction spot at in-phase and out-of-phase conditions measured during and after the evaporation of Si (rate ≈ 1 ML/15 min) on the Si(100) surface at a temperature of 525 K. In the case of fig. 4.4, 1 ML of silicon has been deposited and flash annealed afterwards to 650 K (1), 700 K (2), 750 K (3) and 775 K (4), 1 min per flash (during the flash annealing the evaporator was switched

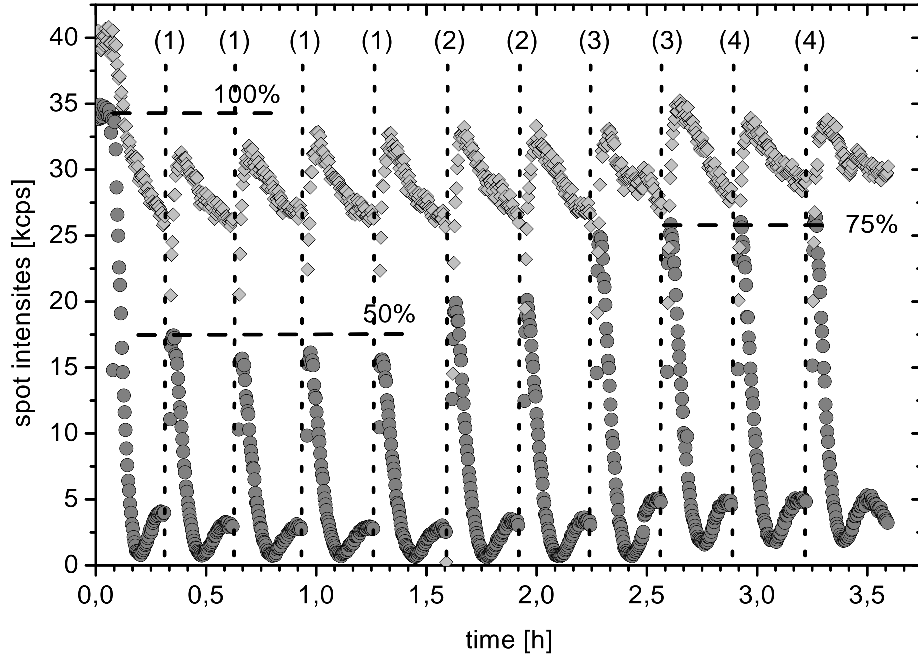

Figure 4.5: Real-time measurement of central diffraction spot intensities during Si growth on Si(100) using kinetic growth manipulation (KGM; circle symbols: $7.338\sqrt{\text{eV}}$, out-of phase condition; rhomb symbols: $9.609\sqrt{\text{eV}}$, in-phase condition; $R \approx 1$ ML/15 min; $T \approx 525$ K). 10 ML of Si were grown applying flash annealing to 650 K (1), 700 K (2), 750 K (3) and 775 K (4) (duration of each flash: 1 min) after every completed ML. During the flash annealing, the evaporation continues. After the flashes the sample quickly cools down to 525 K.

off). At the end of the evaporation, the in-phase intensity is at about 70%, the out-of-phase intensity at about 15% of it's initial value corresponding with the build-up of a rough growth front. Already type (1) flashing is sufficient to get the in-phase intensity back to its initial value indicating a surface with just few defects[3] (in agreement with [WKWvS97] where optical anisotropy measurements revealed the disappearance of defects at 670 K). The out-of-phase intensity increases step by step (66% of the initial value for flash type (1), 87% (2), 97% (3), 100% (4)) with the flashes. Fig. 4.6 a) and b) visualize the effect of flashing using RT STM scans of the Si(100) surface. Scan a) was taken after evaporating a little more than 1 ML at 500 K. It is obvious that nucleation took place in the second layer before the first layer was completed. Scan b) shows the surface with 1 ML grown at 500 K plus a 1 min flash to 660 K. Compared with scan a) less material remains

[3]point-defects such as created during ion-sputtering

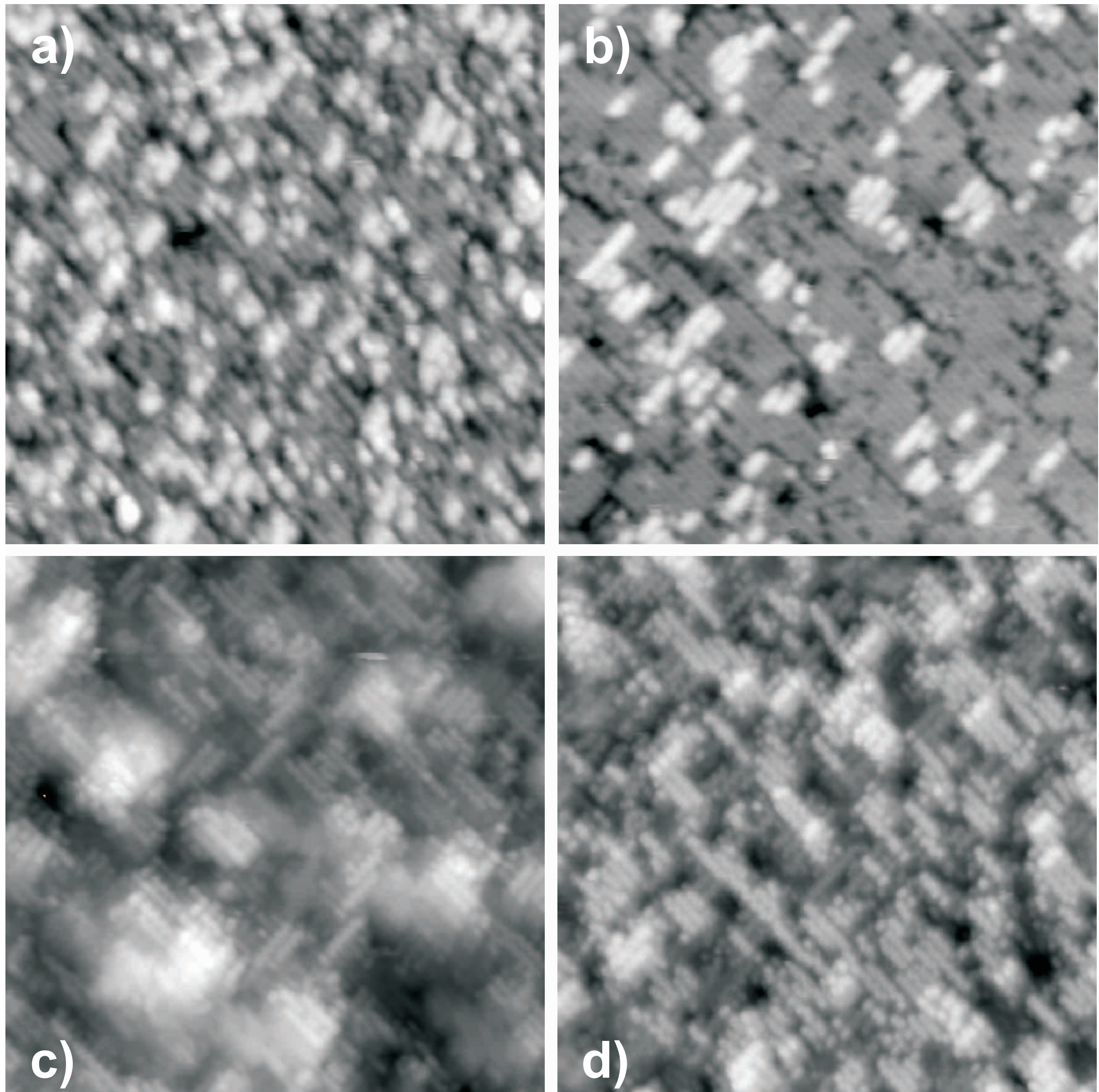

Figure 4.6: STM scans on Si(100) after Si evaporation (quenched to RT), $R_{(a)} \approx 1$ ML/ 17 min, $R_{(b)-(d)} \approx 1$ ML/ 1.7 min. (a) ≈1 ML grown at 500 K (b) ≈1 ML grown at 500 K plus flash to 660 K, 1 min (c) ≈4.5 ML grown at 660 K (d) ≈4.5 ML grown at 500 K applying KGM, i.e. a 1 min flash to 660 K after every completed ML. Tunnelling parameters: -2.0V, 0.5nA. scan width: 250 Å

type	T_{flash}/K	$I_{out-of-phase}/I_0$	θ_1	θ_2	f_{APB}
1ML	-	15%	85%	15%	-
(1)	650	66%	95%	5%	2.5%
(2)	700	87%	98%	2%	2%
(3)	750	97%	99.5%	0.5%	-
(4)	775	100%	100%	0%	< 0.5%

Table 4.1: Calculated coverages and filling factors after growth of 1 ML at 525 K and following flash types (1)-(4), for experimental data see figs. 4.4 and 4.1.

in layer 2, whereas layer 1 is filled to a higher degree. This shows that the evaporated material is distributed over two layers only. The coverages θ_1, θ_2 for the two layers from the out-of-phase intensities $I_{out-of-phase}$ can be calculated using

$$\theta_2 = \frac{1}{4}\left(1 - \sqrt{\frac{I_{out-of-phase}}{I_0}}\right), \; \theta_1 = 1 - \theta_2$$

(assuming that at the out-of-phase intensity maximum a complete ML has been evaporated, see table 4.1 for the results). This flash series shows that a short thermal treatment to a ≈ 200 K higher temperature results for this system in an almost perfectly closed layer. If one would try to reach a similar surface quality by growing 1 ML unmanipulated at a certain *constant* temperature, this temperature would only be found at much higher temperatures (formation of double steps). The reason for the rough growth is that the APB network hinders a complete filling of the first layer, causes nucleation on top of the islands and in this way induces roughening. In the <B>-direction islands cannot grow together and a gap of one lattice unit will remain between the islands. In contrast, an APB_B does not hinder two islands growing together (see fig. 1.3). The fraction of the ML that cannot be held by the layer itself can therefore be defined as f_{APB}. f_{APB} can be calculated as follows from the density of the APB network determined with STM and shown in fig. 4.1

$$f_{APB}(T) = \frac{1}{1 + < B > (T)}$$

Table 4.1 shows a good correspondence between the measured size of the APB network and thus the filling factor f_{APB} and the amount of material that cannot be incorporated in the first layer (θ_2) after annealing. The situation shown in scan b) of fig. 4.6 is not as ideal as expected from the SPA-LEED measurements. This is probably due to the fact

that in the STM UHV system there is no real time probe available making it possible to stop evaporation exactly after completion of a ML, what makes it very hard to produce a completely filled first layer. The error in the amount of deposited material after deposition of 1 ML is estimated as $< 1\,\%$ in case of the SPA-LEED system and $10\,\%$ in case of the STM system.

4.3.2 Flatten thicker Si films

The experiences just described are now applied to grow thicker films in a smooth way. After the completion of each ML grown at a temperature below the coarsening temperature the layer is first annealed to create again a smooth surface with a low defect density. Fig. 4.5 shows the deposition of 10 ML in this way. As soon as an oscillation maximum of the out-of-phase intensity is reached, the sample is flashed (flash types (1)-(4), see above) for one minute. Due to the use of resistive heating, the spot intensity measurements are interrupted during flashing, whereas the silicon evaporation continues. Right after the flashes out-of-phase intensities of $\approx 50\%$ (1), $\approx 60\%$ (2), $\approx 75\%$ (3) and $\approx 75\%$ (4) of the initial values can be measured, in-phase intensities are in the range of $\approx 75 - 90\%$ (1-4) of their initial values. The out-of-phase-intensities are lower than the ones measured after flashing 1 ML. This has two reasons: 1) The evaporation is not interrupted. 2) It takes some seconds till the sample has cooled down from the flash temperature. Due to the Debye-Waller effect the spot intensities are lower at higher temperatures. We found that the evaporating-flashing (1)-cycle can be repeated at least 15 times without noticeable decay of the spot intensities. The same growth experiments have also been performed at lower sample temperatures (down to 425 K), in these cases flashing results in the same spot intensity amplitudes. It is a remarkable result for the homoepitaxy on Si(100) that especially at this low growth temperatures even after the growth of 10 ML the top layer is that smooth. The STM scans in Fig. 4.6 c) and d) show the effect of the applied flashing growth manipulation. As it is hard to visualize thick rough layers with STM the grown layers are only 4.5ML thick. In scan c) the material is grown at 660 K (growth at 525 K resulted in a rough growth front that could not be imaged properly), in scan d) growth took place at 500 K with 1 min flashes after every completed ML.

The growth manipulation method for homoepitaxy on Si(100) that we describe in this paper has a distinctly positive effect on the smoothness of the grown layer. The oscillation amplitude of the SPA-LEED out-of-phase central spot intensity rises from $\approx 10\%$ of the initial value to $\approx 50 - 75\%$ of its initial value (see fig. 4.5). That means that the growing Si layers are filled up to a much higher extent before nucleation in a new layer takes place. Furthermore the growth manipulation results in an absence of the oscillation amplitude

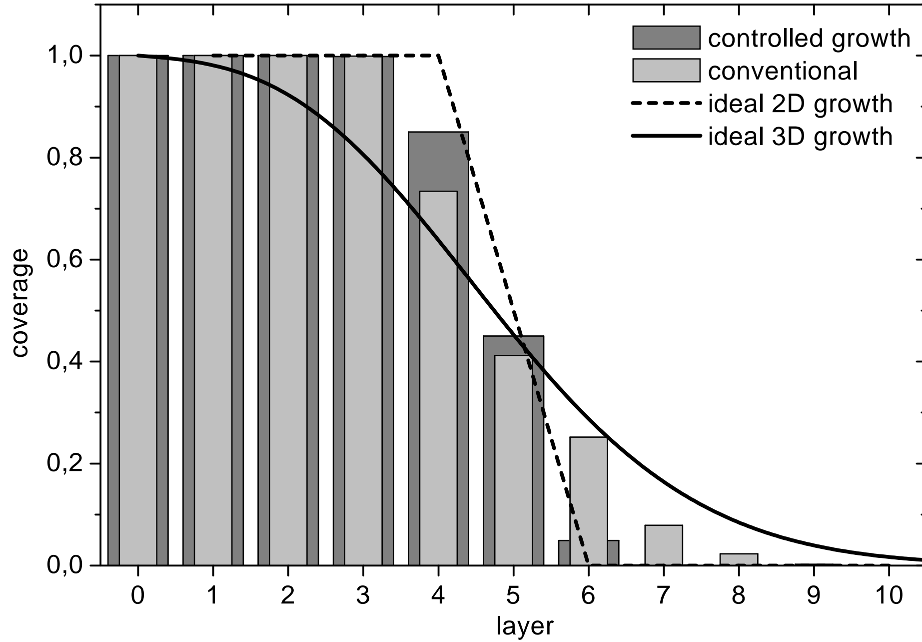

Figure 4.7: Comparison of the grown films (thickness 3.5 ML) after conventional and manipulated homoepitaxy of Si(100): The distribution of material into different atomic layers is plot. Layer 0 is the first bulk layer. For further comparison, the distributions for ideal 2D growth (dashed line) 3D growth (solid line) of 3.5 ML are plotted into the graph. See [EHMC94] for a similar film evaluation.

decay indicating that there is no progressive kinetic roughening during growth.

By carefully evaluating the STM pictures after the growth of 4.5 ML Si with and without applying the growth manipulation method we can make an overview of the distribution of the Si over the visible layers (see fig. 4.7). The surface roughness value can be calculated as [Com95]

$$g = \frac{\sum_n \left(\theta_n^{grown} - \theta_n^{ideal2D}\right)^2}{\sum_n \left(\theta_n^{ideal3D} - \theta_n^{ideal2D}\right)^2}$$

In case of ideal 2D growth, i.e. the type of growth where nucleation in layer $n+1$ starts only if layer n is filled up completely, g equals to 0, whereas $g = 1$ for ideal 3D growth. From our conventional growth data $g = 0.73$ is obtained, the controlled growth data lead to $g = 0.31$. Even if the results from our STM measurements do not completely meet the results in terms of surface quality after growth from the SPA-LEED measurements, the g values express the positive effect of the growth manipulation method.

The basic idea behind our growth recipe is as follows: during the growth of 1 ML

silicon at a fixed low temperature a very high island density is created. Without growth manipulation, this high island density would lead to a high density APB network, with rough growth as a consequence. But during the flash following the growth, the islands can quickly redistribute their material towards neighbouring islands and in that way drastically decrease the APB network density, just because they are small. A lower APB network density on the other hand decreases the chance for nucleation of islands in the layer above (see e.g. [HD90]). These are also the reasons, why the surface is much flatter after manipulated growth than after continuously growing at the high flash temperatures. At high temperatures, the islands are too large to be able to reduce the APB network density in a reasonable time [NM65a, NM65b, Nic66, EMRC98].

4.3.3 Failure of the concept of two mobilities

The principal difference of the manipulation method just described for Si on Si(100) with the well-known kinetic growth manipulation (KGM) methods that have been successfully used on unreconstructed metal surfaces should be pointed out once more: On unreconstructed metal surfaces, KGM aims specifically at the additional energy barrier at the island edges for downward diffusion [EH66, SS66, KPVC90] to enhance the interlayer mass transport (e.g. the concept of two mobilities or better: the concept of two island densities [RST+93, RPC95, RLW+95]). When such a KGM method is applied to enhance the growth on reconstructed semiconductor surfaces, it will fail, because it does not overcome the problem of the building-up APB network and the corresponding preferred island nucleation in higher layers.

To demonstrate this failure, the concept of two mobilities was applied to the system Si on Si(100) (see fig. 4.8). The concept of two mobilities consists of growing the first part of every ML at a lower temperature and afterwards continuing the growth for the rest of the ML at a higher temperature. The idea behind this is the creation of very small islands in the first phase of every ML's growth. This is done to increase the chance of atoms that land on top of those islands to diffuse downwards when the temperature is higher in the later stage of every monolayer's growth overcoming the additional energy barrier at the island edges for downward diffusion. The more adatoms overcome the additional energy barrier and diffuse downwards, the lower is the chance for island nucleation on top of the islands.

Fig. 4.8 shows the intensities of the central SPA-LEED diffraction spot at in-phase and out-of-phase conditions measured in real-time during the growth of Si on Si(100) using the concept of two mobilities. Seven ML of Si have been deposited; during the first half of every ML's deposition the sample temperature was 375 K, during the second half 575

K. The strange-looking scaling in fig. 4.8 is due to the fact that at the very beginning of the experiment the sample is at the lower temperature of 375 K. Because of the Debye-Waller effect, the spot intensities are about twice as high as at 575 K. Compared to the conventional case (see fig 4.3) a slightly enhanced out-of phase oscillation amplitude is recognizable (40% compared to 30% in the unmanipulated case). But what is more important is the fact that the decay of the out-of phase oscillation amplitude that was observed in the unmanipulated case is still present. This shows that the concept of two mobilities as a kinetic growth manipulation method is (in contrast to the manipulation method aiming at the APB network density) not able to suppress the progressive roughening of the surface in the case of homoepitaxy of the reconstructed Si(100).

4.4 Conclusions

A kinetic growth manipulation (KGM) method that aims at the density of the anti-phase boundary (APB) network coming up during growth experiments on the reconstructed Si(100) surface has been developed. It has been demonstrated that this KGM method can be used successfully to prevent progressive roughening of the growth front during homoepitaxy of Si(100). As a consequence, films with a thickness of many ML can be grown in a flat and smooth manner. Furthermore it has been shown, that growth manipulation methods like the concept of two mobilities that work successfully against the additional energy barrier at the island edges for downward diffusion in epitaxy of unreconstructed metal surfaces are not successful in preventing the progressive roughening of the growth front in the case of the reconstructed Si(100) surface.

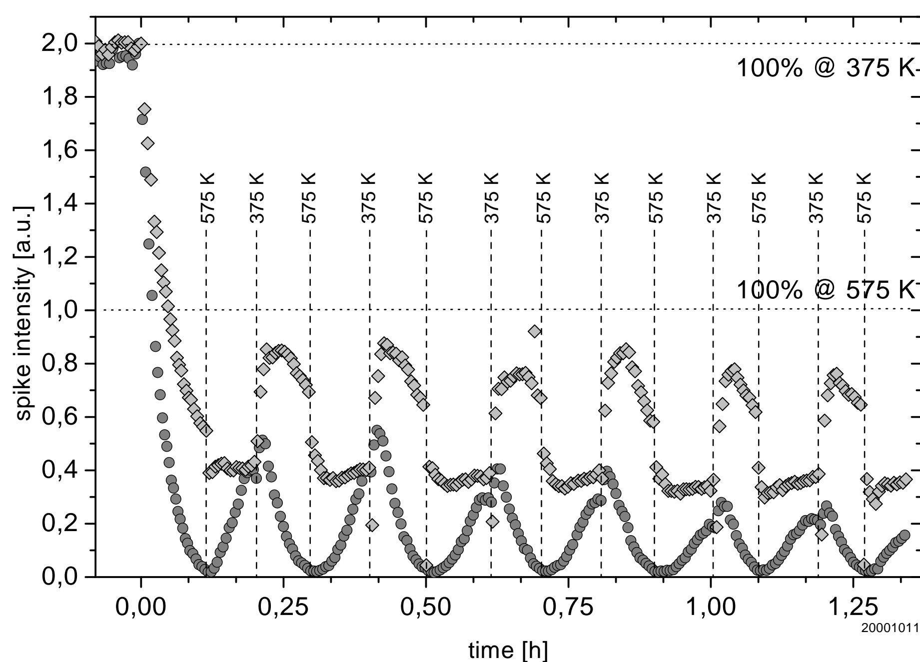

Figure 4.8: Real-time measurement of central diffraction spot intensities during Si growth on Si(100) using the concept of two mobilities as kinetic growth manipulation method (circle symbols: $7.338\sqrt{\mathrm{eV}}$, out-of phase condition; rhomb symbols: $9.609\sqrt{\mathrm{eV}}$, in-phase condition; $R \approx 1$ ML/12 min). The sample temperature is 375 K in the first half of the deposition of every ML (till the minima of the out-of-phase intensity oscillations) and 575 K in the second half (till the maxima of the out-of-phase intensity oscillations). The temperature changes are marked with vertical lines. The scaling of the spot intensities is different than in the figures before; this is due to the fact that at the very beginning of the experiment the sample is at the lower temperature of 375 K. Because of the Debye-Waller effect, at 375 K the spot intensities are about twice as high as at 575 K.

Chapter 5

Si heteroepitaxy on Ge(100)

Silicon-germanium heterostructures are very attractive for the fabrication of novel electronic and optoelectronic devices [GMT99, Wul97]. Therefore, the growth of Ge on Si has been studied intensively during the last years (see for instance [MSK+89, MSSL90, WCZL95, HAL89, Hoe90] or the detailed studies of Horn-von Hoegen [HvH99] and the references therein). Surprisingly, much less has been published about the inverse system [XZM+94, KG94, TXK+94, KUT89, DBBK98, DBKF99, YWV+93], comprising primarily diffraction studies of gas source and molecular beam epitaxy. As Ge has a lower surface free energy than Si, the preferred growth mode of Si on a Ge surface is to form clusters (three-dimensional growth)[1]. Wulfhekel finds with his STM study almost ideal 3D growth of Si on Ge(100) [WZH+98, Wul97]. Furthermore he demonstrates how the three-dimensional growth can be turned into much smoother growth by using kinetic growth manipulation. By way of contrast, Dentel et al. conclude from their RHEED MBE studies that growth takes place in layer-by-layer (in a wide range of temperatures and evaporation rates) mode until a *critical thickness* is reached (Stranski-Krastanov growth).

It is of key importance for a heteroepitaxial system as Si on Ge up to which temperature the films are stable in relation to intermixing. Hoeven et al. conclude that above 680 K a significant diffusion of Si into Ge occurs [HAL89, Hoe90, AKBB96]. However, other publications suggest that even at temperatures as low as room temperature intermixing phenomena occur at this interface [LMC92, QSL00, KT89].

The experiences from the successfully performed growth manipulation for Si on Si(100) (see chapter 4) and the ideas of Wulfhekel et al. concerning the manipulation of Si growth on Ge are the basis for the attempt to reach smooth flat Si films in growth experiments

[1] From the thermodynamical point of view. A thermodynamically stable structure is dictated by the surface and interface free energies and by the difference in the lattice constant of the substrate and the material that is being deposited. In the case of Si and Ge the interface energy is small, so the growth type will depend mainly on the minimization of the surface free energy. [GMT99]

monitored by real-time SPA-LEED measurements and supplemented by ellipsometry.

5.1 Conventional growth at 525 K

The first experiment to be presented is the conventional (i.e. conventional) growth of Si on Ge(100) at a temperature of 525 K. According to Hoeven et al., at this temperature intermixing of Si and Ge should not play a significant role.

For heteroepitaxial systems the definition of the term *out-of-phase* is not unproblematic in diffraction studies [HvH99]: As the vertical distances between grown layers are not necessarily the same as those of the substrate, the out-of-phase condition for the growing layer is not necessarily at the same electron energy as an out-of-phase condition for Ge(100) homoepitaxy. Beyond that, depending on the development of the heterogrowth, the out-of-phase condition can even shift during the growth, if for example relaxation of the grown layer takes place from a certain film thickness on. That's why, during the SPA-LEED real-time growth monitoring of Si on Ge(100), the intensity of the central diffraction spot is always measured at least at five electron energies to increase the chance of getting close to in-phase and out-of-phase condition. These energies are selected in the following way: From the I/E curve of the clean Ge(100) surface (see fig. 5.4 b) the energies for Ge(100) in-phase conditions can be extracted; the energies are then evenly distributed between two neighbouring in-phase conditions. The phase number S_z is defined as (E: electron energy, ϕ: inner potential (in units of eV), h: vertical atomic layer distance (in units of Å), $E_0 = 150.4 eV$ Å^2, see also chapter 1.2.1):

$$S_z = 2 \cdot h \cdot \sqrt{\frac{E + \phi}{E_0}}$$

Fig. 5.1 shows the normalized intensities of the central diffraction spot at energies between the in-phase conditions $n = 2$ and $n = 3$ during the growth of approx. 12 ML Si on Ge(100) at 525 K [2]. Also, the intensity of one of the half-order spots has been measured to get information about how the (2x1) reconstruction behaves during the growth experiment.

During the whole growth experiment, the intensity of the half-order spot stays almost constant at its initial level indicating that the (2x1) reconstruction remains unimpaired. Since an exact (to the extent visible in fig. 5.1) compensation of the consequences of possible changes of the phase conditions for the half-order peak by a varying atomic scattering

[2] Low electron energies are preferred, because low energy electrons have a higher surface sensitivity. Furthermore, the Debye-Waller effect reduces the spot intensities when the sample temperature is rising. The decrease at low electron energies is weaker, that's why it is easier (lower gate-time due to higher count rate) to measure the spot intensities at lower energies in a real-time measurement.

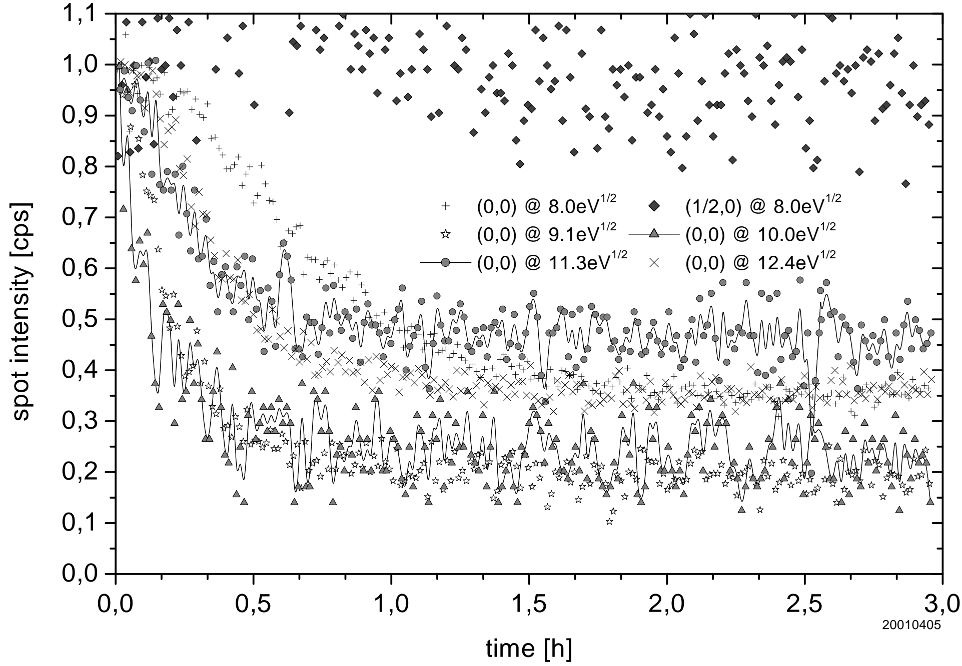

Figure 5.1: Real-time measurement of the central diffraction spot intensity at 5 phase conditions between the Ge bulk in-phase conditions $S_z = 2$ and $S_z = 3$ and half-order spot intensity during conventional growth of approx. 12 ML Si on Ge(100) at 525 K.

factor would be highly unlikely, it can be concluded that phase change effects are absent or at least minimal. Note that since we are dealing exclusively with diffraction from the exposed layer in the fractional order peak considered here, a different inner potential for film and substrate does not play any role. So we can safely conclude that the intact half-order peak intensity is indicative of high quality epitaxial growth.

All five intensities of the central spot decay during the first half of the experiment to values between 20% and 50% of their initial values. The stationary intensities indicate that the growth is neither three-dimensional nor layer-by-layer nor any combination of those two modes. It rather indicates that after an initial phase of the experiment in which about 3 ML are deposited the surface morphology remains stationary like in a step-flow situation. The overall intensity decrease can be attributed to a change in the reflectivity of the sample as after the growth experiment, the diffraction pattern of the surface looks very similar to the one of clean Ge(100) only at first sight. Fig. 5.2 shows a more than 2 BZ wide two-dimensional scan of the diffraction pattern recorded at an electron energy of 135eV and a sample temperature of 100K. Apart from central and first order spots, all half-order and c(4x2) spots are present. A closer look reveals weak facets spots (see fig.

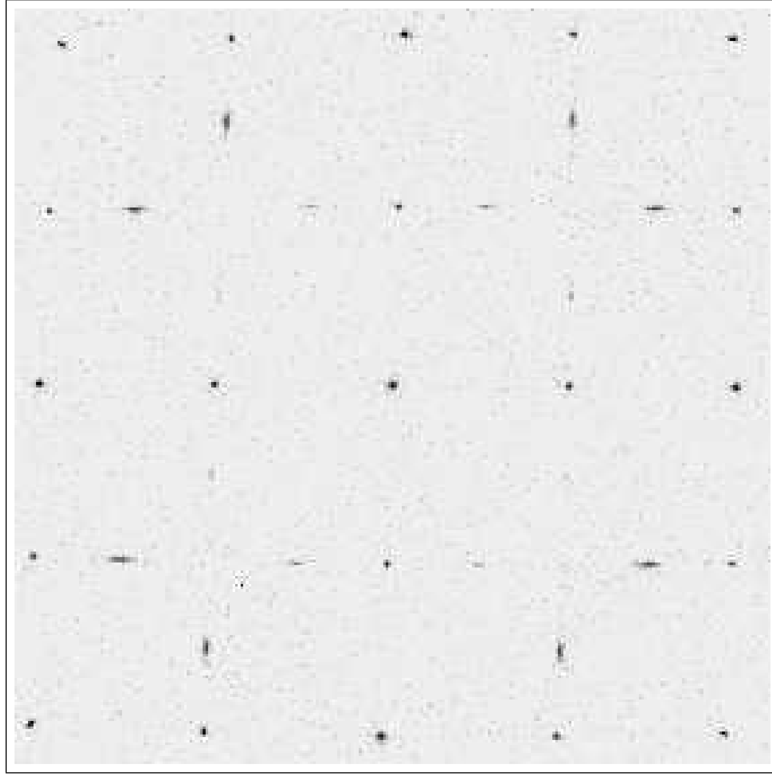

Figure 5.2: Two-dimensional intensity scan of the Ge(100) diffraction pattern (width approx. 2.2 BZ) after the growth experiment shown in fig. 5.1 recorded at an electron energy of 135eV and a sample temperature of 100 K. Central spot, first order spots, half-order spots and the spots of the c(4x2) reconstruction are present.

5.3) in the diffraction pattern. The facet angle amounts to approx. 55°, i.e. (111) oriented facets. This indicates that the surface has roughened, although the low intensity of the facet peaks point to a very limited number of facets. The facet peaks can origin from so called *hut clusters* that possibly build up as a consequence of surface stress, allowing strain relaxation (see e.g. [MSSL90]).

The I/E curve of the surface recorded after the growth experiment (see fig. 5.4) is at first sight different from both the I/E curve of the pure Si(100) and Ge(100) surfaces: Especially the positions of the in-phase-peaks don't match. However, if the I/E curve that was taken after the growth experiment is contracted on its energy axis by a factor of $f_{I/E} = 0.964$, most of its peaks are at the same positions as the peaks of the I/E curve recorded on the clean Ge(100) surface (see fig. 5.5) A contraction suffices to get the peaks of both spectra at the same position, no additional shift, i.e. a change in inner potential was needed. This suggests the interpretation of the outermost layers of the grown film as

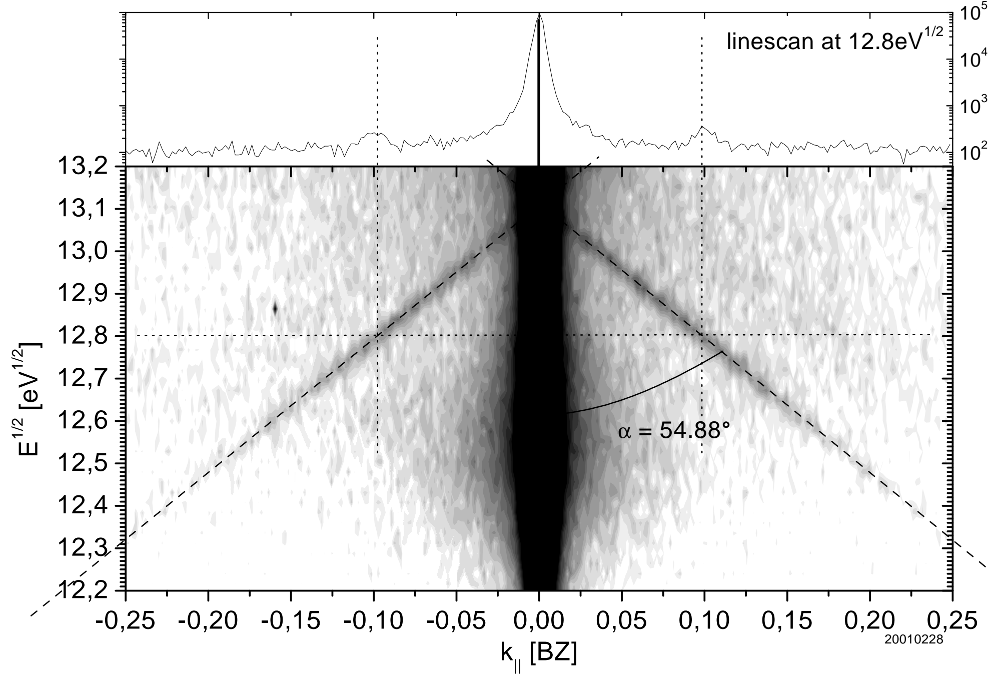

Figure 5.3: Facet-peaks measured on Ge(100) after Si deposition (approx. 12 ML at 525 K, see fig. 5.1). In the upper panel the one-dimensional intensity scan at $12.8\sqrt{\text{eV}}$ is set out to make clear that the facet-peaks are orders of magnitude smaller than the spike of the central spot. The measurement was performed at a sample temperature of 100 K.

being pure Ge-like ones, but with a different interlayer distance. With the energies of the two I/E-curves being related as

$$E_{Ge(100)} = f_{I/E} \cdot E_{525K}$$

the modified interlayer distance h_{525K} reads ($\phi < E$, $f_{I/E} \approx 1$)

$$h_{525K} \approx \sqrt{f_{I/E}} \cdot h_{Ge(100)}$$

If one assumes that the lateral lattice constant $a_{Ge(100)}$ has not changed for the epitaxial film, the effective cubic lattice constant c_{525K} for the grown film can be calculated as (conservation of the atomic volume)

$$c_{525K} = \sqrt[6]{f_{I/E}} \cdot c_{Ge(100)} = 0.994 \cdot c_{Ge(100)}$$

This effective lattice constant is much closer to the one of pure Ge than the one of pure Si (4.2% smaller than Ge). This suggests that the evaporated Si has intermixed with the

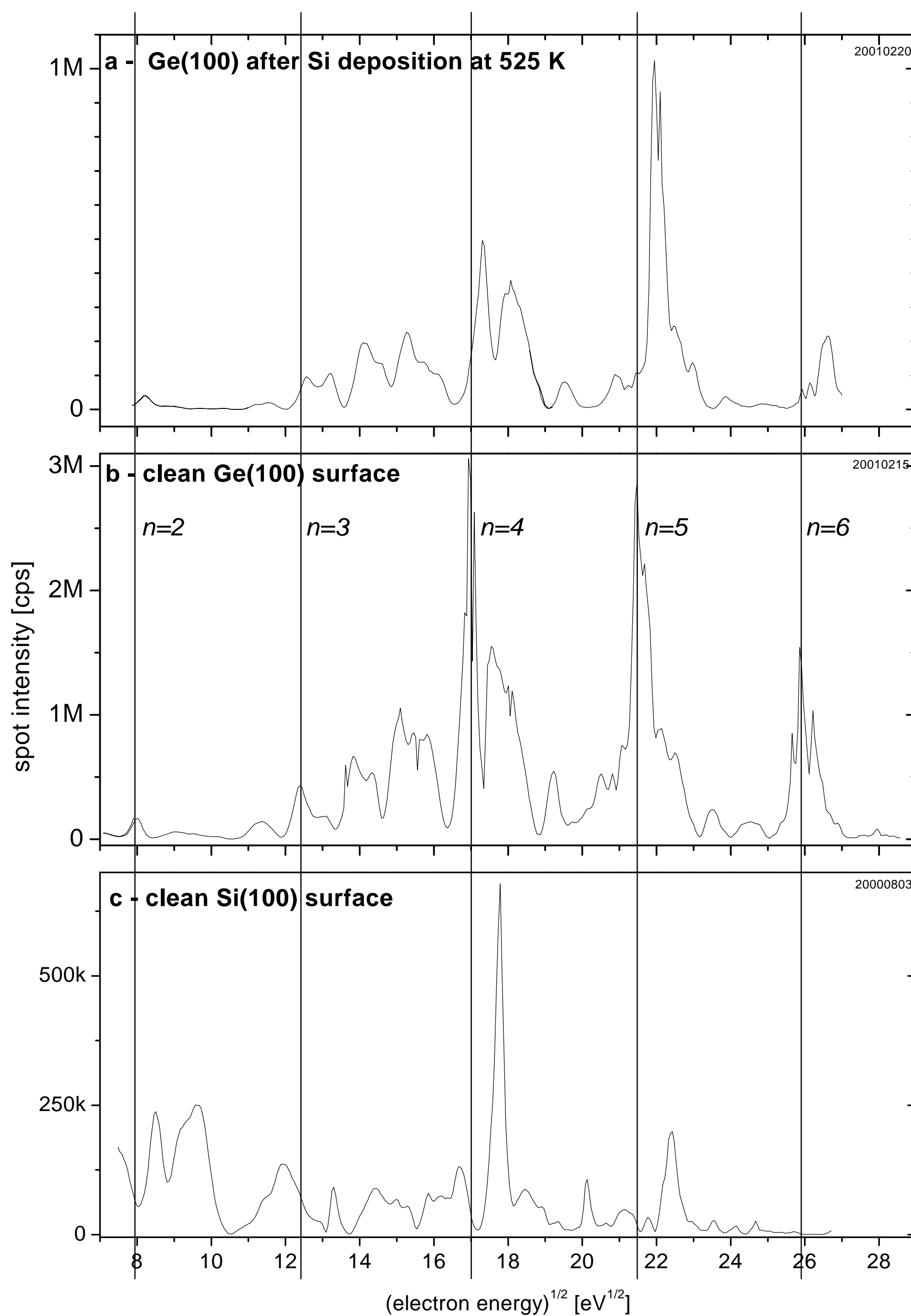

Figure 5.4: I/E curves of: (a) Ge(100) after Si deposition (approx. 12 ML at 525 K, see fig. 5.1). (b) clean Ge(100). (c) clean Si(100). All I/E curves were recorded at a sample temperature of 100 K. The vertical lines represent the in-phase conditions for clean Ge(100).

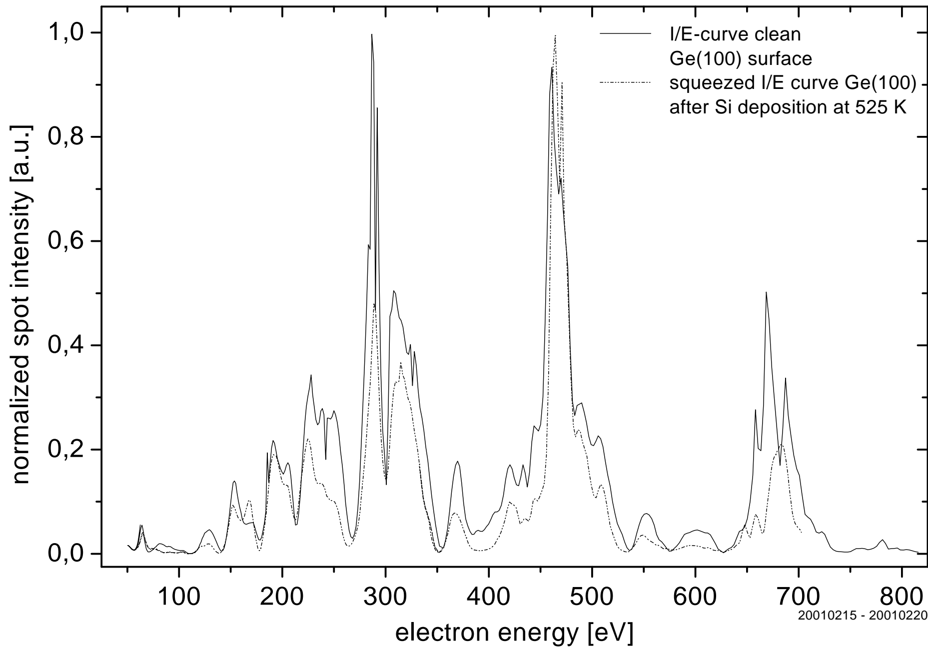

Figure 5.5: I/E curves of clean Ge(100) and Ge(100) after Si deposition (approx. 12 ML at 525 K, see fig. 5.1). The latter is contracted in x-direction by a factor of 0.964. Both I/E curves were recorded at a sample temperature of 100 K.

Ge forming an alloy. From literature, the alloy composition corresponding to the measured value of the effective lattice constant can be determined as 10% Si and 90% Ge. This would indeed stand for an unexpected, but very significant presence of intermixing at 525 K.

After the growth experiment just described spectroscopic ellipsometry measurements have been performed. Fig. 5.6 shows besides the measured optical absorption a) (after the growth experiment) and b) (clean Ge(100)) the calculated absorption curves c) - g), which represent SiGe alloys of different compositions from almost pure Ge to almost pure Si.

For a 12 ML thick Si film on Ge grown at a temperature that is safe concerning intermixing one should expect that the recorded ellipsometry curve a) corresponds to the calculated curve g) of almost pure Si. As can easily be seen, this is not the case. On the contrary, curve a) seems to correspond much more to the curves that belong to those SiGe alloys with a low fraction of Si (11%-20%). This means (in addition to the conclusion from the I/E-curves) that two independent and consistent indications have been found for significant intermixing of Si and Ge at temperatures lower than 670 K. This is in contradiction to the results of Hoeven et al [HAL89, Hoe90, AKBB96] and supports the statements of other authors that predict intermixing phenomena at lower temperatures

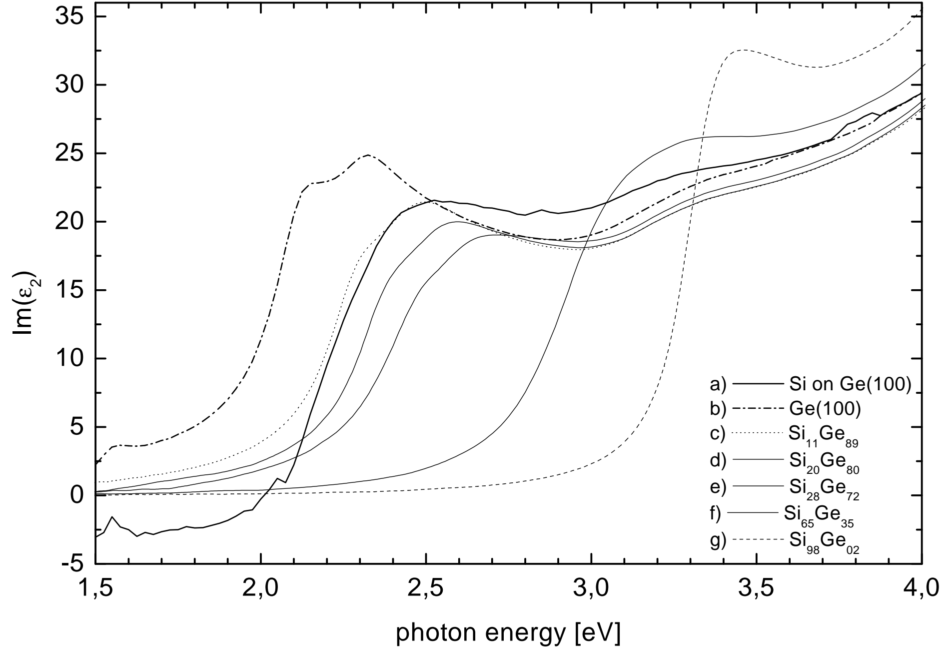

Figure 5.6: Ellipsometrically determined optical absorption of (a) Ge(100) after Si deposition (approx. 12 ML at 525 K, see fig. 5.1). (b) clean Ge(100). Both curves were recorded with the samples being at RT. The curves (c)-(g) are resulting from database values for SiGe alloys.

[LMC92, QSL00, KT89]. Of course one has to keep in mind that in the case of the measurement just described, the sample is held at elevated temperatures for about 3 hours. This is more than 12 times longer than the period that has been used by Hoeven et al. in their annealing experiments.

Comparing the results of Hoeven et al. to the ones presented in this thesis, one could obtain a crude estimate of the energy barrier E_d for in-diffusion of Si into Ge at these low temperatures. The diffusion coefficient D is usually given by

$$D \propto \exp\left(-\frac{E_d}{kT}\right) \tag{5.1}$$

The 12 times longer period needed for diffusion then gives an estimation for the energy barrier by (with T_H the temperature from which in-diffusion becomes significant according to Hoeven et al., T_p is the temperature mentioned in the last sections)

$$12 = \frac{\exp -\frac{E_d}{kT_H}}{\exp -\frac{-E_d}{kT_p}} \tag{5.2}$$

From this, an energy barrier of 0.5 eV can be calculated. This value is significantly lower than the about 2 eV known for Si in bulk Ge diffusion at temperatures above 900 K. However, this is only a crude estimation that neglects the fact that in the presented experiments the sample is held at the higher temperature during deposition instead of a post anneal.

Also a second approach yields an energy barrier lower than 2eV: With 10 ML deposited and 10 % of this film being silicon, one can assume that silicon is spread over about 100 ML during the experiment. The sample is at a temperature of $T = 525$ K for a time in the order of magnitude of about $\Delta t = 10^4$ s. With

$$\bar{x}^2 = (100 \cdot h_{525K})^2 = \nu_0 \cdot \exp\left(-\frac{E_d}{kT}\right) \cdot \Delta t\,, \quad \nu_0 = 10^{13} s^{-1} \tag{5.3}$$

the value of E_d can then be calculated as 1.4 eV, which is also significantly lower than 2 eV.

Room temperature measurements have already shown that intermixing (interchanges, an intermixing phenomenon) at the very surface occurs for Si on Ge(001) [QSL00]. This first step in the intermixing process is thus already active at lower temperatures than the deposition temperature. At the growth temperatures, intermixing is not limited to the first layer, i.e. for instance a surfactant like swimming of one Ge layer, but a thorough in-diffusion occurs. A driving force behind this might well be the lower interface free energy of Ge.

Anyway, the fact that intermixing of Si and Ge occurs at 525 K means that the sample temperatures for the growth experiments have to be chosen considerably lower in order to reach the aim of well-defined films with a chemically sharp interface. In the next section, these measurements will be described.

5.2 Conventional growth at 343 K

In the following experiment Si is grown on Ge(100) at a much lower sample temperature (343 K) in order to avoid intermixing phenomena. Fig. 5.7 shows the normalized intensities of the central diffraction spot, again at five energies between the in-phase conditions $n = 2$ and $n = 3$. Like in the experiment described in the last section, the intensity of one of the half-order spots has also been measured to get information about how the (2x1) reconstruction behaves during the growth experiment.

The central spot intensity at $11.3\sqrt{\text{eV}}$ is decaying strongest in the initial phase of the growth experiment. After the decay, four weak intensity oscillations at a low level are recognizable: After a first weak oscillation, the second oscillation reaches an amplitude of about 9% of the initial intensity. From the second oscillation on, the oscillation amplitude is diminishing till there are finally no oscillations visible any more after the fourth one.

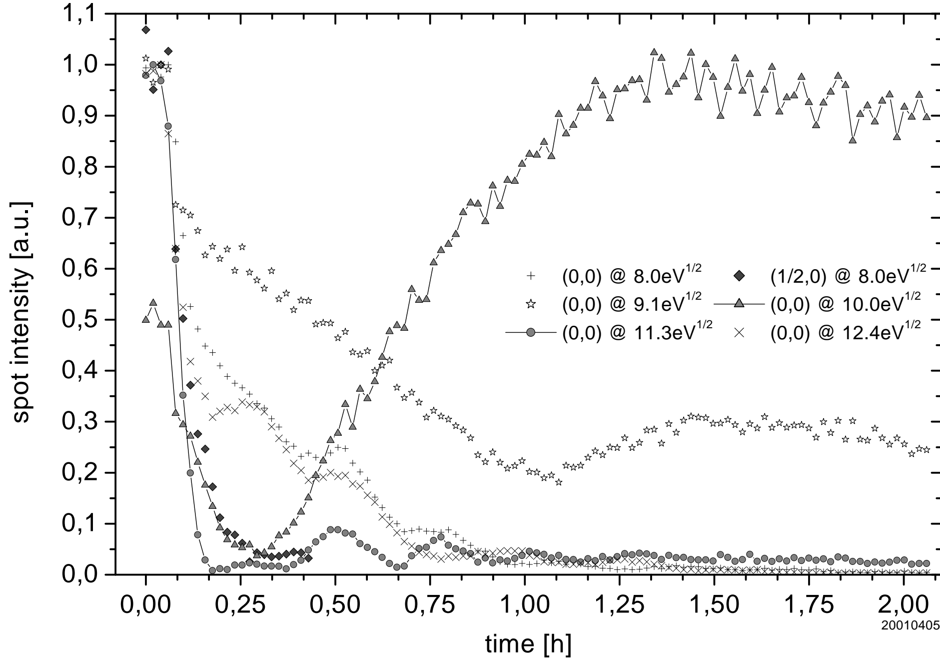

Figure 5.7: Real-time measurement of the central spot intensity at 5 phase conditions between the Ge bulk in-phase condition $n = 2$ and $n = 3$ and half-order spot intensity during conventional growth of Si on Ge(100) at 343 K, evaporation rate approx. 4 ML/h. The intensity values of the central spot at $10.0\sqrt{\mathrm{eV}}$ (up-triangles) have been downscaled by a factor of two.

The spot intensity oscillates with a frequency of about 4 oscillations per hour. With the evaporation rate being about 4 ML per hour, one oscillation can roughly be identified with one ML of grown Si. The properties of the $11.3\sqrt{\mathrm{eV}}$ spot intensity just described let this energy be the one with the most out-of-phase like characteristics for Si on Ge and the parameters in use.

The intensities of the central spot at $8.0\sqrt{\mathrm{eV}}$ and $12.4\sqrt{\mathrm{eV}}$ decay less in the initial part of the experiment. An oscillation of small amplitude is modulating their decay. Till the second oscillation maximum their oscillation matches the one of the $11.3\sqrt{\mathrm{eV}}$ intensity. From the third maximum on, the oscillations have a difference in phase. With these properties, the $8.0\sqrt{\mathrm{eV}}$ and $12.4\sqrt{\mathrm{eV}}$ intensities resemble the in-phase intensities of the Si on Si(111) measurements (see e.g. fig. 3.1).

The intensity of the half-order spot decays very rapidly. After little more than 15 minutes or 1 ML respectively the spot has even completely vanished. That's why its intensity is only drawn till that time, as the spot cannot be distinguished from the background

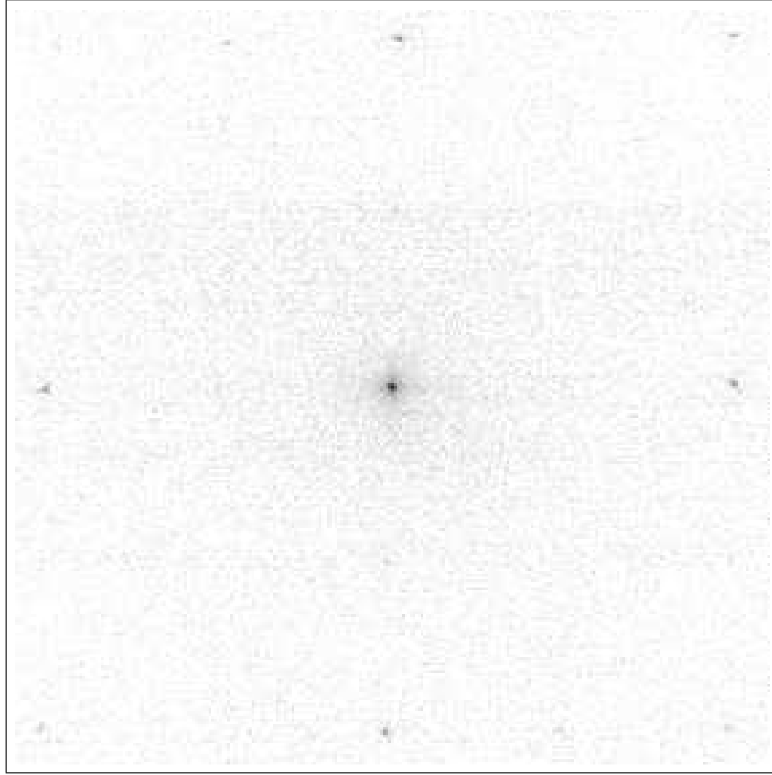

Figure 5.8: Two-dimensional intensity scan (width approx. 2.2 BZ) of the Ge(100) diffraction pattern taken after Si growth (8 ML, see fig. 5.7) at an electron energy of 304.7 eV and a sample temperature of 100 K. All reconstruction spots have practically disappeared.

noise any more. An approx. 2 BZ wide two-dimensional scan of the diffraction pattern that was recorded after the experiment with the sample being quenched to 100 K and an electron energy of 304.7 eV (see fig. 5.8) demonstrates that all the reconstruction spots have practically disappeared (because during the recording of the 2D scan the temperature was almost 250 K lower than in the course of the real-time measurements very weak remains of the half-order spots are faintly observable due to the weaker Debye-Waller effect at these low temperatures). The disappearance of the spot intensity after little more than 1 ML film thickness means that the dimer reconstruction is no longer present indicating non-epitaxial growth.

The behaviour of the $9.1\sqrt{\text{eV}}$ and $10.0\sqrt{\text{eV}}$ intensities is peculiar: after a distinct intensity minimum in the beginning of the measurement, the $10.0\sqrt{\text{eV}}$ intensity rises to values non less than about twice its initial value; then slowly decaying in the sequel. In case of $9.1\sqrt{\text{eV}}$, the intensity starts rising again after a moderate decay of about one hour.

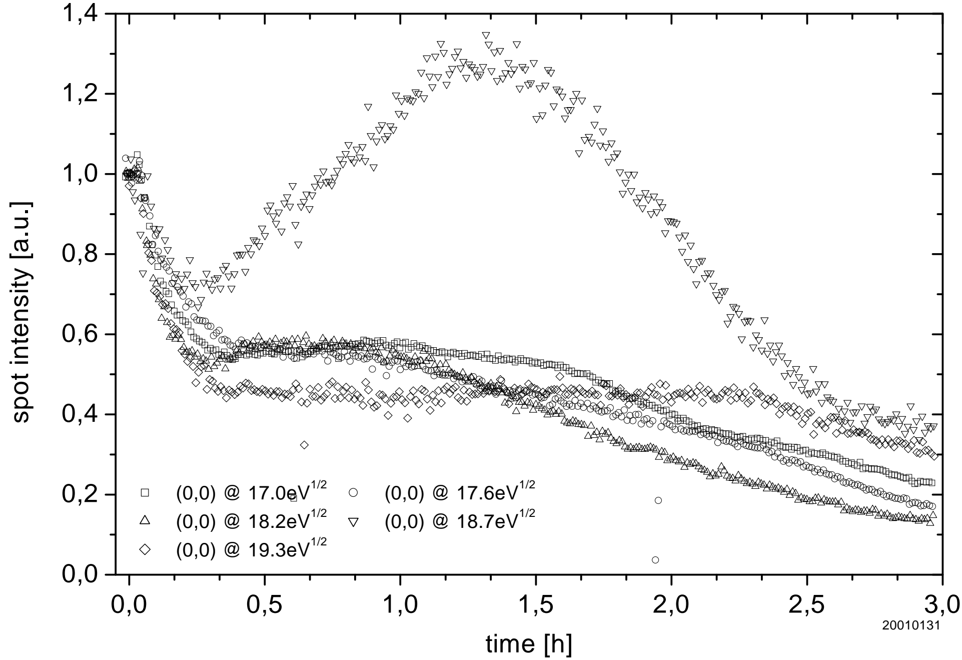

Figure 5.9: Real-time measurement of the central spot (at 5 higher energies) intensity during conventional growth of Si on Ge(100) at 325 K.

This behaviour cannot be explained with either in-phase or out-of-phase characteristics.

Endeavouring to find an electron energy range that is free of such strange spot intensities the real-time measurement was repeated under almost the same circumstances as the one shown in fig. 5.7 but now at quite high electron energies between $n = 4$ and $n = 5$. In fig. 5.9 the central spot intensities at five energies between $17.0\sqrt{\mathrm{eV}}$ and $19.3\sqrt{\mathrm{eV}}$ during Si evaporation (sample temperature 325 K, evaporation rate approx. 4 ML per hour) are plotted [3].

The spot intensities (except the one with the energy $18.7\sqrt{\mathrm{eV}}$) initially decay rapidly to about half of their initial intensities. At that level the intensities stay more or less constant for 3-8 more ML (depending on the energy). Afterwards the decay continues slowly. The $18.7\sqrt{\mathrm{eV}}$ spot intensity shows a completely different behaviour; it displays a maximum with an intensity of approximately 1.3 times its initial intensity.

These intensity developments are even less in agreement with what is expected for

[3] Using high electron energies can be problematic: Firstly the surface sensitivity is lower (lower electron energies have yielded a better quality of real-time measurements for all the experiments on Si(111) and Si(100)), secondly the Debye-Waller effect suppresses spot intensities at higher energies more than at lower energies.

kinetic growth modes then the ones recorded at low electron energies. The intensity developments at high and low electron energies are not even similar. Strong dynamic effects may well play a role in this behaviour. It is surprising, that the higher electron energies seem to be more affected by this. After the growth experiments (figs. 5.7 and 5.9 respectively), an I/E curve has been recorded (see fig. 5.10). At higher energies ($n = 4, \ldots, 6$), the in-phase peaks are at the same energies as for clean Ge(100). However, at lower energies ($n < 4$) there are no peaks at clean Ge(100) in-phase energies, but well at out-of-phase energies. The comparison of the two I/E-curves suggests that the electronic structure of the films grown at low temperatures differs from the one found for clean Ge(100).

In the last section it was shown that the temperature range usable for the growth of Si on Ge is at its high border limited by the occurrence of intermixing phenomena. The measurement just described shows that the limiting factor at the lower temperature border is the transition to growth that is characterized by a less ordered surface (disappearing reconstruction). The next section describes, how kinetic growth manipulation (KGM) is applied attempting to finally reach Si films that are 1) smooth, 2) more ordered and 3).uninfluenced by intermixing.

5.3 Manipulated growth at 343 K

It is the aim to apply the growth manipulation method that has successfully been used for the growth of Si on Si(100) (see chapter 4) on the heteroepitaxial system of Si on Ge(100). The method consists of repeatedly growing an integer number of Si ML on Ge with a subsequent short flash. The sample temperature has to be as low as possible to avoid or at least minimize intermixing of Si and Ge. In the first place the sample base temperature that is used for the growth of the material is chosen as 343 K, the temperature that has been used for the conventional growth experiment shown in fig. 5.7. Secondly an appropriate sample temperature for the flash has to be determined. This will be done in the same way as for Si(100) homoepitaxy: Fig. 5.11 shows the real-time measurement of central diffraction spot intensities at five electron energies during the growth of three ML Si on Ge(100) and the subsequent annealing of the grown film.

As can be seen easily, the behaviour of the spot intensities is very different from what was measured on Si(100): Neither the intensity of the central spot at the out-of-phase like energy $11.3\sqrt{\text{eV}}$ nor those of the in-phase-like energies $8\sqrt{\text{eV}}$ and $12.4\sqrt{\text{eV}}$ increase significantly after the flashes, neither at the low nor in the medium temperature range (where intermixing is not significant yet). On the contrary, they decay even further. Only after reaching even higher flash temperatures of about 650 K the intensities go up; but it cannot be ruled out that this increase is due to intermixing. The STM study of Wulfhekel

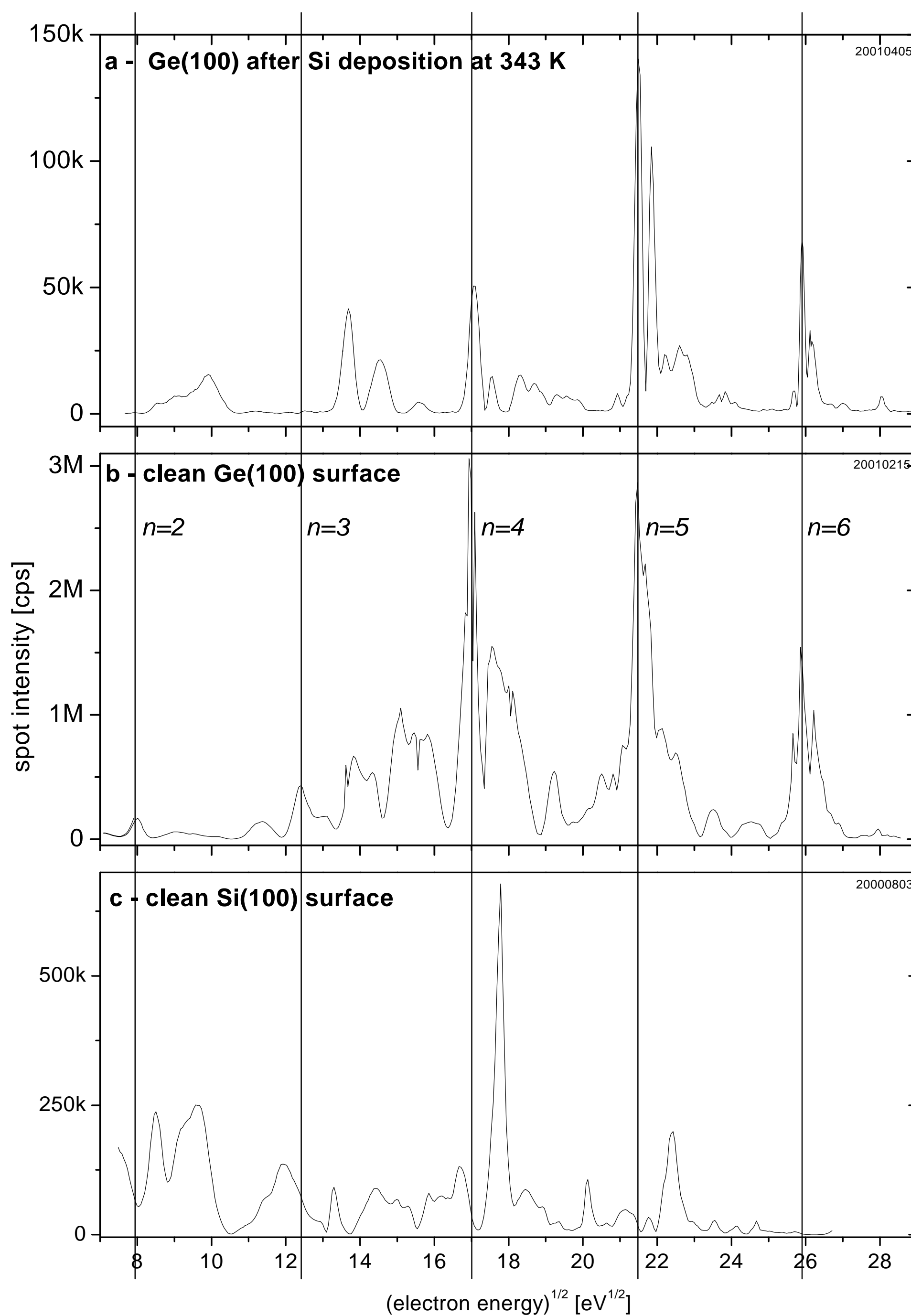

Figure 5.10: I/E curves of: (a) Ge(100) after conventional Si growth (approx. 8 ML at 343 K, see fig. 5.7). (b) clean Ge(100). (c) clean Si(100). All I/E curves were recorded at a sample temperature of 100 K. The vertical lines represent the in-phase conditions for clean Ge(100).

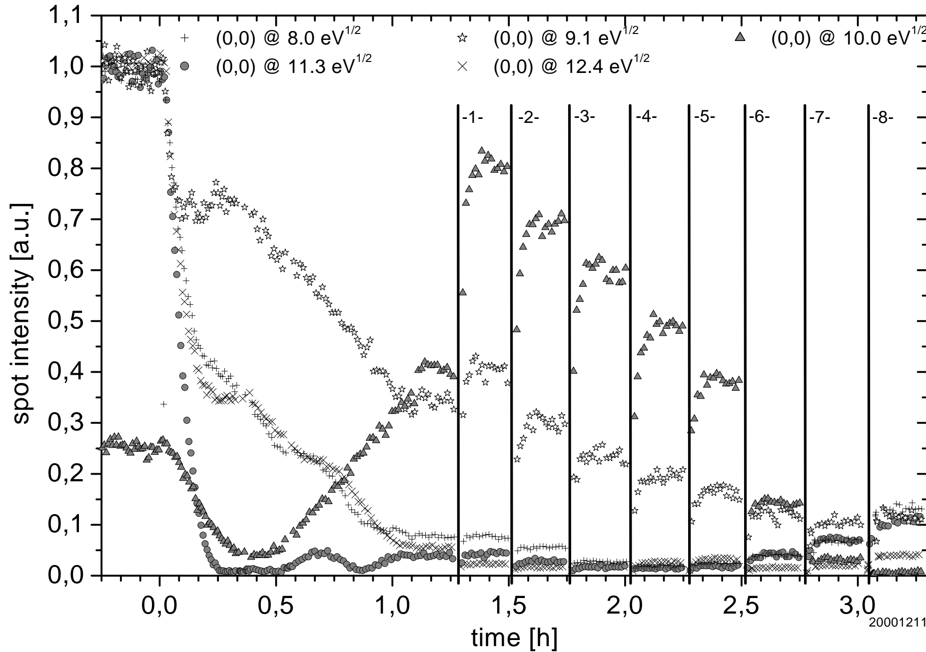

Figure 5.11: Successive annealing (flashes of 1 min) of 3ML of Si grown on Ge(100) at 345 K: -1- flash to 500 K, -2- 575 K, -3- 635 K, -4- 655 K, -5- 665 K, -6- 675 K, -7- 685 K, -8- 690 K

et al. shows very well that the surface gets smoother after the flashes. That's why it is quite astonishing that both the in-phase and the out-phase-like intensities more likely decrease than increase.

On the other hand, the intensities with the energies $9.1\sqrt{\mathrm{eV}}$ and $10.0\sqrt{\mathrm{eV}}$ do increase very well with the first flash (approx. 500K). The nature of these energies is, however, not clear as was already pointed out in section 5.2. During the in-situ deposition at 575 K (see fig. 5.1) the intensities of the energies $9.1\sqrt{\mathrm{eV}}$ and $10.0\sqrt{\mathrm{eV}}$ got stationary at a low level. From that one can deduce that for the intermixed situation the reflectivity of the sample is small. That would suggest that these energies can be used as a crude measure for the amount of intermixing[4]. The decrease of both intensities with increasing temperature would then indicate that 500 K is already a limiting temperature. Quite interesting is the drop in intensity at 675 K (6) a temperature close to the one found by Hoeven et al. for the onset of intermixing of Si and Ge(100). It would not be very convincing to base a decision for a flash temperature of about 500 K only on the experiment shown in fig. 5.11.

[4]In the sense that intermixing becomes more significant for flash temperatures above the temperature leading to an intensity maximum of the electron energies $9.1\sqrt{\mathrm{eV}}$ or $10.0\sqrt{\mathrm{eV}}$.

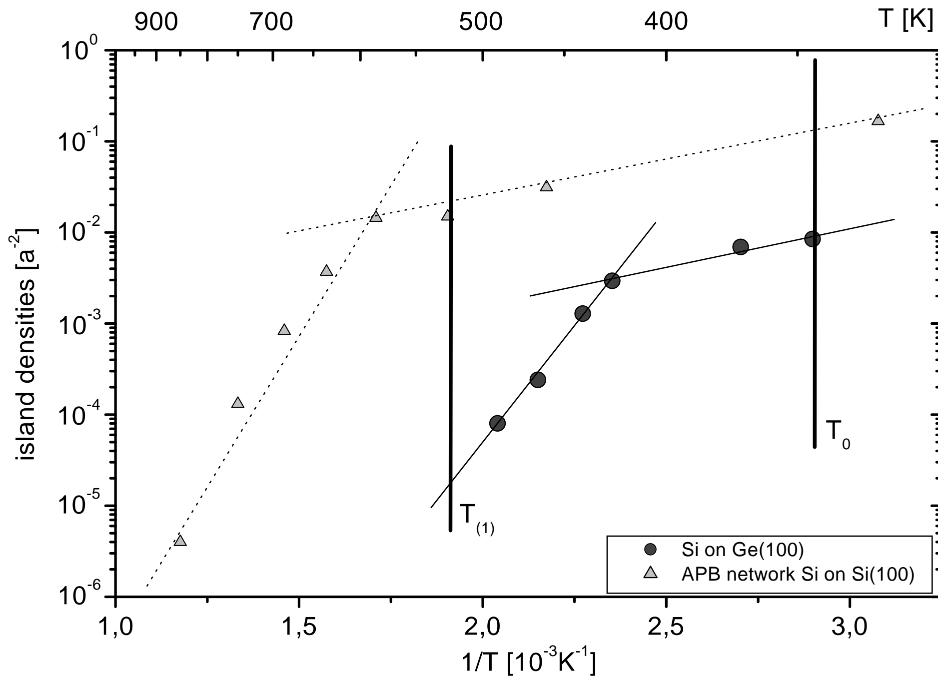

Figure 5.12: Si island densities on Ge(100) for conventional growth of 0.4ML Si vs. growth temperature. For comparison, the Si island densities on Si(100) (see fig. 4.1) are also drawn. T_0 is the base temperature, $T_{(1)}$ is the flash temperature for the manipulated growth experiment shown in fig. 5.13.

Similar to the examination performed for the growth of Si on Si(100) (see chapter 4) the island densities of Si films of 0.4 ML grown on Ge(100) at different temperatures in the range from 343 K to about 500 K have been determined by STM. As can be easily seen in fig. 5.12, the temperature above which island coarsening becomes active is at about 425 K. Following the KGM recipe outlined in chapter 4 an about 100 K higher temperature then the coarsening temperature should be used for the anneal step. Thus, flashing a film to 525 K should lead to APB densities and therefore island densities smaller by almost two orders of magnitude.

The described indications suggest to use 525 K as the flash temperature for the growth manipulation experiments monitored by real-time SPA-LEED measurements. Concerning intermixing 525 K is considered safe, because compared to the conventional growth experiment this temperature is not applied continuously but only during the flashes. That is a reduction by a factor of 15 in time (evaporation rate 4ML per hour). Wulfhekel et al. [WZH$^+$98, Wul97] have used exactly these two temperatures (343 K as base temperature, 525 K for the flashes) for their manipulated growth experiments that lead to the growth

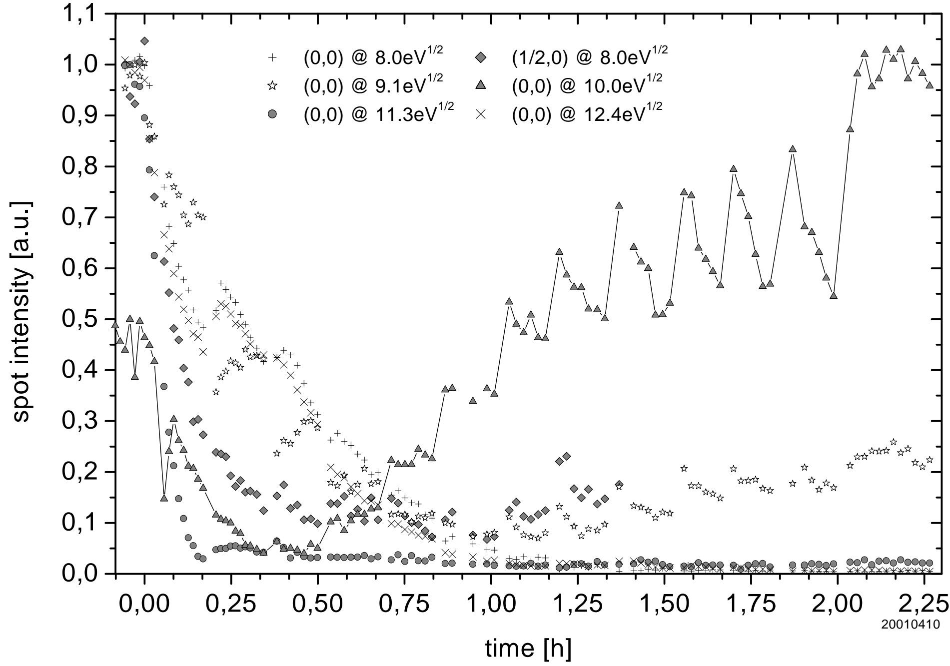

Figure 5.13: Real-time measurement of the central spot intensity at 5 phase conditions between the Ge bulk in-phase conditions $n = 2$ and $n = 3$ and half-order spot intensity during manipulated growth of about 8 ML Si on Ge(100) at 343 K. The evaporation is stopped before the last flash at 2h. The intensity values of the central spot at $10.0\sqrt{\text{eV}}$ (up-triangles) have been downscaled by a factor of two.

of smooth films.

Fig. 5.13 shows the normalized intensities of the central diffraction spot during the manipulated growth of about 8 ML Si on Ge(100) at 343 K (flash temperature 525 K), again at five electron energies between the in-phase conditions $n = 2$ and $n = 3$. Just as in the experiments described previously (see figs. 5.1,5.7), the intensity of one of the half-order spots has also been measured.

Comparing the real-time diffraction spot intensity measurements of conventional and manipulated Si growth (figs. 5.7 and 5.13), there is hardly any positive effect recognizable on the intensities of the central spot at the five different electron energies. The weak intensity oscillation at $11.3\sqrt{\text{eV}}$ has even vanished completely. The intensity of the $10.0\sqrt{\text{eV}}$ peak rises well after the flashes, but still this observation is hardly interpretable in a meaningful way, because the general behaviour of the spot intensity cannot be identified with either in-phase or out-of-phase, neither in conventional nor in manipulated growth. A different measure for the flatness of the film has to be taken into account.

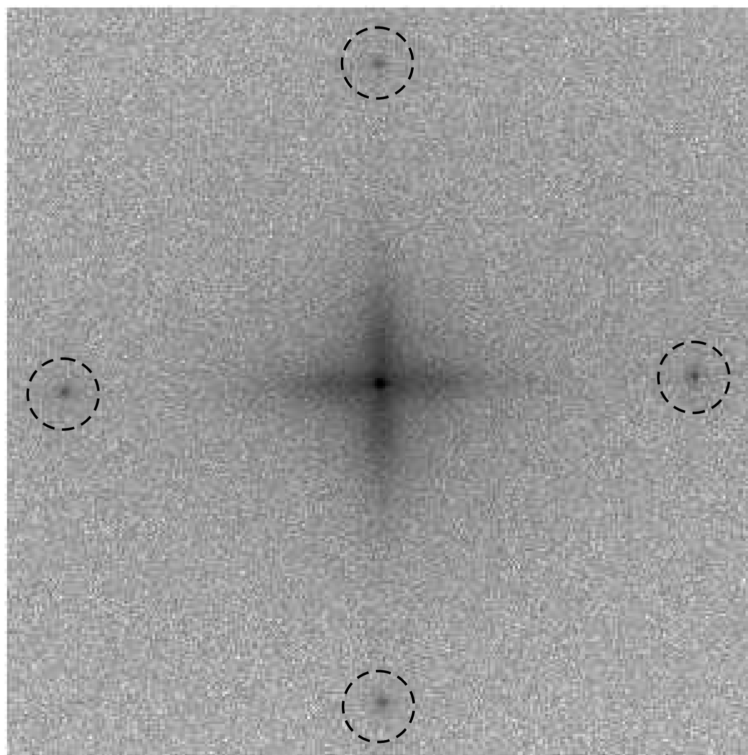

Figure 5.14: Two-dimensional intensity scan of the diffraction pattern of Ge(100) after the manipulated growth of Si (see fig. 5.13) around the central spot recorded at an electron energy of 460.3 eV and a sample temperature of 100 K. The half-order spots are present (markers). The spike of the central spot is surrounded by a four-fold diffuse part.

First of all, the intensity of the half-order spot profits from the kinetic growth manipulation: it stabilizes at about 15% of its initial value during the manipulated growth while the half-order spot vanished completely in the very initial phase of the conventional growth. One and two dimensional intensity scans of the diffraction pattern around the central spot (see figs. 5.14 and 5.15) taken after the experiment with the sample quenched to 100 K also demonstrate the presence of the half-order spots[5]. Thus, with the half-order spots clearly present it can be concluded that film growth occurs with improved surface ordering applying growth manipulation. This observation is supported by optical measurements that have been performed after the conventional and manipulated Si growth (see fig. 5.16). At the low photon energies, the absorption Imϵ_2 of the thin layer is lower

[5]The electron energy that was used for the recording of the intensity scans shown in figs. 5.14 and 5.15 is the energy at which the diffuse part around the central peak is most intense.

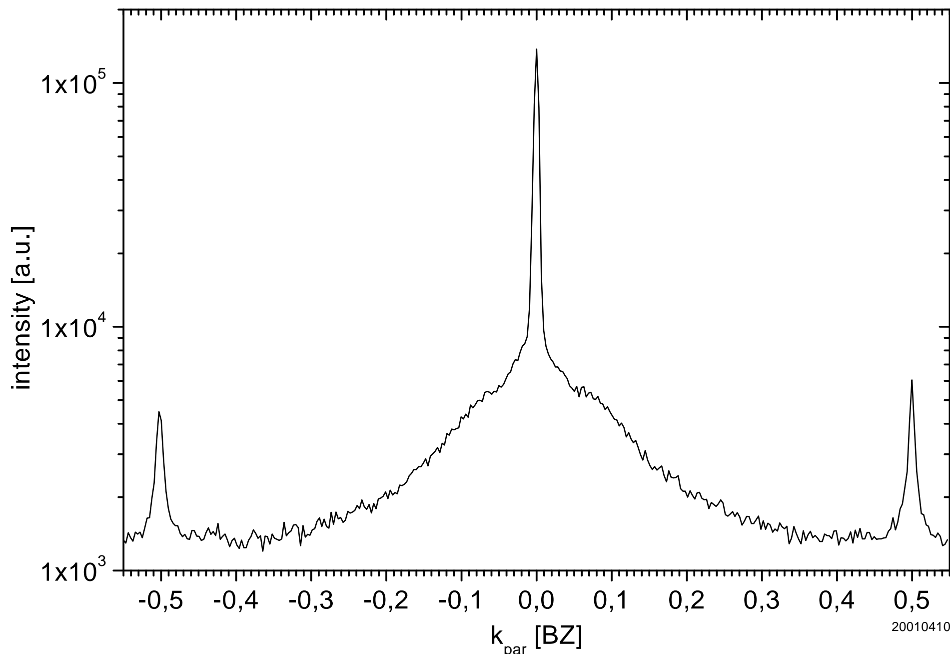

Figure 5.15: One-dimensional intensity scan of the diffraction pattern of Ge(100) after the manipulated growth of Si (see fig. 5.13) through the central spot and two half-order spots (horizontal cut in fig. 5.14) recorded at an electron energy of 460.3 eV and a sample temperature of 100 K.

after the manipulated growth. Although the result is rather noisy for the unmanipulated growth, absorption by silicon in this energy region is usually ascociated with amourphized silicon. The decrease of the optical absorption through growth manipulation would imply that growth only at the base temperature leads to a rather amorphous layer that through regular annealing is turned into a crystaline one. STM measurements indicate that at least the first layer growths epitaxial at the base temperature. The result would thus suggest a gradual change to an amorphous phase. An additional indication of a more crystaline phase of a manipulted film is the increased intensity around 3.4 eV, a so-called critical point of crystalline Si. The appearance of additional absorption at this energy would indicate that manipulation has improved the overall crystalline properties of the layer.

The I/E curves that were taken after conventional and manipulated growth are quite alike (see fig. 5.17): The positions of most of the peaks are identical. Only the intensities of the peaks are different. This clearly suggests that the Si layer grown has not intermixed, but shows the same properties as the low temperature deposited layer. The I/E curve is also different from that of a Ge or a Si surface, indicating that the electronic properties of

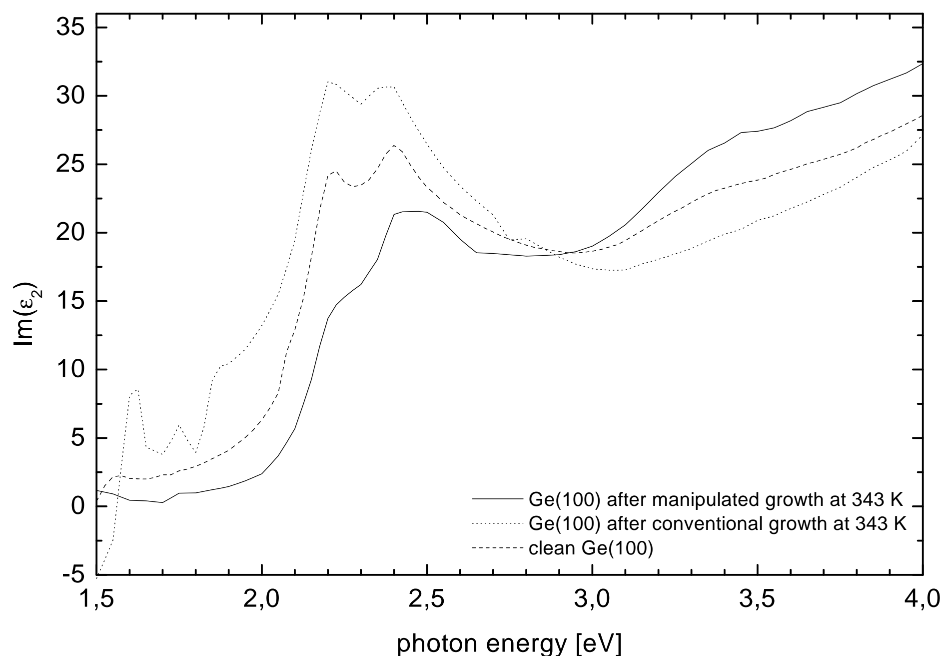

Figure 5.16: Ellipsometric optical absorption measurements after conventional and manipulated Si growth on Ge(100) at 343 K (see figs. 5.7 and 5.13). For comparison, the curve of the clean Ge(100) surface is also drawn. All measurements were taken at a sample temperature of 100 K.

this layer should be different from those bulk materials.

In conclusion, the experiments have shown that the system Si on Ge is even more sensitive to intermixing than has been reported previously. Although recently some intermixing in the first layer for submonolayer coverages of Si on Ge(100) has been reported, the work by Hoeven et al, which presented an intermixing temperature of 680 K, was regarded as a guide line. However, due to slow deposition rates, a temperature of 525 K was sufficient not only for intermixing of Si and Ge to a small degree, but also for a strong in-diffusion that left a top-layer of only 10% Si in a Ge matrix. Deposition at 343 K shows a very different picture of the layer grown. Both I/E and optical measurements show that a layer with electronic properties different from those of Ge and Si has been obtained. However, it is clear that this growth results in a rough layer. It is also evident from these measurements, that real-time LEED is very limited in its use for the present growth system. This is only partly due to heteroepitaxial growth, for which the in-phase and out-of-phase conditions will shift as a result of the changing interlattice spacing. Strong dynamic effects seem to take place also. This is not surprising, because it should be expected that the electronic

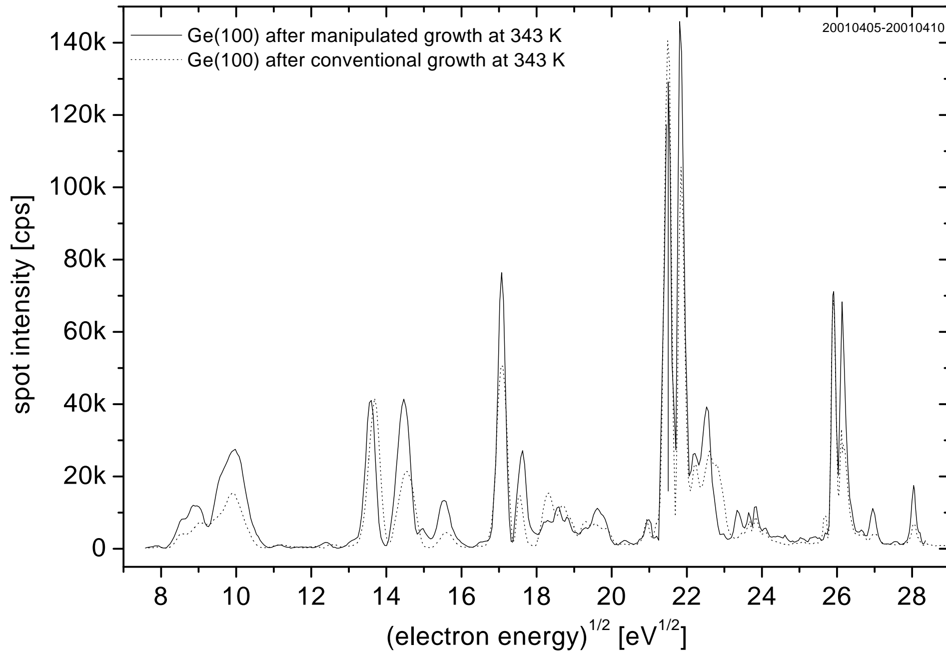

Figure 5.17: I/E curves of Ge(100) after manipulated and conventional Si growth at 343 K (approx. 8 ML, see figs. 5.7 and 5.13). The curves were recorded at a sample temperature of 100 K.

structure of the film changes with the thickness, which results in a strong thickness and electron energy dependent electron reflection. A thorough investigation on the annealing behaviour of a thin layer and the island density at sub-monolayer coverages made it possible to establish a coarsening temperature above which the APB network present in epitaxial growth on a reconstructed semiconductor surface enlarges dramatically. With this we could show that the temperatures taken by Wulfhekel in his KGM approach for Si on Ge(100) are exactly what they should be. From the results presented in this chapter it is clear that the annealing temperature cannot be higher, because intermixing will become significant. This will limit the smoothness of the Si layer grown. The electronic properties of the manipulated layer is quite like that measured at low temperatures (conventional growth), indicating that only very limited intermixing occurred.

Appendix A

WinSPA32

A.1 technical details

This section contains information only about the essential technical details of WinSPA32. See [Ess] for a more detailed description.

A.1.1 I/O hardware

The data acquisition computer is equipped with the following extensions:

1. Burr Brown PCI 20000 carrier board (ISA, part of the standard SPA-LEED equipment), with the following modules mounted:
    (a) two channel 16-bit DA converter module for the control of the SPA-LEED deflection plates
    (b) channeltron pulse counter for the intensity measurement of the diffracted electrons
2. two Keithley Metrabyte DAS-16 12bit ISA DA/AD boards with in total
    (a) 4 DA channels for the control of SPA-LEED electron energy, indirect sample heating filament current, direct sample heating current and evaporator current.
    (b) 16 AD channels to read the SPA-LEED electron energy setting and the analogue output signal of the UHV pressure meter
3. National Instruments GPIB interface card (ISA) to read an eight-channel Keithley scanner multimeter which is used to measure the following parameters: Pt100 sample temperature sensor, indirect sample heating filament current and voltage, sample current and voltage, evaporator current and voltage

Driver DLLs

WinSPA32 is equipped with a set of driver DLLs (DLL = dynamic link library) for the standard measuring hardware that has been used for the measurements described in this thesis. The decisive reason for the use of DLLs is the following: If the use of different measuring hardware should be necessary, only the driver DLLs have to be adapted/rewritten, while WinSPA32 itself stays unchanged. A DLL can be created with any development tool, it is completely independent from the rest of the software. The hardware driver routines are distributed over 3 DLLs (see A.2 for Delphi templates of the DLL's):

- DLL #1 contains the routines responsible for setting the SPA-LEED x and y deflection and reading the channeltron pulse counter
- DLL #2 contains the routines necessary for the SPA-LEED electron energy remote control
- DLL #3 contains the routines used for the remote control and input of all other experimental parameters

For the control of the Keithley Metrabyte DAS-16 boards the driver DLLs call some routines contained in the DLPORTIO.dll that can be downloaded from the ftp-server of Keithley

A.1.2 System requirements

With the standard measuring hardware driver DLL's WinSPA32 runs under the operating systems Microsoft Windows 9x/ME. If it is desired to run WinSPA32 under Microsoft Windows NT/2000, the hardware driver DLL's have to be adapted/rewritten. At least an Pentium processor with 166-200 MHz is recommended. At least 32 MB of internal memory are recommended. The screen resolution should not be lower than 1024x768, the color depth not lower than 16 bit.

A.2 source code hardware driver DLL # 1

```
{
(c) 2000 by Marcus Esser and the Solid State Physics Group
    of the University of Twente / Enschede / The Netherlands

this is the hardware driver DLL for the SPA-LEED
deflection plates and the electron counter.

library ProjectDLLhardwaredriver1;

uses
  SysUtils,
  Classes,
```

```
  UnitBurrBrown32Bit in '..\Units\UnitBurrBrown32Bit.pas', // for Burr Brown card only
  UnitMemAccess in '..\Units\UnitMemAccess.pas'; // for Burr Brown card only

var
  SaveExit: Pointer;  // pointer for exit procedure

// ---------------------------------------------------------------------------

// forward declaration block

// set y deflection DA to y[V, -150 to 150]
// return value 0 if errorfree
function HARDWAREsetYDA(y: single): integer; stdcall; forward;

// set x deflection DA to x[V, -150 to 150]
// return value 0 if errorfree
function HARDWAREsetXDA(x: single): integer; stdcall; forward;

// count electrons for gatetime[ms], result in frequency[counts]
// return value 0 if errorfree
function HARDWAREgetCounts(gatetime: integer; var frequency: double): integer; stdcall; forward;

// library exit procedure
procedure LibExit; forward;

// ---------------------------------------------------------------------------

function HARDWAREsetYDA(y: single): integer; stdcall;
var
     valuey, error: integer;
     i: integer;
begin
     // the following instructions are for the BurrBrown Card only
     valuey:= round(y/150*32767);
     error:= BBSetDA(1,valuey);
     HARDWAREsetYDA:= error;
end;

function HARDWAREsetXDA(x: single): integer; stdcall;
var
     valuex, error: integer;
begin
     // the following instructions are for the BurrBrown Card only
     valuex:= round(x/150*32767);
     error:= BBSetDA(0,valuex);
     HARDWAREsetXDA:= error;
end;

function HARDWAREgetCounts(gatetime: integer; var frequency: double): integer; stdcall;
var
     error: integer;
begin
     // the following instructions are for the BurrBrown Card only
     frequency:= 0;
     error:= BBgetCounts(gatetime,frequency);
     HARDWAREgetCounts:= error;
end;

//library exit procedure
procedure LibExit;
begin
     // instructions executed before the library exits can be entered here
end;

// ---------------------------------------------------------------------------

exports
     HARDWAREgetCounts,
     HARDWAREsetXDA,
     HARDWAREsetYDA;

// ---------------------------------------------------------------------------

// DLL initialisation code
begin
     // instructions to initialize the DLL can be entered here
```

```
     SaveExit:= ExitProc; //save exit procedure chain
     ExitProc:= @LibExit; //install LibExit as exit procedure
end.
// ----------------------------------------------------------------------------
```

A.3 source hardware driver DLL # 2

```
{
(c) 2000 by Marcus Esser and the Solid State Physics Group
    of the University of Twente / Enschede / The Netherlands

this is the hardware driver DLL for the SPA-LEED
electron energy.

library ProjectDLLhardwaredriver2;

uses
  SysUtils,
  Classes,
  UnitDas16pr32Bit in '..\Units\UnitDas16pr32Bit.pas', // only, if Das 16 card is used !
  Das16UnitHeadersDll in '..\Units\Das16UnitHeadersDll.pas'; // only, if Das 16 card is used !

var
  SaveExit: Pointer;  // pointer for exit procedure

// ----------------------------------------------------------------------------

// forward declaration block

// set electron energy to energy[eV]
// return value 0 if errorfree
function HARDWAREsetEnergy(energy: single): integer; stdcall; forward;

// library exit procedure
procedure LibExit; forward;

// ----------------------------------------------------------------------------

function HARDWAREsetEnergy(energy: single): integer; stdcall;
begin
     // the following instructions are for the Das16 Card only
     {$IFDEF energy}
     das16setDAvoltagecalibrated(0,energy/100);
     HARDWAREsetEnergy:=0;
     {$ENDIF energy}
end;

//library exit procedure
procedure LibExit;
begin
     // instructions executed before the library exits can be entered here
end;

// ----------------------------------------------------------------------------

exports
     HARDWAREsetEnergy;

// ----------------------------------------------------------------------------

// DLL initialisation code
begin
     // instructions to initialize the DLL can be entered here

     SaveExit:= ExitProc; //save exit procedure chain
     ExitProc:= @LibExit; //install LibExit as exit procedure
end.
// ----------------------------------------------------------------------------
```

Bibliography

[ABHM88] R. Altsinger, H. Busch, M. Horn, and Henzler M. *Surf. Sci.*, 200:235–246, 1988.

[AF94] J.G. Amar and F. Family. *Phys. Rev. B*, 50:8781, 1994.

[AF95] J.G. Amar and F. Family. *Phys. Rev. Lett.*, 74:2066, 1995.

[AKBB96] D. Aubel, L. Kubler, J.L. Bischoff, and D. Bolmont. *Surf. Sci.*, 352–354:634–640, 1996.

[BAN96] R.-P. Blum, D. Ahlberendt, and H. Niehus. *Surf. Sci.*, 366:107–120, 1996.

[Bau58] E. Bauer. *Z. Kristallogr.*, 110:372–431, 1958.

[BBRK95] H. Brune, K. Bromann, H. Röder, and K. Kern. *Phys. Rev. B*, 52(20):R14380–R14383, 1995.

[BC94] G.S. Bales and D.C. Chrzan. *Phys. Rev. B*, 50:6057, 1994.

[BE92] M.C. Bartelt and J.W. Evans. *Phys. Rev. B*, 46:12675, 1992.

[BE93] M.C. Bartelt and J.W. Evans. *Surf. Sci.*, 298:421, 1993.

[BFL+97] M. Bäumer, M. Frank, J. Libuda, S. Stempel, and H.-J. Freund. *Surf. Sci.*, 391:204–215, 1997.

[BKG97] B. Borovsky, M. Krueger, and E. Ganz. *Phys. Rev. Lett.*, 78(22):4229–4232, 1997.

[BL00] C.L. Berrie and S.R. Leone. *J. Cryst. Growth*, 216:159–170, 2000.

[BPR+95] P. Bedrossian, B. Poelsema, G. Rosenfeld, L.C. Jorritsma, N.N. Lipkin, and G. Comsa. *Surf. Sci.*, 334:1–9, 1995.

[Bro65] E.B. Brown. *Modern Optics*, chapter 4.48, page 178. Reinhold Publishing Corporation, 1965.

[BSE+01] K. Budde, J. Schimmelpfennig, M. Eichmann, W. Ernst, and H. Pfnür. *Surf. Sci.*, 473:71–85, 2001.

[Can98] Marco Cantu. *Mastering Delphi 4*, chapter 3, page 88. Sybex, Inc., 1998.

[CdRM+99] W.C.A.N. Ceelen, M. de Ridder, B. Moest, A.W. Denier van der Gon, and H.H. Brongersma. *Surf. Sci.*, 430:146–153, 1999.

[CDvdGR+98] W.C.A.N. Ceelen, A.W. Denier van der Gon, M.A. Reijme, H.H. Brongersma, I. Spolveri, A. Atrei, and U. Bardi. *Surf. Sci.*, 406:264–278, 1998.

[CMdR+98] W.C.A.N. Ceelen, B. Moest, M. de Ridder, L.J. van Ijzendoorn, A.W. Denier van der Gon, and H.H. Brongersma. *Appl. Surf. Sci.*, 134:87–94, 1998.

[Com95] G. Comsa. Lectures on crystal growth, university of bonn, 1995.

[CRKT89] M. Copel, M.C. Reuter, E. Kaxiras, and R.M. Tromp. *Phys. Rev. Lett.*, 63(6):632–635, 1989.

[CYTP92] R. Cao, X. Yang, J. Terry, and P. Pianetta. *Appl. Phys. Lett.*, 61(19):2347–2349, 1992.

[DBBK98] D. Dentel, J.L. Bischoff, D. Bolmont, and L. Kubler. *Surf. Sci.*, 402–404:304–307, 1998.

[DBKF99] D. Dentel, J.L. Bischoff, L. Kubler, and J. Faure. *J. of Crystal Growth*, 201/202:542–546, 1999.

[DFC+88] J.J. Demiguel, J. Ferron, A. Cebollada, J.M. Gallego, and S. Ferrer. *J. Crystal Growth*, 91:481, 1988.

[Dij00] S. van Dijken. PhD thesis, University of Twente, 2000. ISBN 90-365-1459-2.

[DMTY00] M. Degawa, H. Minoda, Y. Tanishiro, and K. Yagi. *Surf. Sci.*, 461:L528–L536, 2000.

[EFFL94] H.J. Ernst, F. Fabre, R. Folkerts, and J. Lapujoulade. *J. Vac. Sci. Techn. A*, 12:1809, 1994.

[EGC90] D.J. Eaglesham, H.J. Gossmann, and M. Cerullo. *Phys. Rev. Lett.*, 65(10):1227–1230, 1990.

[EH66] G. Ehrlich and F.G. Hudda. *J. Chem. Phys.*, 44:1039, 1966.

[EHMC94] S. Esch, M. Hohage, T. Michely, and G. Comsa. *Phys. Rev. Lett.*, 72(4):518–521, 1994.

[EHO+00] D. Eich, D. Hübner, K. Ortner, L. Kilian, R. Becker, G. Landwehr, R. Fink, and E. Umbach. *Appl. Surf. Sci.*, 166:12–16, 2000.

[EJ89] W.F. Egelhoff and I. Jacob. *Phys. Rev. Lett.*, page 921, 1989.

[EMRC98] M. Esser, K. Morgenstern, G. Rosenfeld, and G. Comsa. *Surf. Sci.*, 402–404:341–345, 1998.

[Ern97] H.J. Ernst. *Surf. Sci.*, 383:L755, 1997.

[Ess] M. Esser. http:\\www.spaleed.com – the spaleed website.

[EWP] M. Esser, H. Wormeester, and Bene Poelsema. to be published.

[EWP01] M. Esser, H. Wormeester, and B. Poelsema. *Surf. Sci.*, 2001. accepted for publication.

[GBBvB98] R. Gröger, A. Berlinger, M. Barczewski, and P. von Blanckenhagen. *Thin Solid Films*, 318:231–233, 1998.

[GBIS85] L.J. Gomez, S. Bourgeal, J. Ibanez, and M. Salmeron. *Phys. Rev. B*, 31:2551, 1985.

[GH82] K.D. Gronwald and M. Henzler. *Surf. Sci.*, 117:180, 1982.

[GMG+00] M. Gierer, A. Mikkelsen, M. Gräber, P. Gille, and W. Moritz. *Surf. Sci.*, 463:L654–L660, 2000.

[GMT99] M.E. Gonzalez-Mendez and N. Takeuchi. *Surf. Sci. Lett.*, 441:L897–L903, 1999.

[GvB96] R. Gröger and P. von Blanckenhagen. *Thin Solid Films*, 281-282:73–75, 1996.

[HAL89] A.J. Hoeven, J. Aarts, and P.K. Larsen. *J. Vac. Sci. Technol. A*, 7(1):5–8, 1989.

[HD90] U.K. Hamers, R.J. Köhler and J.E. Demuth. *J. Vac. Sci. Technol. A*, 8(1):195–200, 1990.

[HDLD89] Lenssink J.M. Hoeven, A.J., D. Dijkkamp, E.J. van Loenen, and J. Dieleman. *Phys. Rev. Lett.*, 63(17):1830–1832, 1989.

[Hen85] M. Henzler. *Surf. Sci.*, 152/153:963, 1985.

[Hen88] M. Henzler. In F. van der Veen and M.A. van Hoeve, editors, *Structure of Surfaces*, volume II of *Springer Series in Surface Science*. Springer, 1988.

[Hen96] M. Henzler. *Surf. Sci.*, 357–358:809–819, 1996.

[HGH88] M. Horn, U. Gotter, and M. Henzler. *J. Vac. Sci. Technol. B*, 6(2):727–730, 1988.

[HKOS00] K. Hata, T. Kimura, S. Ozawa, and H. Shigekawa. *J. Vac. Sci. Technol. A*, 18(4):1933, 2000.

[HMzHZHvH00] R. Hild, F.-J. Meyer zu Heringdorf, P. Zahl, and M. Horn-von Hoegen. *Surf. Sci.*, 454–456:851–855, 2000.

[Hoe90] A.J. Hoeven. PhD thesis, University of Leiden, 1990.

[HPL+99] M. Henzler, O. Pfennigtorf, K. Lang, T. Lüer, F. Moresco, and T. Hildebrandt. *Surf. Sci.*, 438:178–184, 1999.

[HvH99] M. Horn-von Hoegen. *Z. Kristallogr.*, 214:1–75, 1999.

[IGWM99] A. Iglesias, M. Gierer, D. Wolf, and W. Moritz. *Surf. Sci.*, 442:357–373, 1999.

[Jor97] L.C. Jorritsma. PhD thesis, University of Twente, 1997. ISBN 90-365-1021-1.

[KBG97] M. Krueger, B. Borovsky, and E. Ganz. *Surf. Sci.*, 385:146–154, 1997.

[KDH89] U. Köhler, J.E. Demuth, and R.J. Hamers. *J. Vac. Sci. Technol. A*, 7:286, 1989.

[KF86] M.V. Klein and T.E. Furtak. *Optics*, chapter 4.3, pages 222–256. John Wiley and Sons, Inc., 1986.

[KG94] D.D. Koleske and S.M. Gates. *J. Appl. Phys.*, 76(3):1615–1621, 1994.

[KJW+00] U. Köhler, C. Jensen, C. Wolf, A.C. Schindler, L. Brendel, and D.E. Wolf. *Surf. Sci.*, 454–456:676–680, 2000.

[KPVC90] R. Kunkel, B. Poelsema, L.K. Verheij, and G. Comsa. *Phys. Rev. Lett.*, 65:733, 1990.

[KSLW93] N. Kitamura, B.S. Swartzentruber, M.G. Lagally, and M.B. Webb. *Phys. Rev. B*, 48(8):5704–5707, 1993.

[KT89] P.C. Kelires and J. Tersoff. *Phys. Rev. Lett.*, 63(11):1164–1167, 1989.

[KUT89] H. Kawataba, H. Ueba, and C. Tatsuyama. *J. Appl. Phys.*, 66(2):634–639, 1989.

[KY89] H. Kahata and K. Yagi. *Jap. J. of Appl. Phys.*, 28(5):L858–L861, 1989.

[LAKS89] A.V. Latyshev, A.L. Aseev, A.B. Krasilnikow, and S.I. Stenin. *Surface Science*, 213:157–169, 1989.

[LFS+97] J. Libuda, M. Frank, A. Sandell, S. Andersson, P.A. Brühweiler, M. Bäumer, N. Martensson, and H.-J. Freund. *Surf. Sci.*, 384:106–119, 1997.

[LMC92] D.S. Lin, T. Miller, and T.C. Chiang. *Phys. Rev. B*, 45(19):11415–11418, 1992.

[LWWM96] A.H. Levermann, D.A. Woolf, D.I. Westwood, and J.E. Macdonald. *Surf. Sci.*, 352–354:812–816, 1996.

[MFL+96] J.R. Mercer, P. Finetti, F.M. Leibsle, R. McGrath, V.R. Dhanak, A Baraldi, K.C. Prince, and R. Rosei. *Surf. Sci.*, 352–354:173–178, 1996.

[MKWL91] Y.W. Mo, J. Kleiner, M.B. Webb, and M.G. Lagally. *Phys. Rev. Lett.*, 66(15):1998–2001, 1991. see also [PVW92].

[MPS+91] V.A. Markov, O.P. Pchelyakov, L.V. Sokolov, S.I. Stenin, and S. Stoyanov. *Surf. Sci.*, 250:229–234, 1991.

[MRHH00] F. Moresco, M. Rocca, T. Hildebrandt, and M. Henzler. *Surf. Sci.*, 463:22–28, 2000.

[MRZH99] F. Moresco, Hildebrandt-T. Rocca, M. and, V. Zielasek, and M. Henzler. *Surf. Sci.*, 424:62–73, 1999.

[MSH97] B.H. Müller, Th. Schmidt, and M. Henzler. *Surf. Sci.*, 376:123–132, 1997.

[MSK+89] Y.W. Mo, B.S. Swartzentruber, R. Kariotis, M.B. Webb, and M.G. Lagally. *Phys. Rev. Lett.*, 63(21):2393–2396, 1989.

[MSSL90] Y.W. Mo, D.E. Savage, B.S. Swartzentruber, and M.G. Lagally. *Phys. Rev. Lett.*, 65(8):1020–1023, 1990.

[MSY+00] H. Minoda, T. Shimakura, K. Yagi, F.-J. Meyer zu Heringdorf, and M Horn-von Hoegen. *Phys. Rev. B*, 61(8):5672–5678, 2000.

[MYMzH+99] H. Minoda, K. Yagi, F.-J. Meyer zu Heringdorf, A. Meier, D. Kähler, and M Horn-von Hoegen. *Phys. Rev. B*, 59(3):2363–2375, 1999.

[MzHGG+00] F.-J. Meyer zu Heringdorf, H. Goldbach, H.-L. Günter, M. Horn-von Hoegen, V. Dorna, U. Köhler, and M. Henzler. *Surf. Sci.*, 458:147–154, 2000.

[MZVHvH98] A. Meier, P. Zahl, R. Vockenroth, and M. Horn-von Hoegen. *Appl. Surf. Sci.*, 123/124:694–698, 1998.

[Nic66] F.A. Nichols. *J. Appl. Phys.*, 37:2805, 1966.

[NJPN83] J.H. Neave, B.A. Joyce, Dobson P.J., and N. Norton. *Appl. Phys. A*, 31:1–8, 1983.

[NKE93] G.L. Nyberg, M.T. Kief, and W.F. Egelhoff. *Phys. Rev. B.*, 48:14509, 1993.

[NM65a] F.A. Nichols and W.W. Mullins. *Trans. Metall Soc. AIME*, 233:1840, 1965.

[NM65b] F.A. Nichols and W.W. Mullins. *J. Appl. Phys.*, 36:1826, 1965.

[NMF+97] L. Nedelmann, B. Müller, B. Fischer, K. Kern, D. Erdös, J. Wollschläger, and M. Henzler. *Surf. Sci.*, 376:113–122, 1997.

[NSS+97] H. Neureiter, S. Spranger, M. Schneider, U. Winkler, M. Solokowski, and E. Umbach. *Surf. Sci.*, 388:186–200, 1997.

[PBK+95] C. Pearson, B. Borovsky, M. Krueger, R. Curtis, and E. Ganz. *Phys. Rev. Lett.*, 74(14):2710–2713, 1995.

[PBR+92] B. Poelsema, A.F. Becker, G. Rosenfeld, R. Kunkel, N. Nagel, L.K. Verheij, and G. Comsa. *Surf. Sci.*, 272:269, 1992.

[PC] B. Poelsema and G. Comsa. *Scattering of Thermal Energy Atoms from Disordered Surfaces*. Springer.

[PFTV86] W.H. Press, B.P. Flannery, S.A. Teukolsky, and W.T. Vetterling. *Numerical Recipes*, chapter 14.4, pages 521–528. Cambridge University Press, 1986.

[PKMW97] H. Pietsch, A. Klust, A. Meier, and J. Wollschläger. *Surf. Sci.*, 377-379:909–913, 1997.

[PVC84] B. Poelsema, L.K. Verheij, and G. Comsa. *Phys. Rev. Lett.*, 53:2500, 1984.

[PVW92] A. Pimpinelli, J. Villain, and D.E. Wolf. *Phys. Rev. Lett.*, 69(6):985, 1992. comment on [MKWL91].

[QSL00] X.R. Qin, B.S. Swartzentruber, and M.G. Lagally. *Phys. Rev. Lett.*, 84(20):4645–4648, 2000.

[RLW+95] G. Rosenfeld, N.N. Lipkin, W. Wulfhekel, J. Kliewer, K. Morgenstern, B. Poelsema, and G. Comsa. *Appl. Phys. A*, 61:455, 1995.

[Rob98] I.K. Robinson. *Acta Cryst. A*, 54:772, 1998.

[RPC95] G. Rosenfeld, B. Poelsema, and G. Comsa. *J. Cryst. Growth*, 151:230–233, 1995.

[RPLV98] I.K. Robinson, J.A. Pitney, J.L. Libbert, and I.A. Vartanyants. *Physica B*, 248:387, 1998.

[RST+93] G. Rosenfeld, R. Servaty, C. Teichert, B. Poelsema, and G. Comsa. *Phys. Rev. Lett.*, 71:895–898, 1993.

[SC00] M. Sotto and B. Croset. *Surf. Sci.*, 461:78–86, 2000.

[SESK98] C. Schmidthals, A. Enders, D. Sander, and J. Kirschner. *Surf. Sci.*, 402–404:636–640, 1998.

[SLI+00] A.A. Saranin, V.G. Lifshits, K.V. Ignatovich, H. Bethge, R. Kayser, H. Goldbach, A. Klust, J. Wollschläger, and M. Henzler. *Surf. Sci.*, 448:87–92, 2000.

[SMH86] U. Scheithauer, G. Meyer, and M. Henzler. *Surf. Sci.*, 178:441, 1986.

[SMWL89] B.S. Swartzentruber, Y.-W. Mo, M.B. Webb, and M.G. Lagally. *J. Vac. Sci. Technol. A*, 7(4):2901, 1989.

[SS66] R.L. Schwoebel and E.J. Shipsey. *J. Appl. Phys.*, 37:3682, 1966.

[Sto90] S. Stoyanov. *Jap. J. of Appl. Phys.*, 29(4):L659–L662, 1990.

[Swa96] B.S. Swartzentruber. *Phys. Rev. Lett.*, 76(3):459–462, 1996.

[TXK+94] R. Tsu, H.Z. Xiao, Y.-W. Kim, M.-A. Hasan, H.K. Birnbaum, J.E. Greene, D.S. Lin, and T.-C. Chiang. *J. Appl. Phys.*, 75(1):240–247, 1994.

[UDYJ97] V.A. Ukraintsev, Z. Dohnalek, and J.T. Yates Jr. *Surf. Sci.*, 388:132, 1997.

[vDJP99] S. van Dijken, L.C. Jorritsma, and B. Poelsema. *Phys. Rev. Lett.*, 82:4038, 1999.

[vdVVBV98] H.A. van der Vegt, J. Vrijmoeth, R.J. Behm, and E. Vlieg. *Phys. Rev. B*, 57:4127, 1998.

[Ven73] J.A. Venables. *Phil. Mag.*, 27:697, 1973.

[VLvdV95] E. Vlieg, M. Lohmeier, and H.A. van der Vegt. *Nucl. Instrum. Meth. B*, 97:358, 1995.

[VSH84] J.A. Venables, G.D.T. Spiller, and M. Hanbrücken. *Rep. Progr. Phys.*, 47:399, 1984.

[vSLZ+92] R.G. van Silfhout, M. Lohmeier, S. Zaima, J.F. van der Veen, P.B. Howes, C. Norris, J.M.C. Thornton, and A.A. Williams. *Surf. Sci.*, 271:32, 1992.

[vSvdVFN92] R.G. van Silfhout, J.F. van der Veen, S. Ferrer, and C. Norris. *Surf. Sci*, 264:281, 1992.

[WBR+98] W. Wulfhekel, I. Beckmann, G. Rosenfeld, B. Poelsema, and G. Comsa. *Surf. Sci.*, 395:168, 1998.

[WCZL95] Fang Wu, Xun Chen, Zhenyu Zhang, and M.G. Lagally. *Phys. Rev. Lett.*, 74(4):574–577, 1995.

[Wen96] D.J. Wentink. PhD thesis, University of Twente, 1996. ISBN 90-9009872-0.

[WES98] J. Wollschläger, D. Erdös, and K.-M. Schröder. *Surf. Sci.*, 402–404:272–276, 1998.

[WHZ+97] W. Wulfhekel, B.J. Hattink, H.J.W. Zandvliet, G. Rosenfeld, and B. Poelsema. *Phys. Rev. Lett.*, 79(13):2494–2497, 1997.

[WKWvS97] D.J. Wentink, M. Kuijper, H. Wormeester, and A. van Silfhout. *Phys. Rev. B*, 56(12):7679–7686, 1997.

[WM96] J. Wollschläger and A. Meier. *Appl. Surf. Sci.*, 104/105:392–401, 1996.

[Wul97] W. Wulfhekel. PhD thesis, University of Twente, 1997. ISSN 0944-2952.

[WVT+99] J. Wollschläger, J. Viernow, C. Tegenkamp, D. Erdös, K.M. Schröder, and H. Pfnür. *Appl. Surf. Sci.*, 142:129–134, 1999.

[WZH+98] W. Wulfhekel, H.J.W. Zandvliet, B.J. Hattink, G. Rosenfeld, G. Comsa, and B. Poelsema. *Phys. Rev. B*, 58(23):15359–15362, 1998.

[XZM+94] M.H. Xie, J. Zhang, S.M. Mokler, J. Fernandez, and B.A. Joyce. *Surf. Sci.*, 320:259–270, 1994.

[YWV+93] T. Yokotsuka, M.R. Wilby, D.D. Vvedensky, T. Kawamura, K. Fukutani, and S. Ino. *Appl. Phys. Lett.*, 62(14):1673–1675, 1993.

[YY93] H. Yamaguchi and K. Yagi. *Surf. Sci.*, 287/288:820–825, 1993.

[Zan00] H.J.W. Zandvliet. *Review of Modern Physics*, 72(2):593–602, 2000.

[ZEvL92] H.J.W. Zandvliet, H.B. Elswijk, and E.J. van Loenen. *Surf. Sci.*, 272:264–268, 1992.

[Zoe01] E. Zoethout. PhD thesis, University of Twente, 2001. ISBN 90-365-1633-1.

[ZW97] J.K. Zuo and J.F. Wendelken. *Phys. Rev. Lett.*, 78:2791, 1997.

[ZWDC94] J.K. Zuo, J.F. Wendelken, H. Durr, and Liu C.L. *Phys. Rev. Lett.*, 72, 1994. 3064.

[ZZWP01] H.J.W. Zandvliet, E. Zoethout, W. Wulfhekel, and Bene Poelsema. accepted for publication, 2001.

Summary

In this thesis, a study of the growth of silicon on Si(111), Si(100) and Ge(100) surfaces has been presented. Spot Profile Analysis Low Energy Electron Diffraction (SPA-LEED) has been used as a real-time in-situ probe for the surface morphology next to scanning tunneling microscopy (STM). The extended use of the SPA-LEED technique has required the development of improved experimental control software. The new software in combination with the implementation of the remote control of the electron energy and other key experimental parameters allows the reliable automatic measurement of diffraction pattern intensities in real-time. During an experiment, the spike intensities or linescans through various spots even at different phase conditions can be recorded intermittently. I/E curves can be recorded automatically with high point resolution. This advanced control enables not only a thorough study with in-situ electron diffraction, but also helps to identify the nature of low energy electron studies.

For homoepitaxy of Si(111), possibilities and limitations of the SPA-LEED technique for real-time in-situ analysis are discussed. The problem of the validity of the kinematic approximation in LEED has been revisited. In particular, the dispute on its applicability for the purpose of obtaining quantitative information from the analysis of spot shapes in high-resolution LEED (SPA-LEED) has been aggravated. The data on the homoepitaxial growth of Si(111) that have been presented suggest that dynamic features could be important also for the analysis of disordered systems even in a small range of scattering vector changes. The useful approach, suggested by Henzler, in which the atomic scattering factors are replaced by effective atomic scattering factors related to columns below a particular surface unit cell has been followed. The observations on the behaviour of the in-phase spot height during growth imply that the atomic scattering factors positioned on, or near to, defect sites deviate from those centred in ideal environments in flat terraces. At this point it is concluded that it is unlikely that just a deviation from the scattering position of the step atoms from their bulk positions could explain these results. However, to really nail down the importance of dynamic effects in SPA-LEED analysis one should study kinetic roughening of surfaces, which show no inherent tendency for reconstruction. The findings presented here urge caution when trying to obtain information on the vertical distribution

of exposed bilayers from the energy dependence of the height of the central spot in the spatial distribution near a Bragg position.

For the homoepitaxy of Si(100), a kinetic growth manipulation (KGM) method that aims at the manipulation of the density of the anti-phase boundary (APB) network that forms during growth on the reconstructed Si(100) surface has been developed. The KGM method makes use of the fact that above the coarsening temperature of about 560-600 K the density of the APB network depends strongly on the temperature. It has been demonstrated that this KGM method can be used successfully to prevent progressive roughening of the growth front during homoepitaxy of Si(100). As a consequence, films with a thickness of many ML can be grown in a flat and smooth manner. Furthermore it has been shown, that growth manipulation methods like the concept of two mobilities that work successfully against the additional energy barrier at the island edges for downward diffusion in epitaxy of unreconstructed metal surfaces are not successful in preventing the progressive roughening of the growth front in the case of the reconstructed Si(100) surface.

For the growth system Si on Ge(100), experiments have shown that it is even more sensitive to intermixing than has been reported previously. Although recently some intermixing in the first layer for submonolayer coverages of Si on Ge(100) has been reported, the work by Hoeven et al, which presented an intermixing temperature of 680 K, was regarded as a guide line. However, due to slow deposition rates, a temperature of 525 K was sufficient not only for intermixing of Si and Ge to a small degree, but also for a strong in-diffusion that left a top-layer of only 10% Si in a Ge matrix. Deposition at 343 K shows a very different picture of the layer grown. Both I/E and optical measurements show that a layer with electronic properties different from those of Ge and Si has been obtained. However, growth at this temperature results in a rough layer. It is also evident from these measurements, that real-time LEED is very limited in its use for the present growth system. This is only partly due to heteroepitaxial growth, for which the in-phase and out-of-phase conditions will shift as a result of the changing interlattice spacing. Strong dynamic effects seem to take place also. This is not surprising, because it should be expected that the electronic structure of the film changes with the thickness, which results in a strong thickness and electron energy dependent electron reflection. A thorough investigation on the annealing behaviour of a thin layer and the island density at sub-monolayer coverages made it possible to establish a coarsening temperature above which the APB network present in epitaxial growth on reconstructed Si(100) and Ge(100) surface enlarges dramatically. With this we could show that the temperatures taken by Wulfhekel in his KGM approach for Si on Ge(100) are exactly what they should be. From the results presented in this chapter it is clear that the annealing temperature cannot be higher, because intermixing will become significant. This will limit the smoothness of the Si layer grown. The electronic properties

of the manipulated layer are quite like that measured at low temperatures (conventional growth), indicating that only very limited intermixing occurred.

Samenvatting

In dit proefschrift met de titel 'Kinetisch gecontroleerde Si-epitaxie op Si(100) en Ge(100)' is onderzoek verricht naar de groei van silicium op Si(111), Si(100) en Ge(100) oppervlaktes. Spot Profile Analysis Low Energy Electron Diffraction (SPA-LEED) is gebruikt als een real-time in-situ techniek voor de verkenning van de oppervlaktemorfologie (naast raster tunneling microscopie). Om de mogelijkheden van de SPA-LEED techniek ten volle te benutten, is de ontwikkeling van verbeterde software voor de besturing van de experimenten vereist. De combinatie van nieuwe software met de implementatie van afstandsbesturing van de elektronenenergie en andere belangrijke experimentele parameters, staan betrouwbare geautomatiseerde metingen toe van de intensiteit van diffractiepatronen in real-time. Gedurende een experiment kunnen de piek-intensiteiten van line-scans van verschillende spots zelfs bij verschillende fase condities afzonderlijk opgeslagen worden. I/E krommes kunnen automatisch met hoge punt resolutie opgeslagen worden. Deze geavanceerde manier van besturing maakt het niet alleen mogelijk in-situ elektronen diffractie te bestuderen, maar het helpt ook de eigenschappen van lage energie elektronen diffractie te bestuderen.

De mogelijkheden en beperkingen van de SPA-LEED techniek worden voor real-time in-situ analyse van de homoepitaxie op Si(111) besproken. Het probleem van de geldigheid van de kinematische benadering in LEED wordt opnieuw bekeken. Specifiek wordt de discussie over de toepasbaarheid van het verkrijgen van kwantitatieve informatie, afkomstig van spot-vorm-analyse in hoge resolutie LEED, weer geopend. De data van de homoepitaxiale groei experimenten op Si(111) suggereert dat dynamische effecten ook voor de analyse van verstoorde systemen, zelfs in een klein veranderingsbereik van de verstrooiingsvector, belangrijk kunnen zijn. De benadering van Henzler, waarin de atomaire verstrooiingsfactoren vervangen zijn door effectieve atomaire verstrooiingsfactoren, gerelateerd aan kolommen onder een specifieke oppervlakte-eenheidscel, wordt gehanteerd. De observaties van het gedrag van in-fase spot-hoogtes gedurende groei impliceren dat atomaire verstrooiingsfactoren, gepositioneerd op of dichtbij foutlocaties, afwijken van diegene die gecentreerd zijn in ideale omgevingen in vlakke terrassen. Het is onwaarschijnlijk dat deze resultaten verklaard kunnen worden met alleen een afwijking van de verstrooiingspositie van de randatomen ten opzichte van hun bulk posities. Om het belang van dynamische effecten in

de SPA-LEED analyse vast te leggen, moet men de kinetische verruwing van oppervlaktes, die geen inherente tendens voor reconstructie laten zien, bestuderen. De gepresenteerde resultaten vragen grote voorzichtigheid; met name wanneer men informatie probeert te verkrijgen over de verticale verdeling van blootgestelde dubbellagen uit de energieafhankelijkheid van de hoogte van de centrale spot in de ruimtelijke verdeling in de buurt van een Bragg-positie.

Een kinetische groei manipulatie methode (KGM) is ontwikkeld voor de homoepitaxie van Si(100). Deze richt zich op de manipulatie van de dichtheid van het anti-fase grenzen (APB) netwerk, die wordt opgebouwd op de gereconstrueerde Si(100) oppervlaktes. De KGM methode maakt gebruik van het feit dat boven een coarsening temperatuur van rond 560-600 K de dichtheid van het APB-netwerk sterk van de temperatuur afhangt. Aangetoond wordt dat deze KGM methode succesvol kan worden toegepast om progressieve verruwing van het groeifront tijdens homoepitaxie op Si(100) te voorkomen. Het gevolg is, dat films met een dikte van vele monolagen op een vlakke en gladde manier kunnen worden geproduceerd. Verder wordt aangetoond dat groei manipulatie methodes, zoals het concept of two mobilities (overwint de energiebarrire aan de eilanden randen die diffusie over deze randen heen kan voorkomen; werkt succesvol voor epitaxie op ongereconstrueerde metaaloppervlaktes) niet succesvol zijn in het voorkomen van progressieve verruwing van het groeifront in het geval van het gereconstrueerde Si(100) oppervlak.

Experimenten laten zien, dat het groeisysteem Si op Ge(100) nog gevoeliger is voor intermixing dan eerder gepubliceerd is. Hoewel onlangs over intermixing in de bovenste laag bij sub-monolagen bedekking in het geval van groei van Si op Ge(100) is gerapporteerd, wordt de publicatie van Hoeven et al., die liet zien dat bij temperaturen van 680 K intermixing optreedt, als een rode draad gebruikt. Als gevolg van lage depositiesnelheden is een temperatuur van 525 K voldoende niet alleen voor het intermixing van Si en Ge op kleine schaal, maar ook voor een sterke in-diffusie dat een toplaag van slechts 10 % Si achterlaat in een Ge-matrix. Depositie bij 343 K laat een heel ander plaatje zien van de gegroeide lagen. Zowel I/E krommes als optische metingen laten zien dat een laag met elektronische eigenschappen anders dan die van Si en Ge ontstaan is. Toch resulteert groei bij deze temperatuur in een ruwe laag. Uit deze metingen wordt duidelijk dat real-time LEED een gelimiteerd methode is bij onderzoek van dit groeisysteem. Dit is alleen gedeeltelijk het gevolg van heteroepitaxiale groei, waarin de in- en uit-fase condities verschoven zijn als gevolg van de veranderde interlagen afstand. Sterke dynamische effecten spelen blijkbaar ook een rol. Dit is geen verrassing, omdat verwacht kan worden, dat de elektronische structuur van de film verandert met de laagdikte, resulterend in een sterke dikte- en elektronenenergieafhankelijke elektronenreflectie. Diepgaand onderzoek over het verwarmingsgedrag van een dunne laag en de eilanddichtheid bij sub-monolagenbedekkingen heeft

het mogelijk gemaakt, om een coarseningtemperatuur te bepalen. Boven deze coarseningtemperatuur neemt de dichtheid van het APB netwerk, dat op gereconstrueerde Si(100) en Ge(100) oppervlaktes ontstaat, sterk met de temperatuur toe. Hieruit blijkt, dat de temperaturen, die Wulfhekel in zijn KGM benadering gemeten heeft, juist zijn. Uit deze resultaten blijkt, dat de verwarmingstemperatuur niet hoger kan zijn, omdat dan intermixing significant wordt. Dit zal de gladheid van de groei van de Si laag beperken. De elektronische eigenschappen van de gemanipuleerde laag zijn vergelijkbaar met die gemeten bij lagere temperaturen (conventionele groei). Dit wijst erop, dat alleen zeer beperkte intermixing optreedt.

Acknowledgements

Now, at the end of the research periode for my PhD thesis I want to express my thanks to several people that have contributed to the thesis' development.

First of all, I want to thank my promotor Bene Poelsema for giving me the possibility to perform the PhD study in his research group and his fatherly care for the project and me. I am grateful to my co-promotor Herbert Wormeester for his guiding support and his inexhaustible ideas concerning experiments and physics. I express gratitude to Harold Zandvliet for sharing his almost infinite knowledge about semiconductors with me.

It was a great pleasure for me to spend the last years working in the Solid State Physics Group. I express thanks to all my colleagues for creating the pleasant 'vastestof' atmosphere, especially Herman Oerbekke, Gerard Kip, Geert Mentink, Rianne Nales, Ben van de Waal, Arend van Silfhout, Louis Jorritsma, Wulf Wulfhekel, Georg Rosenfeld, Paul de Boeij, Petra Hegeman, Sebastiaan van Dijken, Erwin Zoethout, Frank van Dijk, Ronny Van Moere, Oguzhan Gürlü, Stefan Kooij, Martijn Brower, Peter Broekmann, Esther van Vroonhoven, Misha Ovsyanko, Andrei Zinine, Ruben Sharpe, Petra v.d. Hoogenwerf, Martijn Middel and Agnes Mewe.

No experimental work would be successful without skilled technical support. Thanks to Herman, Geert an Gerard for providing it and always being patient, even if I had many questions and requests. Thanks to Rianne for her always quick and reliable help.

Thanks to Sebastiaan for being a great colleague and friend ('wenn die heißen Winde weh'n...'). Thanks to Ronny and Oguzhan for enriching my flat and life after the big bang. Thanks to Rico Keim for approximately 700 nice lunches and discussions about almost everything in the mensa.

Frank, Ronny, Oguzhan, Martijn, Esther, Misha, Ruben and Andrei: I wish you all the best and a lot of success for the remaining parts of your PhD studies. May the force be with you !!!

Finally, I want to thank my parents Hanne and Jörg Eßer for everything!

Thank you
and good-bye!

Bedankt
en tot ziens!

Euch allen vielen Dank
und auf Wiedersehen !